**Hassan, MZ, Aufa, AN, Brytan, Z, Tanski, T, Ren, J, Mazurkiewicz, J, Mohd Sani, MS and Ismail, Z**

**Selective laser melting of magnesium alloys for biomedical applications: Microstructure to clinical translation**

Journal of Materials Research and Technology 39 (2025) 660–691

Contents lists available at ScienceDirect

Journal of Materials Research and Technology

journal homepage: www.elsevier.com/locate/jmrt

# Selective laser melting of magnesium alloys for biomedical applications: Microstructure to clinical translation

Mohamad Zaki Hassan [a,b,*], A.N. Aufa [b], Zbigniew Brytan [b], Tomasz Tanski [b], James Ren [c], Janusz Mazurkiewicz [b], Mohd Shahrir Mohd Sani [d], Zarini Ismail [e]

[a] Faculty of Artificial Intelligence, Universiti Teknologi Malaysia, Jalan Yahya Petra, 54100, Kuala Lumpur, Malaysia
[b] Faculty of Mechanical Engineering and Technology, Silesian University of Technology, 18a Konarskiego Street, PL – 44-100, Gliwice, Poland
[c] School of Engineering, Liverpool John Moores University, James Parsons Building, Byrom Street, L3 3AF, Liverpool, UK
[d] Faculty of Mechanical & Automotive Engineering Technology, Universiti Malaysia Pahang Al-Sultan Abdullah, 26600, Pekan, Pahang, Malaysia
[e] Faculty of Medicine and Health Sciences, Universiti Sains Islam Malaysia, Persiaran Ilmu, Bandar Baru Nilai, 71800, Nilai, Negeri Sembilan, Malaysia

ARTICLE INFO

Handling Editor: L Murr

*Keywords:*
Selective laser melting
Magnesium alloys
Corrosion resistance
Biomedical implants

ABSTRACT

Selective Laser Melting (SLM) has emerged as a competitive additive manufacturing (AM) technique for producing magnesium (Mg) alloy implants with complicated shapes intended for biomedical usages. Mg alloys are appealing because of their biodegradability and durability, which are comparable to those of real bone. However, a rapid solidification in SLM creates issues in regulating the grain system, pores, and cracking, all of which considerably affect the strength and corrosion performances of the final components. This review highlights recent progress in clarifying the connections among processing settings, microstructural features, and their effects on biological elements. In vitro and in vivo studies are crucial for assessing the degradation behaviour, cytocompatibility, and biological reaction of SLM-Mg alloys in physiological environments. It also examines defect mitigation strategies and post-processing treatments. Future directions include the establishment of strategies to enhance alloy systems, the optimisation of process monitoring, and the implementation of improved characterisation techniques to enhance the clinical translation of SLM Mg-based implants.

## 1. Introduction

As industries are progressing to the IR 4.0, which includes the increasing of sustainable manufacturing, the need for an efficient implant with customised parts and mechanical properties has increased. Additive manufacturing (AM) has significant potential across various industries, including electronics, automotive, aeronautics, medicine, and dentistry. The biomedical industry has significantly adopted additive manufacturing for the capacity to efficiently produce patient-specific implants layer by layer from CAD models, utilising lower feedstock and allowing for significant freedom in design. Recent projections from the American Professional Association predict a significant yearly growth of up to 35 % in the AM medical implant market, potentially reaching $9 billion by 2027 [1]. Metallic powder bed fusion (PBF) is a recent AM technique that constructs metal components sequentially by selectively melting or sintering fine metallic powders [2]The PBF system includes techniques such as Selective Laser Melting (SLM), Direct Metal Laser Sintering (DMLS), and Electron Beam Melting (EBM), which enable the fabrication of intricate components with complex geometries, porous structures, and customised implants for patients. For example, SLM enables the production of implants with high precision and superior surface quality, therefore reducing the necessity for post-processing before clinical application [3], however it is expensive. DMLS offers numerous advantages for biological applications; nonetheless, the elevated temperature gradients produced during laser processing may result in residual stresses. The stresses that occur can lead to bending or changing the shape of the part, which might affect how accurately it fits and how strong it is for use in medical implants [4]. Another common powder bed method is EBM; however, it is less preferred for biomedical fabrication due to the higher surface roughness (25 μm–130 μm) than SLM (5 μm–40 μm) of the end product, attributed to their low melting point, as studied by Vayssette et al. [5]. In general, SLM enables the fabrication of highly complex geometries, typically producing components with near-full density, making it ideal for high-performance and biomedical applications [6].

Metallic biomaterials have been utilised since the early 20th century

* Corresponding author. Faculty of Artificial Intelligence, Universiti Teknologi Malaysia, Jalan Yahya Petra, 54100, Kuala Lumpur, Malaysia.
*E-mail address:* mzaki.kl@utm.my (M.Z. Hassan).

https://doi.org/10.1016/j.jmrt.2025.09.137
Received 14 August 2025; Received in revised form 15 September 2025; Accepted 15 September 2025
Available online 19 September 2025

to replace damaged or diseased bone. They are chosen for uses that need to support weight because they are very strong and durable, making them more reliable and longer lasting than ceramics or polymers. Table 1 illustrates that metallic materials are primarily utilised for fracture fixations and deformities. Generally, stainless steel, particularly SS 316L, is commonly used for low-cost implants due to its high modulus of elasticity and suitability for long-term fixation [7]. However, in comparison to cobalt-chromium (Co–Cr) alloys, it is less preferred by surgeons for prolonged utilisation [8],. This is primarily due to its incompatibilities with Magnetic Resonance Imaging (MRI) and a higher possibility of postoperative infections [9]. Currently, inert implants, like titanium (Ti) alloys, are extensively utilised for their abilities to integrate successfully with anatomical structures after implantation [10]. However, these implants have significant limitations, including vulnerability to corrosion in physiological conditions, potentially resulting in the release of harmful ions. The corrosive properties of metallic implants may result in the freeing of harmful metal ions into the body, generating an inflammatory reaction from the immune system and the surrounding tissues [11]. Ti, on the other hand, demonstrated the highest modulus, which may lead to implant loosening and infections in patients. Their higher stiffness compared to natural bone can lead to stress shielding, which may result in bone resorption and, over time, implant failure. This reaction compromises the biocompatibility of the implant and may negatively affect its long-term performance [12].

For this reason, Magnesium (Mg) is an excellent substance for application in the human body due to its elastic modulus nearly mimicking that of real bone. The density of Mg and its alloys is approximately 1.7 g/cm$^3$, slightly lower than that of natural bone, which typically ranges from 1.8 to 2.1 g/cm$^3$ [13]. In addition, Mg is naturally found in the anatomical body and weighs around 25–30 g [14]. This substance is mostly located in the skeletal region, contributing to bone density and strength [15]. It is crucial for metabolic processes involving blood glucose regulation, energy generation, and the maintenance of muscle and bone integrity. The release of Mg ions into surrounding tissues is considered safe and non-toxic to the human body. For bone implants, Mg must provide reliable and consistent support following implantation. A deficiency in Mg can cause various health issues, such as muscle cramps [16]. That facilitates the synthesis of apatite inside the bone matrix, hence enhancing bone strength and helping in daily mobility [16]. Mg exhibits robust mechanical strength, which includes increased specific strength, low melting temperature, and machinability [17]. Compared to other biomaterials, Mg's elastic modulus and compressive strength fall within the range of cortical bone, making it appropriate to be used for rigid implants in order to facilitate osteoblast proliferation and reduce the possibility of stress shielding effects [18]. However, The fast dissolution of Mg results in the accelerated release of hydrogen gas bubbles at a rate above what the body can absorb [19]. The presence of hydrogen ions accelerates the corrosion rate, leading to a loss of mechanical integrity in load-bearing applications. As a result, the implant may inadequately assist the healing process, consequently elevating the likelihood of failure. Due to this limitation, more than 95 % of Mg alloys are produced through casting because of its high efficiency. However, this method has significant drawbacks, particularly in its inability to produce complex geometries and near-net-shape porous structures required for advanced biomedical applications [20]. Deformation techniques can adversely impact the surface quality of Mg due to its inadequate workability at extreme temperatures [21].

For biomedical applications, the composition of metallic implants plays a crucial role in minimising adverse biological reactions. Ideally, the alloy used should be non-carcinogenic and non-toxic to ensure biocompatibility. Additionally, the implant must exhibit a controlled corrosion rate that aligns with the healing process. This allows the implant to retain its mechanical integrity long enough to support the surrounding tissue until the bone has fully remodelled and can independently sustain physiological loads [22]. In biomedical applications, such as hip implants and bone screws, the incorporation of calcium (Ca) into Mg (Mg) alloys is vital for decreasing implant weight while improving biodegradability, especially in load-bearing areas like the femoral condyle of the knee joint. These alloying elements improve mechanical performance by refining the grain structure, increasing corrosion resistance, and promoting the formation of intermetallic phases that also facilitate the manufacturing process [23] Table 2 presents common Mg alloys used in the SLM process, highlighting various alloying elements, including rare earth metals, and their corresponding properties. Alloying Mg with other metals is essential to improve and control biomedical behaviour in anatomical fluids. Mg alloys are broadly classified into three categories: aluminium-containing alloys like AZ31, AZ61, and AZ91 (AZ series); rare earth element-based alloys such as WE43; and aluminium-free alloys like Mg–Ca and Mg–Zn systems [24].

Mg alloys have surfaced as promising materials for biomedical implants, garnering considerable attention owing to their remarkable biocompatibility and biodegradability [26].

Fig. 1 shows various example cases of Mg alloys utilised in biomedical implants.

Mg alloys, specifically those processed using SLM present an intriguing option for dental implants due to their biodegradability, which minimizes the need for surgical removal after bone healing. The elastic modulus of Mg alloys (40 GPa) is comparable to that of cortical bone(30 GPa) [27], which makes them particularly suitable for load-bearing applications, such as tooth replacements. Mg alloys also offer the added benefit of reducing stress shielding effects, as they can gradually degrade over time while supporting the surrounding bone

**Table 1**
Mechanical properties determine the durability and compatibility of anatomical and metallic implants.

| Tissue/ Material | Density (g/cm$^3$) | Compressive Strength, $\sigma_c$ (MPa) | Tensile Strength, $\sigma_y$ (MPa) | Elastic Modulus, E (GPa) |
|---|---|---|---|---|
| Natural Materials | | | | |
| Cancellous bone | 1.0–1.4 | 160 | 35 | 0.01–1.57 |
| Cortical bone | 1.8–2.0 | 240 | 283 | 5–23 |
| **Mg Alloys** | | | | |
| Pure Mg | 1.74 | 20–115 | 90–190 | 45 |
| AZ31 (Extruded) | 1.75 | 83–97 | 241–260 | 45 |
| AZ91D (die-cast) | 1.81 | 160 | 230 | 45 |
| **Other Metallic Alloys** | | | | |
| Cobalt-Chrome Alloys | 7.8 | – | 430–960 | 195–230 |
| Stainless Steel | 7.9 | – | 480–620 | 193–200 |
| Titanium Alloys | 4.4 | – | 530–985 | 100–125 |

**Table 2**
Different alloying elements of Mg used in SLM [25].

| Alloy | Composition |
|---|---|
| Pure Mg | 100 % Mg |
| Mg–Zn | Mg–3 %–6 % Zn |
| Mg–Ca | Mg–0.4 %–1 % Ca |
| Mg–Sr | Mg–0.5 %–2 % Sr |
| Mg–Zn–Ca | Mg–3 % Zn, 1 % Ca |
| Mg–Zn–Ca–Sr | Mg–3 % Zn, 0.2 % Ca, 0.2 % Sr |
| ZK-series | Mg–3 % Zn, 0.6 % Zr (ZK30) |
| | Mg–4 % Zn, 0.5–0.8 % Zr (ZK40) |
| | Mg–6 % Zn, 0.5–1 % Zr (ZK60) |
| AZ-series | Mg–9 % Al, 1 % Zn (AZ91) |
| | Mg −3 % Al, 1 % Zn, 0.2 % Mn (AZ31) |
| Mg–RE Alloys | Mg–4 % Y, 3 % Zn (WE43) |

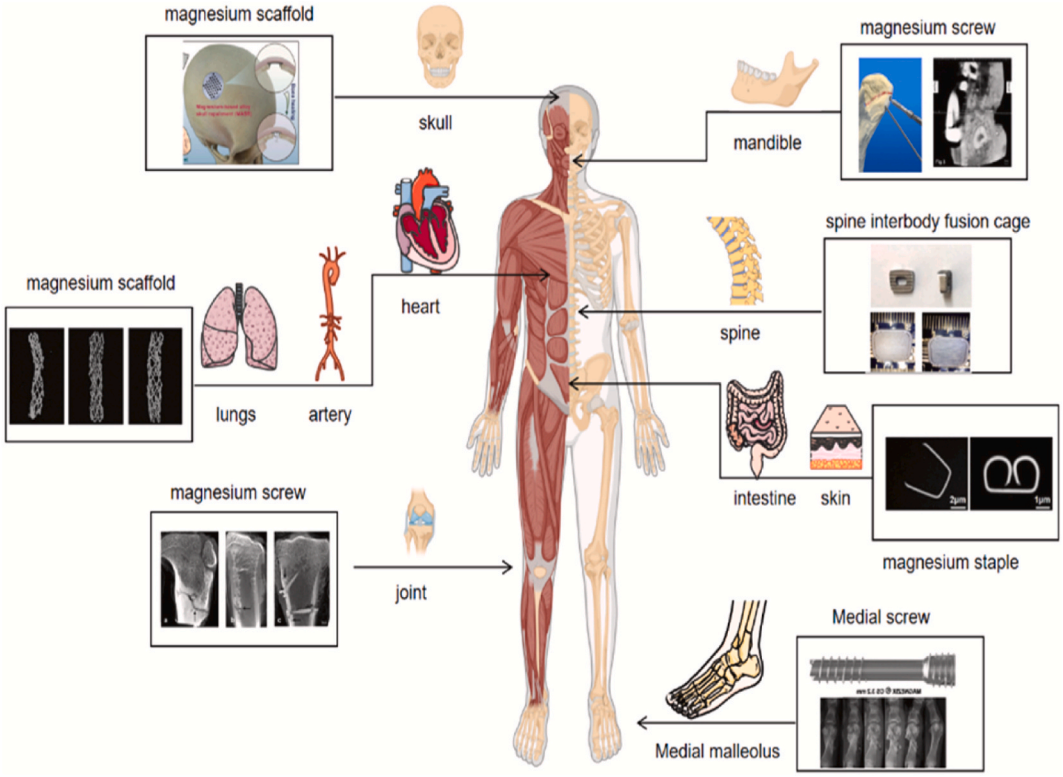


**Fig. 1.** Several case instances involving Mg alloys used for biomedical implants [26].

tissue [28].

However, the mechanical load conditions in the oral cavity and the specific corrosion challenges in anatomical microenvironment must be taken into account in designing dental implants. In addition to the general biological responses to Mg alloy implants in orthopedic application, dental implants pose additional clinical challenges that need to be addressed. The oral environment introduces different biological reactions to materials, primarily due to the presence of saliva, the mechanical stress from chewing, and the proximity to sensitive tissues, such as the gingiva. The degradation behaviour of Mg alloys in the oral cavity can be accelerated by the constant exposure to moisture and chloride ions in saliva, leading to a different corrosion rate compared to that seen in bone implants. Recent study by Helmer et al. [29] demonstrated that the presence of saliva, which contains ions like chloride (Cl-), accelerates the corrosion process which formed a hydroxide layer that can compromise the structural integrity of the implant over time. This study also supported by Qian et al. [30] corrosion caused by Mg particularly detrimental because it leads to the release of $H^+$ and an increase in pH levels in the surrounding tissues. This may cause irritation to the gingiva or result in the formation of pits, which could act as stress concentrators and contribute to implant failure [31]. Furthermore, the loss of material integrity due to corrosion may affect the mechanical properties of the implant. Seetharaman et al. [32] demonstrated that the byproducts of magnesium corrosion, which of magnesium hydroxide ($Mg(OH)_2$), are typically biocompatible and can be absorbed by the body, however, excessive corrosion can lead to the release of metal ions, which can affect the surrounding tissues, leading to inflammation. Further research should explore how Mg alloys, particularly those produced via SLM, can be optimised for these distinct conditions.

Thus, understanding how Mg alloys behave in the oral environment is essential for optimising their use in dental implants.On the other hand, mechanical stresses encountered by dental implants are fundamentally different from those in orthopedic implants. For example, while bone implants must support the entire weight of the body or resist impact from falls, dental implants primarily endure cyclical loading from chewing and grinding [33,34]. These loads are generally much smaller in magnitude but are more frequent and can vary depending on the type of tooth being replaced and the patient's chewing habits [35]. Given these specific load conditions, dental implants may require magnesium alloys with tailored mechanical properties to ensure they can withstand the repeated forces without degrading prematurely.

This paper aims to examine Mg alloys produced by SLM for biomedical implants, focusing on their degradation behaviour and the consequences for medical applications. It analyses the impact of SLM processing settings on microstructure and corrosion mechanisms, hence influencing implant performance and biocompatibility. The text addresses contemporary issues and prospective ways to enhance the biodegradability and safe, effective biomedical application of Mg alloys generated via SLM.

## 2. SLM process parameters

The microstructure and characteristics of SLM Mg alloys are significantly influenced by critical processing factors, including laser power, scanning velocity, hatch spacing, and layer thickness [36]. Enhancing these characteristics is essential for attaining optimal mechanical strength and reducing faults in the final component. These parameters govern temperature gradients and solidification features during manufacturing, directly affecting grain size, morphology, and crystallographic texture. Accurate optimisation of these parameters is essential for obtaining fine, homogeneous grain structures that increase structural strength and resistance to corrosion, consequently enhancing the reliability of Mg alloys for advanced biodegradable implants [3,37]. In SLM, energy density represents the combined effect of process parameters, defined as laser energy input per unit area or volume (Equation (1)) [38].

$$Energy\ density = \frac{P}{v.h.t} \tag{1}$$

the parameters *P, v, h,* and *t* represent laser power, scanning speed, hatch

spacing, and layer thickness, respectively.

### 2.1. Processing window in SLM

The energy density levels instantly impact the thermal history during processing, consequently influencing melt pool dynamics, solidification patterns, and the resultant mechanical properties. Operating within that window guarantees suitable energy input, facilitating complete melting and adequate fusing of powder particles while preventing defects such as porosity, warping, or cracking [39,40]. If parameters fall outside this window, Issues such as inadequate melting, keyhole formation, or thermal deformation can occur, weakening the quality and efficiency of biomedical Mg alloy components [41]. Establishing and keeping the processing window is vital for the uniform, defect-free production of Mg alloys by SLM. Several research studies have investigated Mg alloys, concentrating on the influence of varying laser strengths and scanning speeds in SLM procedures to fabricate fully dense components with superior mechanical properties. Like, Esmaily et al. [42] developed a process map focusing on scan speed and laser power to identify the suitable parameters for the fabrication of WE43 alloy components. Their advice indicated that the two terminal sections of the process map should represent regions of low and high energy input, as seen in Fig. 2(a). Specimens produced in the low energy input zone demonstrated decreased rigidity, mostly because of increased porosity and insufficient fusion [43]. Increased energy inputs resulted in significant Mg evaporation. The WE43 sample produced under OP1 conditions (Fig. 2(a)) had a more refined microstructure than the cast alloy, attributable to the elevated cooling rates. However, the increased porosity in the sample produced with OP1, in contrast to OP3, is attributable to reduced heat input, resulting in inadequate energy input. The forming zone, which includes OP2, is still the best area for fabricating Mg samples. So, increasing the laser power gives more energy to help the powder stick together, and slowing down the scan speed allows the laser to interact with the material longer, leading to a smoother movement of the liquid metal [44].

Wu et al. [45] additionally created a process map for the ZK60 alloy, considering laser power and scanning velocity. As shown in Fig. 2(b), the samples were categorised into five distinct regions. Region 1 was designated as the overheating zone, where smoke became apparent, and the sample displayed a heterogeneous surface along with reduced dimensional accuracy. At high input energy levels, Mg rapidly vaporises under continuous laser irradiation, leading to the ejection of molten metal driven by recoil pressure and Marangoni convection [46]. Lowering laser input energy reduced Mg evaporation, leading to

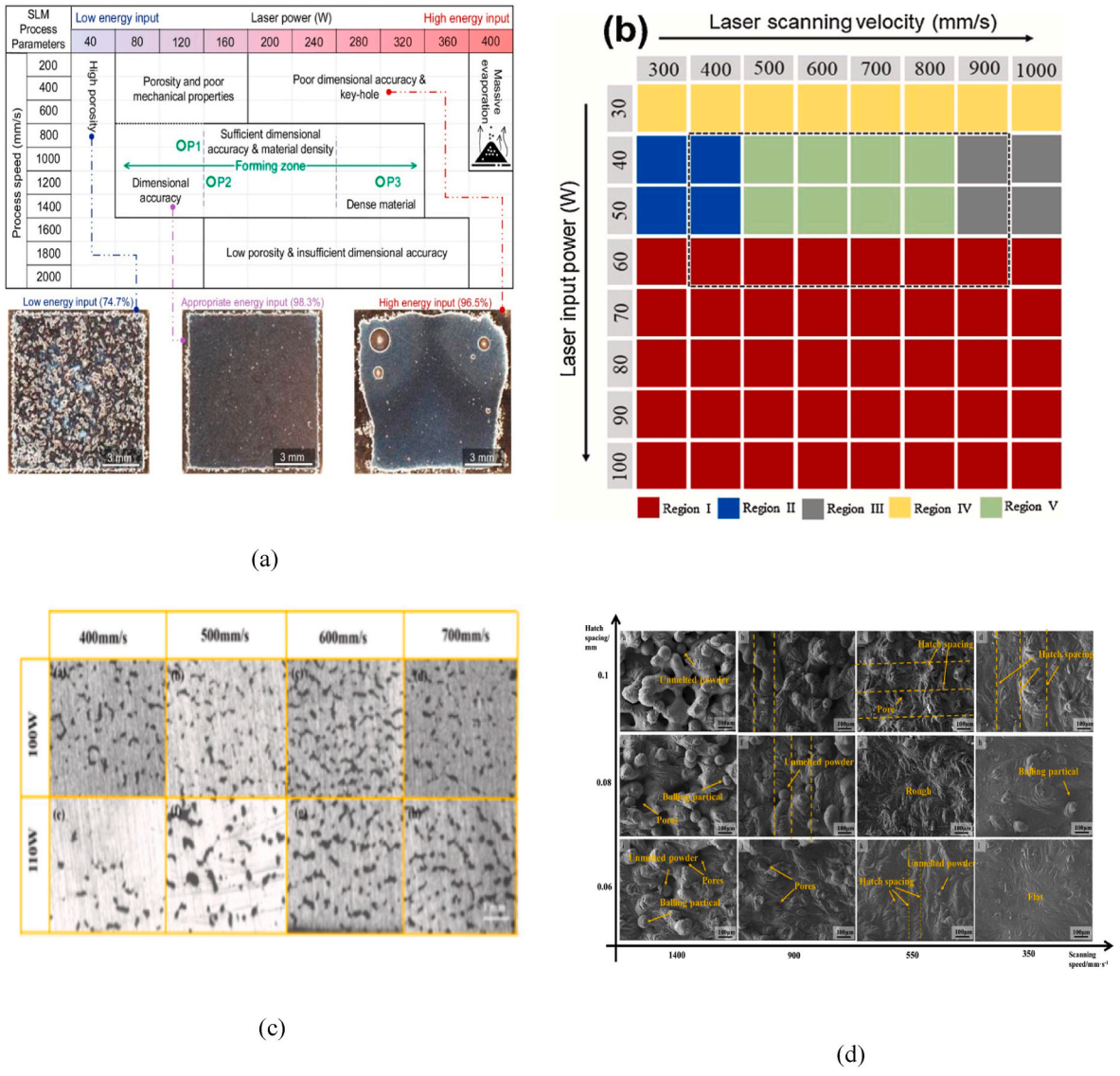


**Fig. 2.** Processing window for (a) WE43 [42], (b) ZK60 [45], (c) void formation in ZK60 [50] and (d) defect of ZK60 [26] following the SLM process.

enhanced surface quality (Region II); nevertheless, the samples continued to exhibit low dimensional accuracy and irregular surfaces. The melt pool in Region III displayed a low circumference-to-length ratio, resulting from inadequate powder melting, which led to instability. At lowered laser power (Region IV), the samples exhibited worse mechanical performance and poor forming quality [47]. In contrast, Region V, referred to as the optimal forming region, represents the ideal processing conditions for fabricating ZK60 alloy components. Tonga et al. [48] examined the influence of scanning velocity and laser intensity on the microstructural development of elements produced by SLM. Increasing both scanning speed and laser power enhances grain refinement and reduces texture intensity in the alloy [21]. The best combination of formability and mechanical properties was obtained within the laser power range of 200–250 W and scanning speeds between 750 and 1250 mm/s. Consequently, increased laser power improves particle consolidation, and reduced scan speed extends interaction time, facilitating smoother melt flow [49]. According to Liu et al. [50] modifying the scanning speed at a constant laser power did not produce a consistent pattern in defect generation. At a constant scanning speed, increasing the laser power significantly decreased the occurrence of defects [51]. Additionally, changes in scanning speed showed minimal impact on relative density. Notably, a laser power of 110 W paired with a scanning speed of 400 mm/s proved particularly effective in reducing flaws and enhancing the relative density of ZK60 samples (Fig. 2(c)). The effect of the combination between laser powers and scanning speed in terms of grain structure was evaluated by Wang et al. [52]. Grain size slightly increased with higher laser power due to the elevated molten pool temperature. At a constant cooling rate, higher laser power slightly extended solidification time and promoted minor grain growth.

In addition, Wang et al. [53] conducted a study on the effect of varying laser power levels on the microstructural characteristics of the AZ61 alloy fabricated using SLM. At low laser power, the samples exhibit poor surface morphology due to crater accumulation caused by insufficient energy input; yet, the low evaporation rate might reduce melt pool velocity, and the production of tiny bubbles contributes to the highest relative density [21]. As laser power increases, surface smoothness enhances and crater creation decreases; however, pore development increases [54]. While at a high power level, it leads to enhanced evaporation, considerably promotes pore formation, and reduces the relative density of the parts [55]. Hatch spacing is the distance between the centres of adjacent laser scan tracks in SLM. It directly affects melt pool overlap, influencing surface quality and porosity [56]. Generally, reducing hatch spacing increases element density and lowers defects, as tighter scan lines provide enhanced melt dispersion and fluid dynamics. In contrast, increasing the hatch spacing beyond the laser spot size reduces overlap, leading to inadequate fusion between adjacent tracks and increased porosity [57]. Ultimately, differences in hatch spacing result in changes in surface quality, heat transfer characteristics, and overlap efficiency.

Liu et al. [58] observed that the effect of surface morphology of SLM-AZ61 alloy varies with processing parameters. Fig. 2(d) shows that at higher scanning speeds, enlarging the hatch spacing results in bigger pores, whereas at lower speeds, narrowing the hatch spacing improves surface roughness. It corresponds to the surface tension induced by the rising temperature gradient. An increase of hatch spacing lowers the temperature gradient and energy input [55] therefore elevating surface tension and liquid viscosity, which ultimately restricts the smooth movement of molten material towards the outer edge of the pool [47]. Consequently, increasing the hatch spacing alters the overlap between adjacent scan tracks and influences molten pool dynamics, leading to the formation of defects such as balling and porosity. In contrast, optimising hatch spacing at a fixed scanning speed effectively mitigates these defects, resulting in a smooth and defect-free surface morphology.

Bandar Al-Mangour et al. [59] examined the correlation between energy density and hatch spacing in relation to the solidification process of the final fabricated component. The densification of components fabricated via SLM is predominantly governed by melt pool dynamics and the chosen hatch spacing [60]. Insufficient energy density may result in gaps between adjacent scan tracks, provided the melt pool is wider than the hatch spacing. Maintaining an ideal hatch spacing of 60–120 μm, along with regulated overlap, is essential for reducing lack-of-fusion porosity. This leads to unmelted powder or pore development, thereby diminishing the densification of the deposited material. At elevated energy densities, where the melt pool diameter exceeds the hatch spacing, adjacent scan tracks overlap efficiently [61]. This facilitates the remelting of the previous track, thereby reducing pore formation. Under the specified conditions, a final relative density of approximately 93 % was achieved; however, the occurrence of additional laser-induced defects in some instances adversely affected the overall densification.

Equation (1) shows that energy density decreases as layer thickness increases, indicating an inverse relationship between these two parameters. Consequently, the remaining three parameters must be adjusted appropriately to guarantee sufficient energy input for effective powder melting when the layer thickness is changed. At all layer thicknesses, increased laser power coupled with excessive scanning speeds led to significant vaporisation and thermal distortion in the melt pool, resulting in process failure [49]. In contrast, decreased laser power combined with higher scanning velocities and consequently low energy density resulted in a lack of fusion defects, yielding irregularly shaped structures. At moderate energy densities and scanning speeds, entirely dense cross-sections were attained, revealing low porosity and little lack of fusion. Under these optimal conditions, the relative density surpassed 99.5 %. The influence of laser power on relative density was determined to be more prominent than that of scanning speed [26]. Optimal fusion with few imperfections was achieved at moderate laser power and scanning velocity across all evaluated layer thicknesses. However, the ideal energy input necessary for defect-free manufacturing diminished as the layer thickness formed [56]. Yang et al. [62] divided the process window mapping for AS41 into three distinct zones. A significant amount of pores and balling were discovered in the metallographic specimens within the region marked by insufficient energy density during the initial mapping. Increased energy densities improved the density of the specimens, ultimately minimising the defects (Fig. 3). When the scanning speed was higher, the scanning trace and hatch spacing would be tiny, resulting in a decrease in overlap area. Conversely, the growth of the molten pool increased as the scanning speed diminished, leading to a coarser microstructure [63], a reduction in nucleation sites, and diminished anisotropy.

In summary, optimising energy density is vital for attaining complete melting, stable melt pool dynamics, and effective interlayer bonding in SLM-Mg alloys [64], while avoiding defects such as vaporisation or oxidation. Research consistently indicates that an energy density between 83 and 167 J/mm$^3$ is often effective for the creation of SLM-Mg alloys. This range has been extensively utilised to attain elevated densification levels and optimal mechanical performance in the final components [65]. For instance, Wei et al. [66] indicated that this energy density range is appropriate for manufacturing AZ91 parts, facilitating the development of a compact microstructure with fewer imperfections. Wang et al. [67] similarly established that this range is suitable for processing more complicated Mg alloy systems, such as Mg–Y–Sm–Zn–Zr, hence providing steady melt pool dynamics and enhanced part quality. Liu et al. [58] revealed that a marginally narrower energy density range of 125–150 J/mm$^3$ produced exceptional outcomes for the AZ61 alloy, underscoring the material-specific characteristics of optimal SLM parameters. Additionally, Shi et al. [68] determined that an energy density of 83 J/mm$^3$ was adequate for producing WE43 alloy with superior surface quality and reduced porosity. These findings collectively underscore the importance of carefully selecting energy density based on the specific alloy composition and processing requirements. This range delivers adequate energy to

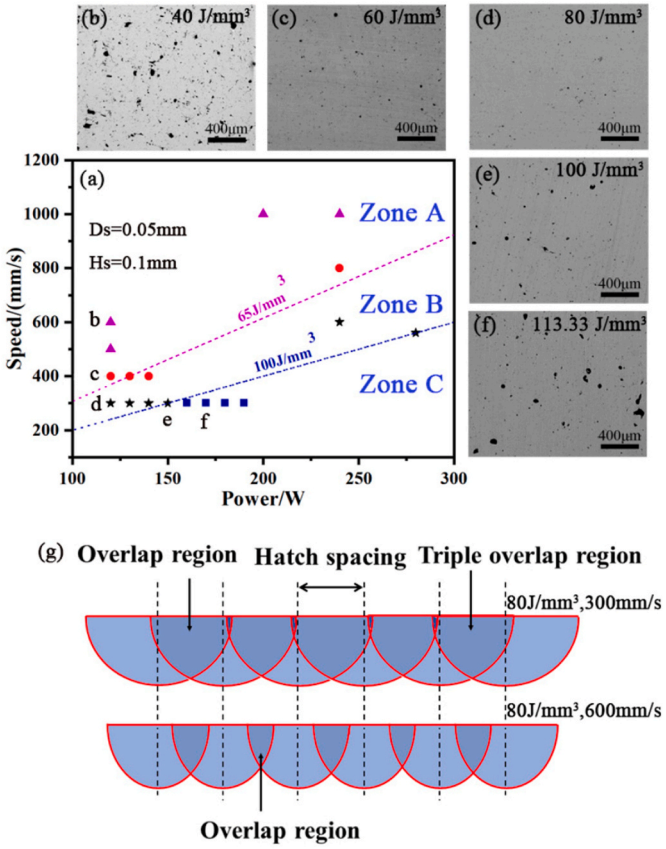


**Fig. 3.** The effect of hatching distance [62] on the fabrication quality and characteristics of parts produced by SLM Mg alloys.

completely melt powder layers and partially remelt the underlying layer, facilitating metallurgical bonding and reducing lack-of-fusion. Components manufactured during this period generally have relative densities over 98 %, which is crucial for structural and biomedical uses [58]. Operating below this energy density frequently results in inadequate melting, higher porosity, worse bonding, and poor surface quality. Conversely, excessive energy input can lead to over-melting, keyhole porosity, material evaporation, and significant oxidation due to Mg's low boiling point (approximately 1091 °C), hence compromising mechanical performance [45,69]. To guarantee high-quality Mg components, it is crucial to tune specific parameters, such as laser intensity, scan speed, hatch distance, and layer thickness, within this perfect energy range.

Enhanced energy density not only advances fusion but also ameliorates the microstructure. Controlled thermal input promotes the development of fine, equiaxed grains, thereby improving both strength and ductility. Energy density is essential in SLM to guarantee enough melting and prevent imperfections. insufficient energy results in insufficient fusion, whereas excessive energy induces keyhole porosity [21]. Preheating the build plate to 100–200 °C can mitigate temperature gradients, therefore decreasing residual stress and cracking during fabrication [55]. It restricts the development of inclusions and oxide films that may serve as locations for crack initiation. Moreover, it is essential to maintain an inert environment with oxygen levels below 100 ppm to avert oxidation during processing [70]. It must be linked with additional process factors, including powder morphology, scanning method, and environmental control [59]. Mg's high reactivity necessitates processing in an ultra-low oxygen atmosphere to prevent oxide inclusion and combustion risks. Consistent powder distribution and uniform laser irradiation are essential for ensuring repeatability and uniform densification [61]. Table 3 delineates various strategies for enhancing the quality of Mg alloys produced using SLM.

**Table 3**
Outlines several ways for improving the quality of SLM-Mg alloys.

| Objective | Key Parameters | Optimisation Strategies | Expected Outcome |
|---|---|---|---|
| Structure | Scanning strategy | Employ stripe or chessboard scanning patterns. | Consistent and stable shape, minimized distortion |
| | Hatch spacing | Enhance hatch spacing overlap (60–120 μm) to mitigate residual stress. | |
| Mechanical Properties | Correlation between laser power and scanning velocity | Moderate to high laser power with moderate scanning velocity | Enhanced mechanical characteristics |
| | Layer thickness | Employ thin layers measuring 20–30 μm. | |
| Microstructure | Energy density | Adjust energy density to prevent excessive heat buildup. | Control energy density to prevent excessive heat buildup. |
| | Rate of cooling | High cooling rates favour fine grain size | |
| Void Minimization | Laser energy density | Use optimal energy density (83–167 J/mm$^3$ for Mg) | Reduced porosity, better part integrity |
| | Atmosphere | Inert gas (Ar) with low $O_2$ level (<0.1 %) | |

## 3. Defect in SLM - Mg alloys

### 3.1. Surface defect

Surface defects refer to deviations from the ideal surface profile defined by the CAD model, resulting in uneven or irregular surface features. In AM components, four primary factors contributing to these defects have been identified: the staircase effect, partially melted powder particles, the balling phenomenon, and surface cracking. Four main sources of defects have been recognised: staircase formation, incomplete melting of powders, balling, and cracks on the surface [51]. These imperfections collectively lead to increased surface roughness and reduced dimensional accuracy, highlighting a significant limitation of additive manufacturing when compared to conventional techniques such as machining. Jinge et al. [71] presented a crack and balling effect phenomenon on the surface of ZK60 samples fabricated by the SLM process. The continuous melting of adjacent scan tracks and successive layers, along with the cyclical variations in temperature related to the layer-by-layer additive manufacturing process, results in localised solidification shrinkage and thermal contraction, leading to the buildup of significant thermal stresses [70]. As the previously solidified layers underwent repeated reheating, their temperatures occasionally exceeded 340 °C, leading to localised remelting [72]. This remelting promoted liquation cracking, particularly in regions enriched with segregated elemental precipitates. The pronounced temperature gradients between the molten pool and adjacent solidified material facilitated the development of solidification cracks within the deposited layers. The existence of a crack in the upper layer of the specimens in Fig. 4 further confirmed the occurrence of solidification cracking.

#### 3.1.1. Balling effect

The balling phenomenon refers to the production of irregular, circular droplets or beads along the scan track instead of a smooth, continuous melt pool. In SLM of Mg alloys, this issue is particularly

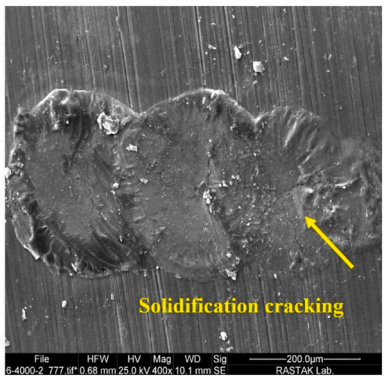


**Fig. 4.** Formation of surface solidification cracks in AZ80 alloy during fabrication by laser-based methods [73].

prominent due to Mg having a low boiling point, high pressure in the vapour, and weak wettability [74]. These conditions may contribute to uncertainty in the molten metal and irregular solidification. Balling may occur due to uneven powder dispersion across consecutive layers. The insufficient wettability of the surrounding layer, pore formation, and disruptions in the build process due to interactions with the recoating blade would also lead to balling [74].

Numerous variables are recognised to influence balling in single-track in molten metal. It generally happens as capillary forces act to reduce surface energy. Capillary forces are affected by the melt temperature due to surface tension getting lower as the temperature increases. As a result of steep temperature gradients on the melt pool surface, Marangoni flow can lead to the disruption and separation of continuous melt tracks [74]. This situation is more probable when the liquid metal exhibits inadequate wetting capabilities on the adjacent powder or substrate. The issue gets worse by the development of oxide layers, which elevate the wetting angle and restrict sufficient melting and bonding between layers [75,76].

Balling events can occur at both low scanning speeds with high energy input and at high scan speeds, irrespective of the laser power level applied. Excessive energy within the melt pool can inhibit proper solidification, accelerating the point at which surface tension drives melt pool instability. Ball formation is identified as a non-equilibrium phenomenon that disturbs melt pool fluid dynamics and solidification processes [77].Traditional approaches to alleviate this problem include boosting the energy density or decreasing the powder layer thickness. This defect mechanism significantly affects the quality of the final component, frequently resulting in heightened surface roughness, increased porosity, and weakened interlayer adhesion in areas near the produced balls. For example, Zoller et al. [78] analysed the balling phenomenon by pairing simulation results, analytical models, and experimental data in the SLM process. The simulation features four distinct zones: depression, transition, neck, and tail end. In the early depression zone, the melt pool is shifted downward toward the laser beam due to substantial recoil pressure and Marangoni forces [79,80]. Then, the transition zone arises from diminishing high-temperature gradients, restricted melt extrusion, and an evenly distributed melt pool width [81]. The region where the melt [82] pool contracts after laser irradiation is referred to as the necking zone. This is substituted by the end portion, resulting in the creation of a balling (Fig. 5 (a)). The depression and transition zones exhibit consistent phenomena, but the neck and tail regions undergo repeated changes resulting in the development of spheres [83]. Wang et al. [80] claim that scanning speed is crucial in defect creation, especially balling. An increment in scanning velocity reduces the thermal energy transferred to the material, hence raising the thermal gradient inside the solidification zone. This situation results in insufficient powder melting and fast solidification, preventing maximum bonding between the powder surface and the substrate [84].

Both top-down and cross-sectional perspectives of the simulation domain at differing scanning velocities demonstrate that variations in scanning speed markedly affect the morphology of the melt pool. Prolonged laser exposure increases thermal input, resulting in an expanded heat-affected zone (HAZ). Furthermore, the isothermal region at the trailing edge expands, providing adequate heat energy for the melting of neighbouring powder particles. Currently, the molten pool has a broad and profound form, together with significant melt length and depth. As a consequence, the specimen may have lower densification, leaving it subject to porosity and balling issues. The circle markers indicate balling effects, and the rectangular markers signify pores under a constant laser power, with scanning rates varying from 400 to 1200 mm/s examined (Fig. 5(a)). Fig. 5(b) illustrates that the evolution of the balling phenomenon is influenced by the combined effects of recoil pressure, Marangoni convection, and heat dissipation, all of which are closely linked to the applied energy density.

Also, Liu and Guo [85] provided a detailed four-main-contributing-factors explanation of the balling phenomenon in SLM-processed Mg alloys. They observed that the (i) low viscosity and high surface tension [43,86,87] of molten metal promote the creation of dispersed metal spheres due to the interplay between viscous flow and surface energy reduction. It is also associated with Plateau–Rayleigh capillary instability [83,88,89], a natural phenomenon in which liquid cylinders split into tiny drops as a result of surface tension. (iii) Thermodynamic considerations contribute to the balling phenomena. In this case, The liquid metal has more potential energy than the molecules at its surface [80,90], attempting to minimise its surface energy, resulting in the creation of spherical droplets. The powder on the substrate undergoes complex dynamic behaviour, including melting, wetting, spreading, and solidification, all of which are affected. In this process, capillary forces compete with inertial resistance [83], while rapid solidification under steep temperature gradients hinders spreading, ultimately leading to the spheroidisation of the liquid metal. In terms of energy density, it was suggested that high scanning speeds result in low energy input, leading to insufficient heating and the formation of spheroidised balling. Large-sized balling particles are often observed due to the inadequate energy density (Fig. 6). Al Mangour et al. [59] elucidated that balling occurs when the molten pool insufficiently wets the surface due to low energy density, resulting in the liquid dividing into spheres to reduce interfacial tension. This phenomenon also arises at elevated scanning velocities and inadequate energy density, leading to melting pool instabilities and Marangoni convection [91]. Increased scanning speeds lead to significant shrinking of powder particles, causing capillary instabilities in the molten pool that produce spherical forms of varying sizes, which ultimately impede the densification process. Additionally, oxygen may infiltrate the molten area either through the powdered feedstock or by entrapped gases generated by turbulent melt pool dynamics. Hu et al. [92] described balling occurring during the SLM of Mg, even when the oxygen concentration in the chamber is below 0.2 %. In general, the inadequate interlayer bonding, occurrence of balling, and weakened densification can be partially attributed to an oxide film on the surface of the preceding layer, which obstructs efficient remelting and metallurgical bonding during subsequent laser scans, consequently compromising the overall build quality [93].

Chen et al. [94] categorised three energy density regimes corresponding to the micro- and macro-morphological characteristics of SLM-processed Mg-RE alloys. At low energy density, High-melting-point RE elements often remain unmelted, while low-melting-point elements like Mg and Zn melt quickly. These unmelted RE-rich particles hinder laser penetration and reduce wettability, leading to incomplete melting and particle adhesion on melt tracks. They also trap gas, forming micro-defects. Balling is observed on both surfaces and sides of the samples. As the energy density enters the transition mode, the increased input energy causes Mg and Zn vapours to entrain fine particles into the melt pool, resulting in spatters that become cold-welded to the surface. The laser tracks form continuous, fish-scale-like patterns, while only a

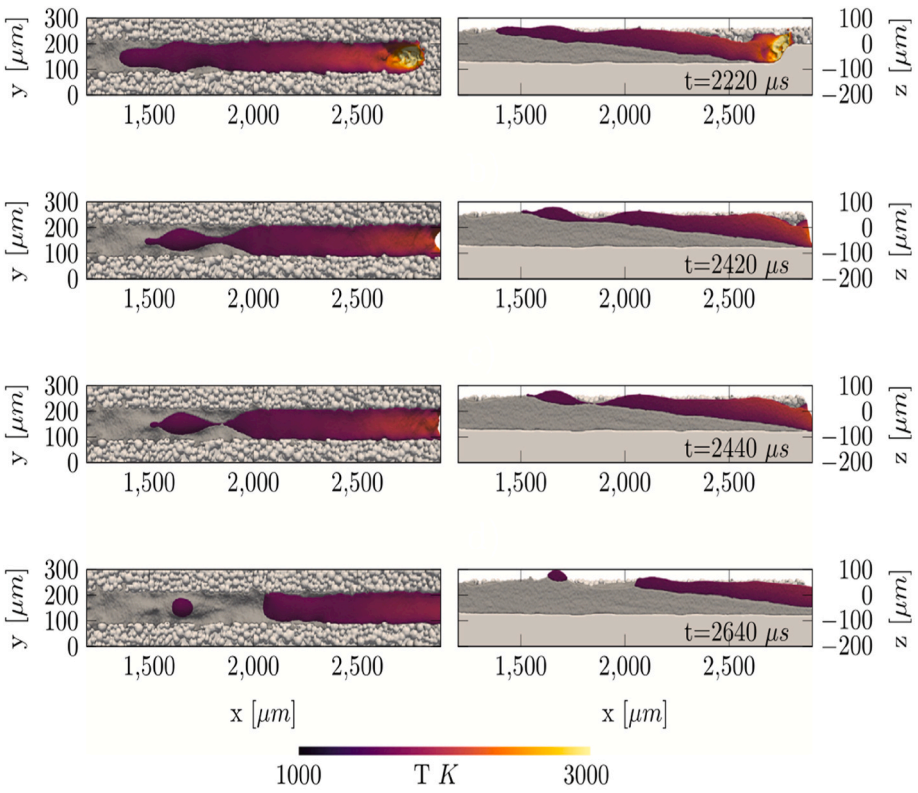


(a)

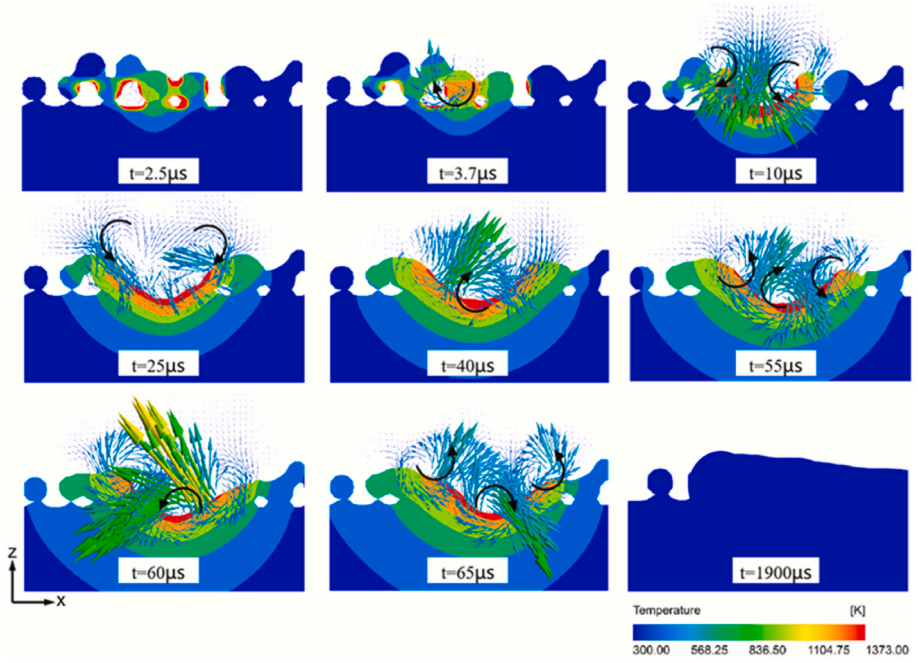


(b)

**Fig. 5.** Evolution of (a) the balling phenomenon as explained by Zoller et al. [78], influenced by the combined effects of recoil pressure, Marangoni convection, and heat dissipation [79] during SLM Mg alloy.

few gas pores are generated due to the combined effects of Marangoni flow, recoil pressure, and buoyancy [95]. The resulting surface exhibits minimal balling and cracking. At high energy densities, the SLM process enters the keyhole mode, characterised by intense melt pool turbulence, gas entrapment, and the formation of irregular pores. The vaporisation of elements, combined with melt flow instability, gives rise to rough, wave-like surface morphologies featuring humps, valleys, and agglomerated particles [96]. Additionally, unmelted powders can be drawn into the melt pool and solidify at its base, while trapped gases contribute to surface collapses, central bulges, and peripheral burnout defects.

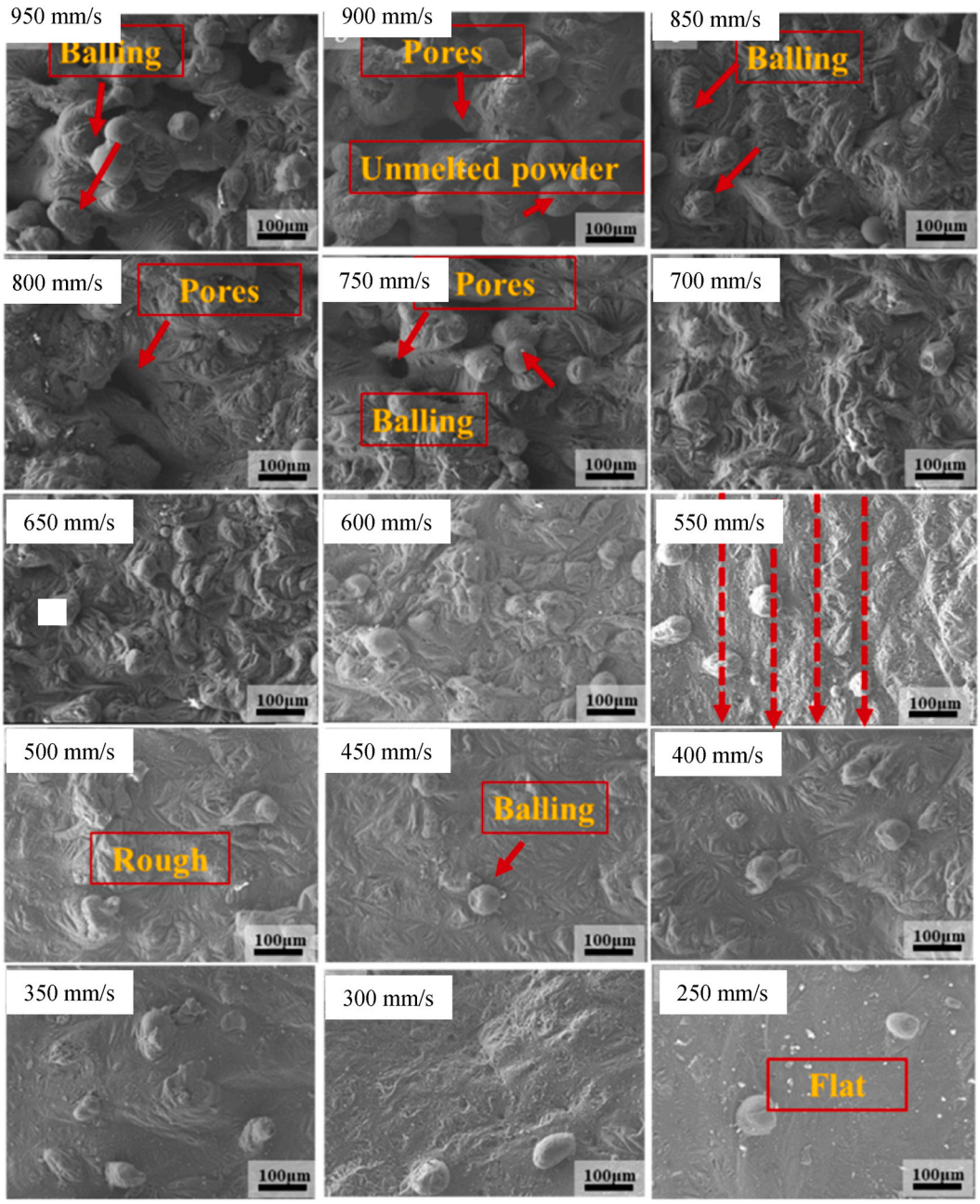


**Fig. 6.** Surface morphology of SLM AZ61 at various scanning velocities [85].

An established strategy to mitigate balling involves increasing the applied energy density or reducing the powder layer thickness. Nevertheless, balling may still occur at elevated scanning speeds, independent of the laser power level. This defect is considered a fundamental challenge in SLM processing, as it contributes to the formation of rough surface features, elevated porosity, and compromised interlayer bonding in areas where spherical accumulations of material are present [97].

### *3.1.2. Unmelted/partially melted powder particles*

In SLM Mg alloys, unmelted or partially melted powder particles may arise from insufficient energy input, high scan speeds, or inadequate laser absorption. The elevated heat conductivity and low boiling point of Mg, coupled with surface oxidation and inadequate wettability, prevent complete melting. These particles reduce part density, weaken interlayer bonding, and may act as initiation sites for defects such as cracks or pores. Yang et al. [98] depict the surface topography of SLM Mg alloy in relation to energy density. At low energy density, the fine particles retained their original topologies without any aggregation. The energy density was marginally higher, resulting in the presence of unmelted particles on the surface. At intermediate energy densities, a significant quantity of coarsened particles was discovered, several of which were cemented together, resulting in weakly linked sintering necks [99].In this condition, the particle temperature exceeded the melting point, leading to partial melting. A minimal quantity of liquid phase enhanced the sintering of neighbouring particles, resulting in incomplete fusion and weak inter-particle bonding. Fig. 7 presents SEM images of the top surface morphology and corresponding cross-sections of samples fabricated at various laser powers. Three typical surface morphologies are highlighted [54]. The influence of energy density on pore formation, defects, and microstructure is clearly observed. Samples exhibit pores of different shapes and sizes. At low energy densities, unmelted and partially melted powders are prevalent due to insufficient energy input

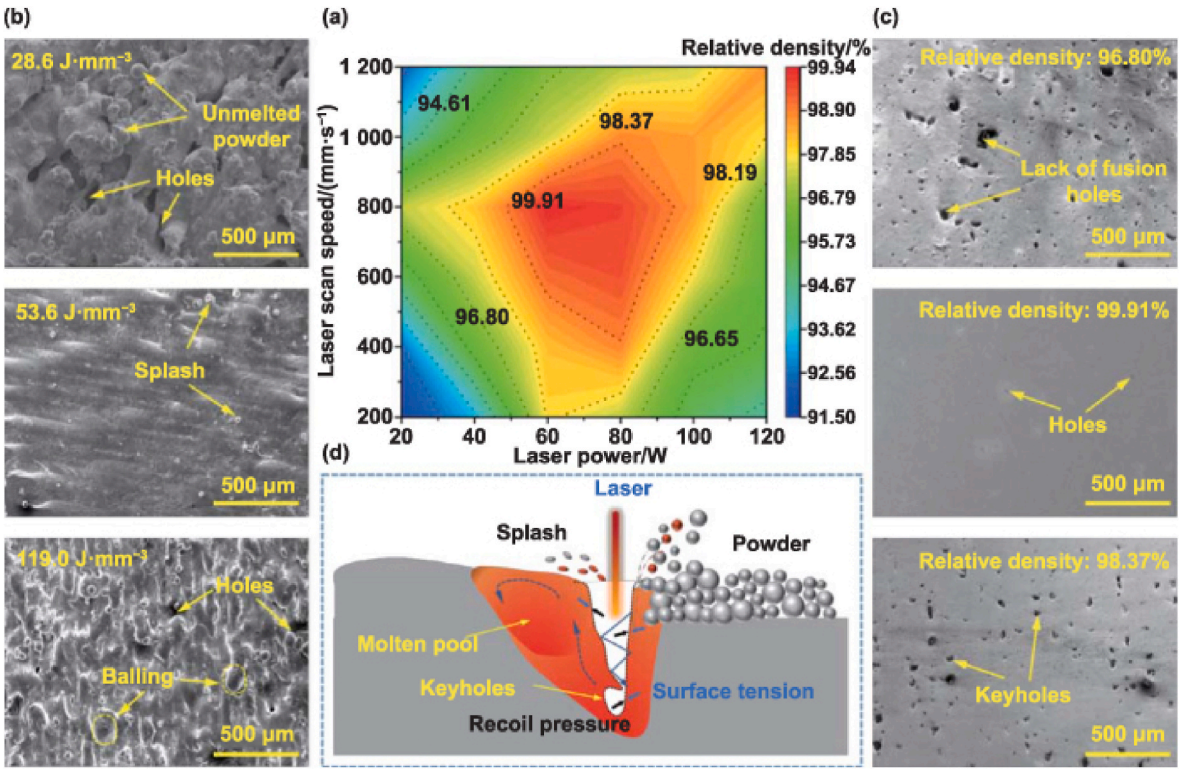


**Fig. 7.** Surface morphology, unmelted particles, holes, and other defects in SLM WE43 alloy fabrication [100].

[90]. As the energy density increases, more complete melting of the metal powder occurs, reducing the presence of microscopic pores and resulting in a denser, more uniform microstructure.

### 3.2. Internal defect

#### 3.2.1. Crack

The quick melting and significant temperature fluctuations in the HAZ of Mg alloy induce superheating and undercooling at the grain boundaries during the SLM Mg process. This results from high thermal stresses, a wide solidification temperature range, the existence of a low melting point of the eutectic phase at grain boundaries, and the presence of slag inclusions and structural segregation, all of which facilitate crack formation. Also, the influence of sample size, preheating, laser energy input modification, and scanning technique on cracking susceptibility is going to be examined. In the SLM process, hot cracking is categorised into two main types: solidification cracking, which occurs in the mushy zone during the final stages of solidification, and liquation cracking [101], which develops in partially melted areas adjacent to the melt pool due to localised overheating and melting along grain boundaries. Liang et al. [102] provided a detailed explanation of the thermal cracking mechanisms in Mg–Zn binary alloys during SLM processing, highlighting the formation of both solidification and liquation cracks. Under conditions of high energy density input, Zn migrates towards the edges of the solid–liquid interface, depositing along grain boundaries and dendritic formations. During rapid solidification, Zn segregation leads to the formation of weak liquid film zones. When thermal stress is applied at the grain boundaries, solidification cracks initiate within these zones [103]. In contrast, liquation cracks occur in the HAZ as a result of thermal stresses caused by differences in solidification temperatures (Fig. 8(a)). These cracks typically begin with grain boundary tearing due to tensile stress generated by thermal expansion during heating and contraction during cooling. Liang et al. [102] analysed the structure, mechanical behaviour, and crack features of ZK60 Mg alloy. Under optimal operational conditions, the microstructure consisted of an equiaxed and lamellar zone, with the molten pool boundary comprising Zn elements. The fine-grained phase considerably affected the properties of the sample, with thermal cracks primarily consisting of liquation cracks [51].

Early work by Liu et al. [71] reported that the wide solidification temperature range and low eutectic temperature significantly contribute to the hot cracking risk of the SLM ZK60 alloy. In general, the solidification range from the liquidus temperature at 640 °C to the eutectic temperature at 340 °C for the $Mg_7Zn_3$ phase can promote the formation of liquation cracks [104]. The higher cooling rates, coupled with localised solidification shrinkage and thermal contraction over successive heat cycles, ultimately lead to the creation of multiple tracks and layers during the welding process (Fig. 8(b)). Wei et al. [105] examined the fracture characteristics of SLM Mg alloys in relation to the zinc concentration in the final products. Lowered Zn content can produce a near fully dense product; with increasing it could suffer from solidification cracks. All samples exhibit a microstructure composed of an α-Mg matrix and a eutectic $Mg_7Zn_3$ phase. Nonetheless, once the Zn content significantly increases, the formation of micro-pores becomes apparent. This phenomenon is attributed to the segregation of Zn during solidification, which fosters low melting point phases near grain boundaries, leading to shrinkage and localised porosity [106]. Fig. 8(c) illustrates the evolution of cracks related to Zn content.

#### 3.2.2. Internal pores

In general, internal pores in SLM for Mg parts can be classified into lack of fusion, gas pores, and keyhole pores. The lack of fusion pores is widely recognised as an effect of insufficient energy input, resulting in a tiny and shallow molten pool that fails to effectively penetrate the previously formed layers [107]. While gas pores in SLM-processed Mg alloys typically arise from multiple interrelated resources. The vaporisation of low-boiling-point elements, like Mg and zinc, produces gas within the melt pool. Moreover, shielding gases or residual gases encapsulated in the powder may be incorporated during the melting process [108]. The high solidification rates characteristic of the SLM

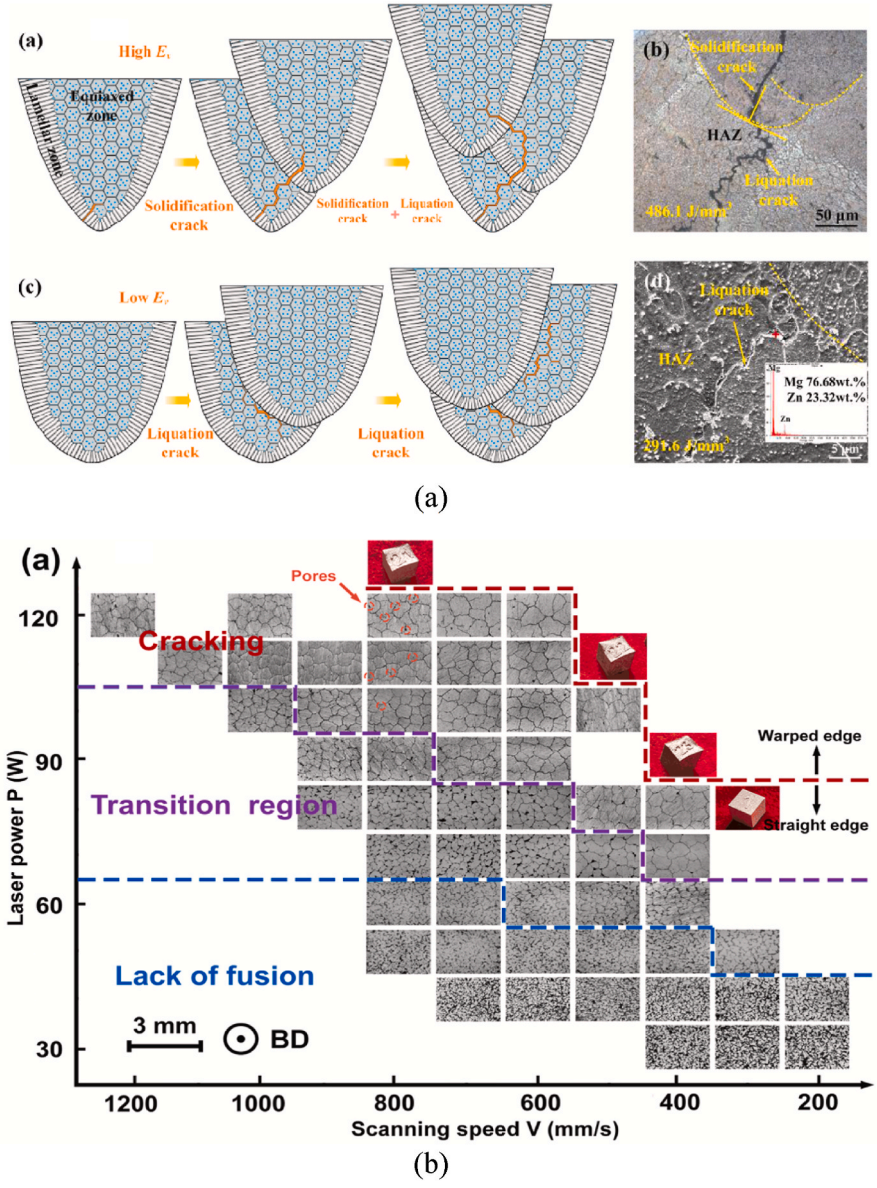


**Fig. 8.** Presence of (a) solidification and liquation cracks in the HAZ [102], (b) transition of crack evolution [71] and (c) crack formation associated with Zn content [105].

process typically prevent gas bubbles from escaping, resulting in the development of pores inside the formed material. The keyhole pores are generated by the unstable melting phase [109].

*3.2.2.1. Lack of fusion.* Wang Y. et al. [58] showed a map that explains how laser power and scanning speed affect the creation of internal pores in Mg alloy made using SLM. The window map identifies three distinct regimes: lack-of-fusion, keyholing, and stable melt pool zones. At a constant laser power of 40 W, numerous irregular lack-of-fusion holes, typically measuring between 30 and 80 μm, become apparent due to inadequate energy input. As the scanning speed increases, both the frequency and size of these pores also increase [110]. The emergence of unconsolidated particles indicates insufficient melting and weak inter-layer bonding, typical of the lack-of-fusion regime. Shorter interaction time under high scanning speed conditions reduces the energy input. Spherical keyhole pores form when the scanning speed is between 200 and 400 mm/s and the laser power goes up, because the process changes from conduction to keyhole mode due to the evaporation of metal [72]. On the other hand, raising the laser power and scan speed significantly decreases both lack-of-fusion and keyhole porosity [111], leading to very dense specimens (Fig. 9(a)). Nevertheless, small circular pores are evident even in optimised settings. Niu et al. [112] reported that porosity in components produced by SLM predominantly originates from entrapped gases and incomplete fusion due to insufficient energy input. Gas pores typically range from 1 to 10 μm in size, whereas lack-of-fusion pores are larger and characterised by irregular morphologies. In this study, higher scanning speeds led to a reduction in energy density, thereby increasing the likelihood of lack-of-fusion defects. As a result, both the number and volume of lack-of-fusion pores exhibited a positive correlation with increasing scanning speed (Fig. 9(b)). Similarly, Li X et al. [113] presented fracture morphologies consisting of the relationship between laser power and scanning speed to represent the defect of SLM Mg samples. When laser power is reduced and scanning speed is moderate, the surface exhibits numerous lack-of-fusion defects and gas pores, primarily caused by insufficient energy input [114]. In contrast, greater energy input at lower scanning velocities leads to the

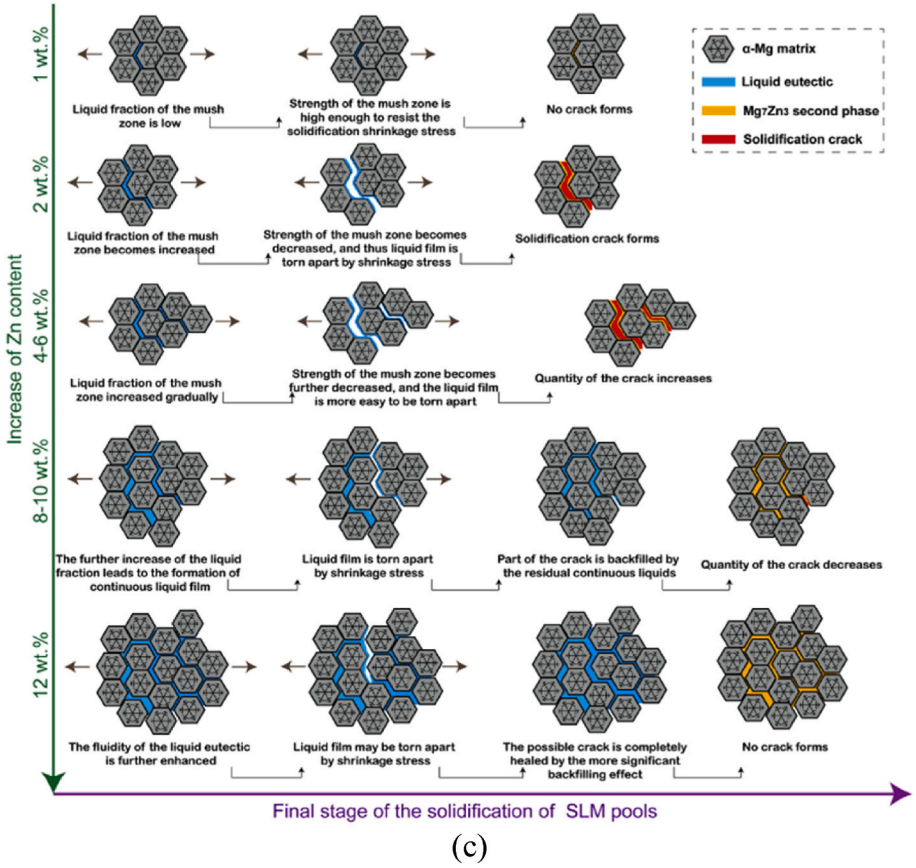


**Fig. 8.** (*continued*).

development of keyholes and gas porosity, presumably due to increased metal vaporisation and an unstable keyhole phenomenon induced by excessive laser radiation. Under optimal processing conditions, the fracture morphologies exhibited a notable transformation, characterised by a highly dense distribution of equiaxed dimples with an almost complete absence of pores and microcracks [115]. Yin et al. [56] reported that the variation in mechanical properties as a function of processing parameters closely mirrors the trend observed in densification behaviour. This connection supports the idea that defects are important stress points when the material is under mechanical load, which can cause cracks to start and grow, leading to early failure and poor mechanical performance. Importantly, lack-of-fusion pores and cracks exert a more pronounced deleterious effect on mechanical integrity compared to keyhole and gas pores [106]. The relatively smooth and rounded morphology of keyhole and gas pores facilitates a more uniform stress distribution, thereby mitigating localised stress intensification. On the other hand, the uneven and sharp shapes of lack-of-fusion pores and cracks create areas where stress builds up, which speeds up the formation and growth of cracks when under pressure [116]. Moreover, a reduction in laser power leads to a gradual decrease in the fraction of keyhole and gas pores.

*3.2.2.2. Keyhole pore.* In general, the grain structure of the SLM sample displayed significant complexity due to recurrent remelting and differing orientations among the deposited layers. As can be seen from Fig. 10(a), coarser grains developed in the HAZ surrounding the molten pool, influenced by elevated thermal exposure. Conversely, the centre area of the molten pool, insulated from the thermal influences of succeeding layers, exhibited directional solidification primarily governed by vertical heat transfer from the topmost layer downward [75]. As a result, columnar grains formed in a direction opposite to the prevailing thermal gradient. The ongoing expansion of columnar grains resulted in a significant distance between the liquid front and the molten pool boundary, hence complicating heat dissipation. Subsequently, the temperature differential of the melt would diminish, and there was no notable directionality, so impeding the further development of columnar grains.

Keyhole pores are one of the most common volumetric flaws observed in metal additive manufacturing. The speed of the laser and the thickness of the powder layer are important factors that directly impact how the melt pool behaves and therefore, greatly affect the development of porosity [50]. This phenomenon (Fig. 10(b)) also arises when the viscous melt, influenced by material evaporation, surface and subsurface Marangoni convection, recoil pressure generated by evaporation, and gas expansion, contributes to the formation of a keyhole during the SLM process [118]. Wu et al. [45] explained the fabrication of the keyhole phenomenon for SLM Mg alloy. As shown in Fig. 10(c), the bottom of the keyholes can easily reach evaporation temperature due to Mg having a low temperature and turning into vapour quickly. Mg possesses a low dynamic viscosity of approximately 1.25 mPa s at 650 °C, a boiling point of 1091 °C, and an evaporation enthalpy of 5.272 kJ $kg^{-1}$ at ambient pressure [119]. These characteristics promote rapid evaporation of Mg, which reacts with residual oxygen in the selective laser melting chamber to form magnesium oxide (MgO), accompanied by significant heat release. This reaction elevates recoil pressure and reduces surface tension, thereby facilitating the stabilisation of open keyholes during the melting process [120]. However, as the upper region of the keyholes began to cool, the surface tension increased, leading to the closure of this region and the subsequent formation of pores. Meanwhile, with additional laser irradiation of the depressed area, the recoil pressure escalated once again, producing a vigorous downward melt flow that propelled the pores farther into the melt pool, resulting in an increase in the final part porosity [121]. Similarly, Khairallah et al.

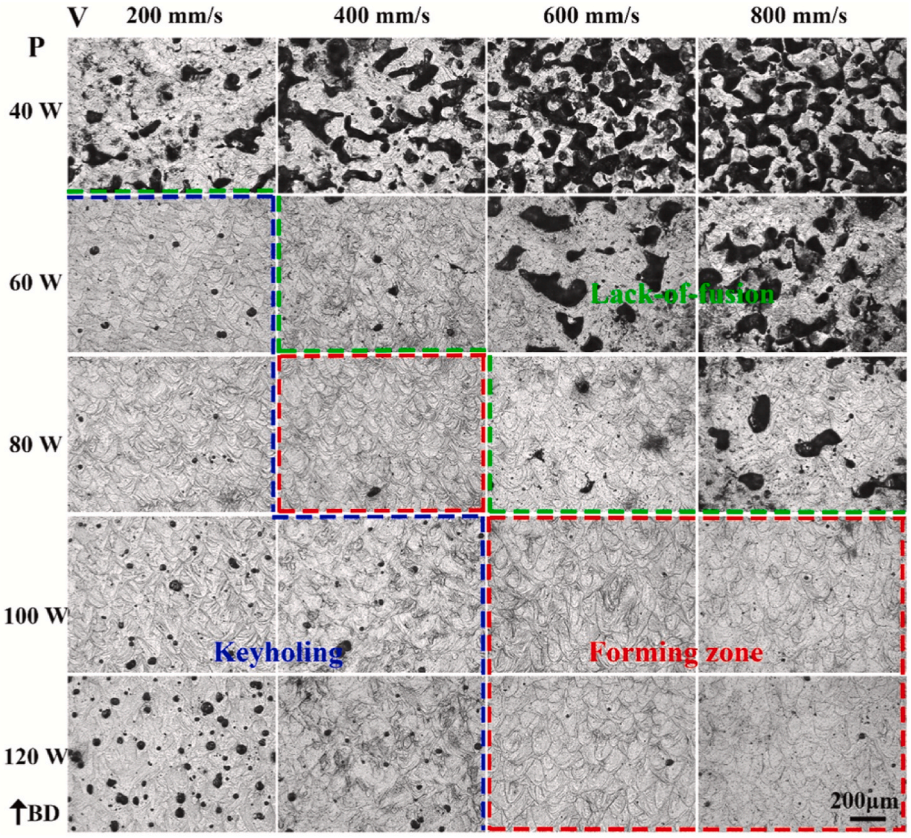


(a)

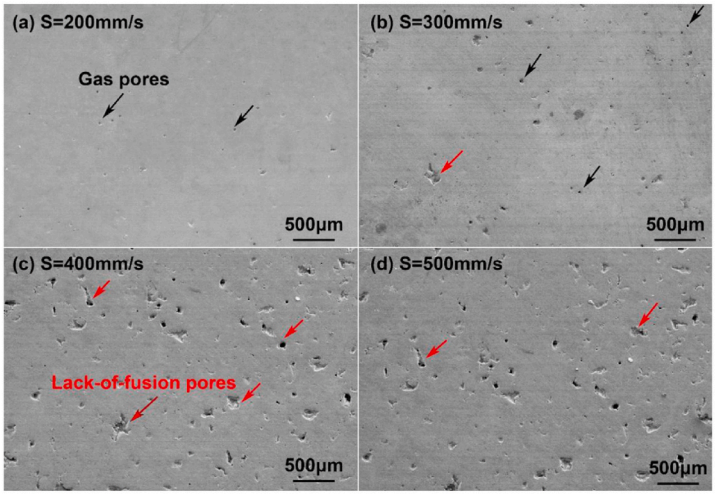


(b)

**Fig. 9.** Surface internal pores and morphologies of SLM-fabricated (a) Mg [117] and (b) AZ91D at different scanning speeds [112].

[122] extensively investigated the fluid dynamics associated with laser irradiation during the SLM Mg process, emphasising the key roles of recoil pressure, Marangoni convection, and evaporative and radiative surface cooling. Their study demonstrated that recoil pressure, generated by intense metal vaporisation, is the dominant force driving the formation of keyhole-shaped cavities (Fig. 10(d)). These defects are often accompanied by complex hydrodynamic behaviours, including surface-driven Marangoni flow and internal vortex formation within the melt pool [108]. The development of vortex flows, induced by thermal gradients and surface tension effects, intensifies melt pool agitation and raises the local surface temperature. Concurrently, an increasing vapour stream and surface deformation further compromise the stability of the melt pool. As the solidification front progresses upward, these unstable conditions may entrap gas bubbles prior to their escape, leading to the creation of permanent pores in the solidified substance [69]. This mechanistic insight highlights the intricate coupling of thermal and fluid

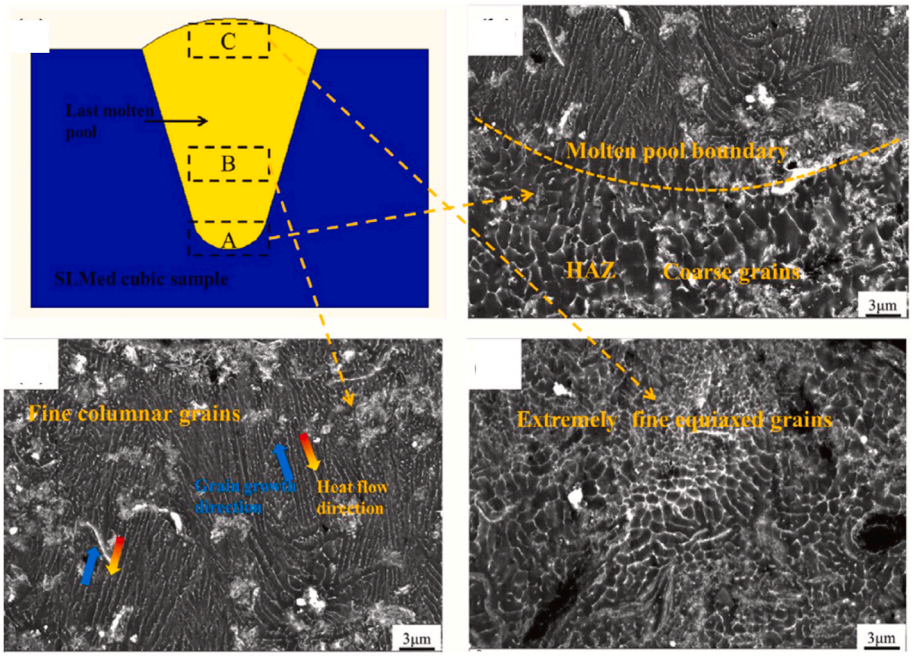


(a)


(b)

**Fig. 10.** (b) A keyhole defect [123], the evolution of (c) the keyhole phenomenon [45], and (d) a fluid dynamic simulation depicting the formation of a keyhole [122].

flow phenomena in SLM and underscores the importance of optimising process parameters to suppress defect formation.

Process parameters in additive manufacturing critically influence the molten pool's shape and dynamics, enabling control over the solidification behaviour and resulting grain structure. Wang et al. [124] reported that both the depth and width of the molten pool increase with higher laser power due to the elevated peak temperature and larger laser spot size. Based on this observation, at lower laser power settings, the molten pool exhibits characteristics of a keyhole mode. As the laser power increases, a distinct circular cavity appears in the molten pool, indicating the transition to a deep keyhole mode. In this regime, Marangoni convection becomes more complex compared to the conduction mode, complicating the melt pool dynamics [91].

Consequently, the rapid solidification rate may trap gas from entrapped pores in the original powder, residual argon in the build chamber, and evaporated Mg in the molten pool, leading to the formation of internal circular pores (Fig. 11). Moreover, the cellular dendrites tend to grow nearly perpendicular to the melt pool boundary, opposing the direction of maximum heat flow. So, the shape of the molten pool directly affects how the dendrites grow and, in turn, influences the crystal structure of the finished sample [125].

*3.2.2.3. Gas pores.* On the other hand, Shi et al. [68] observed porosity-induced void features on the tensile fracture surface, where the gas pores appeared larger than the surrounding equiaxed microstructures. The melt pool mainly has areas with tree-like, layered, and stringy structures, along with wavy patterns around the gas pores. Zu et al. [126] evaluated the effect of laser power and hatch spacing of AZ91D alloy by SLM. The average diameter of the keyhole is 600 μm. They found that a regular pore structure gradually disappeared with a decrease in hatch spacing. These porosities can be categorised into two groups. Distinct voids were created from unmelted powder and trapped shielding gas, whereas reaction blowholes emerged due to the cooling of Mg vapour that could not escape the rapidly solidifying molten pools [127]. Xu et al. [128] investigated the influence of varying scanning speeds and hatch spacing on the SLM process of NZ30K Mg alloy. They suggested that with increasing scanning speed, the porosity initially decreases, resulting in a nearly dense structure, but then gas pores

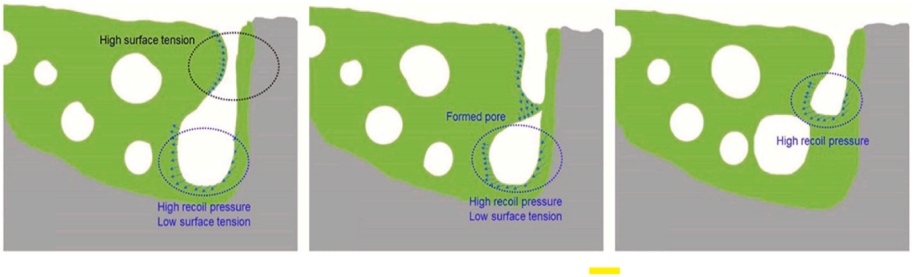


(c)

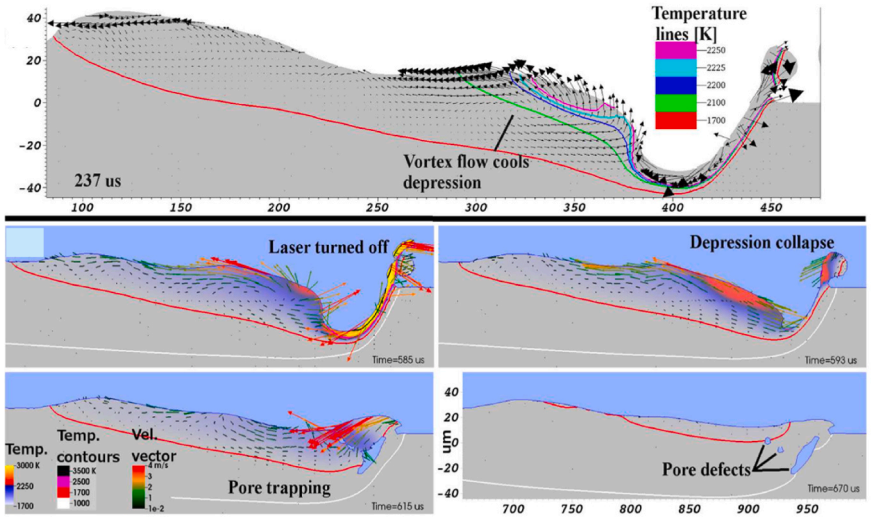


(d)

**Fig. 10.** (*continued*).

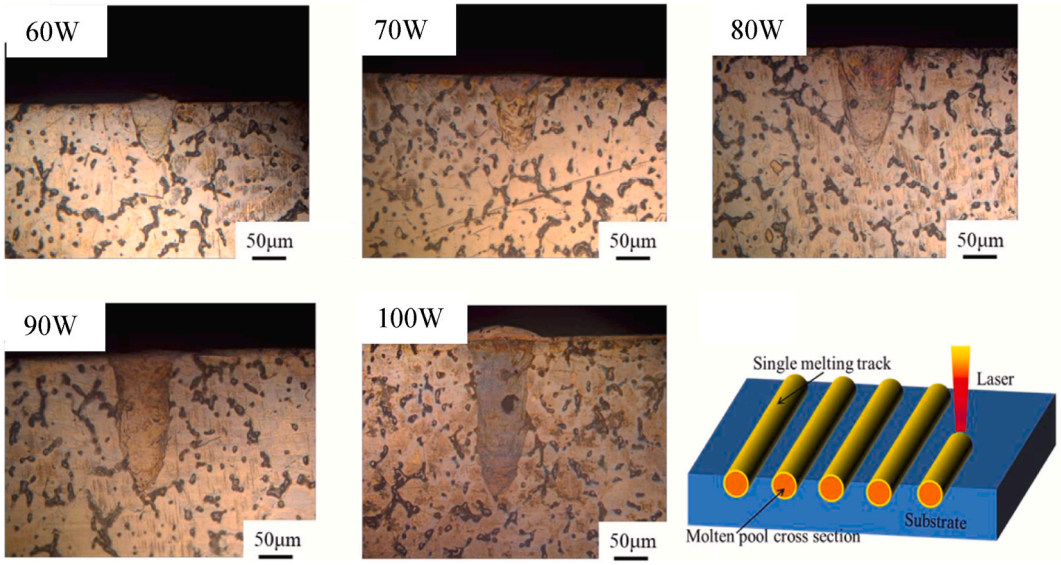


**Fig. 11.** The effect of laser power on the development of a keyhole defect [124].

increase at higher velocities. The types of gas porosity can be broadly categorised into three regions: (1) an excessive evaporation zone characterised by moderate gas porosity, (2) a stable forming zone, and (3) an incomplete fusion zone, where lack-of-fusion defects are predominant. The gas pores, typically round or elliptical, form from trapped metal vapour at high laser energy densities [70], while irregularly shaped

unfused defects result from incomplete powder melting at lower energy densities. The fabricated parts exhibit a microstructure composed of lamellar regions, along with both equiaxed and columnar grains [70]. Interestingly, with an increase in laser energy density, both the average grain size and variation decreased significantly. Fig. 12 illustrates light microscope findings that highlight gas-induced porosity in the WE43 alloy L-PBF [70].

A comparable result was published as well by Yin et al. [30], where at high energy input, circular pores were observed, whereas low energy input tended to result in lack-of-fusion defects; however, intermediate laser power and scanning speed resulted in an exceptionally dense component. The laser power had a greater impact on energy density than the scanning velocity. They also found that pores tend to form at the junctions of the porous scaffold. Poor heat dissipation at these points due to large overhang angles and thin walls makes it harder to remove heat, as most of them only dissipated through the solid metal [130]. This increased the molten pool temperature, and intense vaporisation caused keyhole collapse, leading to gas pore formation. A greater layer thickness resulted in a deeper keyhole. Also, Liu et al. [50] observed that increasing laser power at a fixed scanning speed significantly reduced gas pore formation, whereas increasing both laser power and scanning speed resulted in a lack of fusion defect. The results aligned with the findings of gas pores on the sample. Wang et al. [67] found that using too little or too high energy density during processing can lower the relative density and make the round pores tend to form in the samples. This is because excessively low or high energy density disrupts the melt pool convection, making it more difficult for gas to escape from the molten pool. On the other hand, Xie et al. [131] examined the influence of zinc content on the porosity properties of Mg–xZn–0.2Mn alloys produced via SLM. They mentioned that increasing the Zn content results in an increase in gas pore formation.

In SLM of Mg alloys, porosity formation, including lack-of-fusion, keyhole, and gas pores, significantly impacts the mechanical properties and integrity of the final part. Lack-of-fusion porosity is primarily caused by insufficient overlap between adjacent melt tracks, resulting from inadequate melt pool size or poor scan strategy [86]. Keyhole porosity, in contrast, occurs under high energy input where intense vaporisation leads to keyhole instability and collapse, trapping gas within the melt [94]. This effect becomes more pronounced with increased layer thickness. Gas porosity originates from the entrapment of residual gases, such as argon or vaporised Mg, due to its low boiling point and the rapid solidification rate [132]. Each porosity type is influenced by different process parameters, making their control complex. To minimise porosity, parameters such as laser power, scan speed, hatch spacing, and layer thickness must be carefully optimised based on the desired microstructure, part performance, and powder characteristics [133,134]. Sufficient processing tolerance is essential to ensure consistent, high-density components.

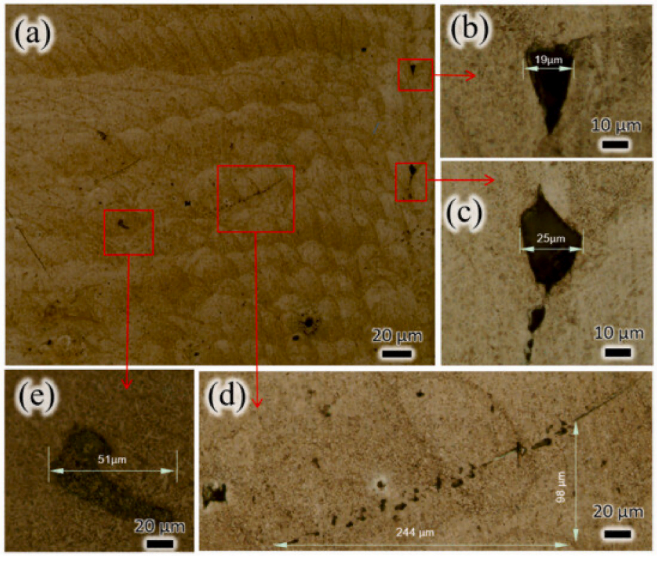


**Fig. 12.** Optical microscope images of gas pore defects in SLM-fabricated WE43 alloy [129].

## 4. Microstructure characteristics

In SLM, the formation of textured columnar grain formations often leads to significant anisotropy in mechanical properties, presenting an important challenge in the progression of additive manufacturing. This microstructural feature arises from the combined effects of epitaxial grain development at the melt pool boundary and competitive growth between surrounding grains during solidification [135]. In the SLM process, the motion of the laser heat source results in a temperature decrease at the leading edge of the molten pool, causing solidification to commence as it falls below the liquidus temperature [136]. Dendritic structures begin epitaxial growth from the base of the molten pool, generally displaying a cellular appearance, as shown by Wang et al. [95]. The growth direction of grains in SLM typically aligns with the maximum thermal gradient, directed from the top surface of the molten pool downward. This leads to epitaxial grain development from remelted sublayers or the substrate in the build direction. As the molten pool temperature decreases, equiaxed crystals begin to form ahead of columnar tips [137]Their growth direction initially appears perpendicular to the laser scan (Fig. 13(a)), then gradually shifts along the scan direction due to increased undercooling along the heat flow direction. Dendrite arms grow faster along this gradient. Additionally, solute segregation occurs, with low concentrations in dendrite cores and enriched regions between dendrites.

Bar et al. [138] reported that micrographs of WE43 fabricated via SLM exhibit a three-zone microstructural evolution (Fig. 13(b)). Equiaxed zones were identified from the surface to the centre of the melt pool. Certain features clearly originate from a partially molten region that surrounds the entirely molten volume during the short melting period. At the lower region of the melt pool, thin, nearly parallel lines constituting a lamellar zone are noticed. The HAZ is the unmelted area of a material where microstructural and property modifications [76] occur as a result of exposure to elevated temperatures during thermal processing. The gradual transition of the microstructure from lamellar to equiaxed morphology is attributed to the reduced cooling rate and thermal gradient [68]from the periphery to the centre of the melt pool during solidification. The pole figures presented in Fig. 13(c) clearly reveal the texture evolution during SLM WE43 alloy processing, which can be categorised into three distinct regions. In Region I, columnar grains are primarily elongated along the z-direction, with their intensity concentrated near the melt pool boundary [139]. Region II represents a lamellar structure, formed due to laser scanning mainly along the y-direction. In Region III, large Mg grains exhibit a strong orientation along the z-direction, aligned with the laser scanning and build direction. Zumdick et al. [140] compared the grain sizes of WE43 Mg alloy samples fabricated by SLM, powder extrusion, and conventional casting, as illustrated in Fig. 13(d). The SLM samples exhibited fine, uniform grain structures, with sizes ranging from 0.4 to 2.9 μm and an average grain size of approximately 1.0–1.1 μm across all three orthogonal cross-sections of the cubes. The powder-extruded samples showed slightly coarser grains, with an average size of 1.3 μm in both longitudinal and transverse directions, and demonstrated minimal variation across different planes. In contrast, the as-cast material presented significantly larger grains, averaging 44.3 μm. Compared to conventionally processed materials, SLM-fabricated components generally possess more homogeneous and refined microstructures [141]. This is primarily due to the characteristics of powder-based processing and the rapid cooling rates inherent to SLM, which promote the formation of equiaxed grains. As a result, Mg alloys produced by SLM often exhibit

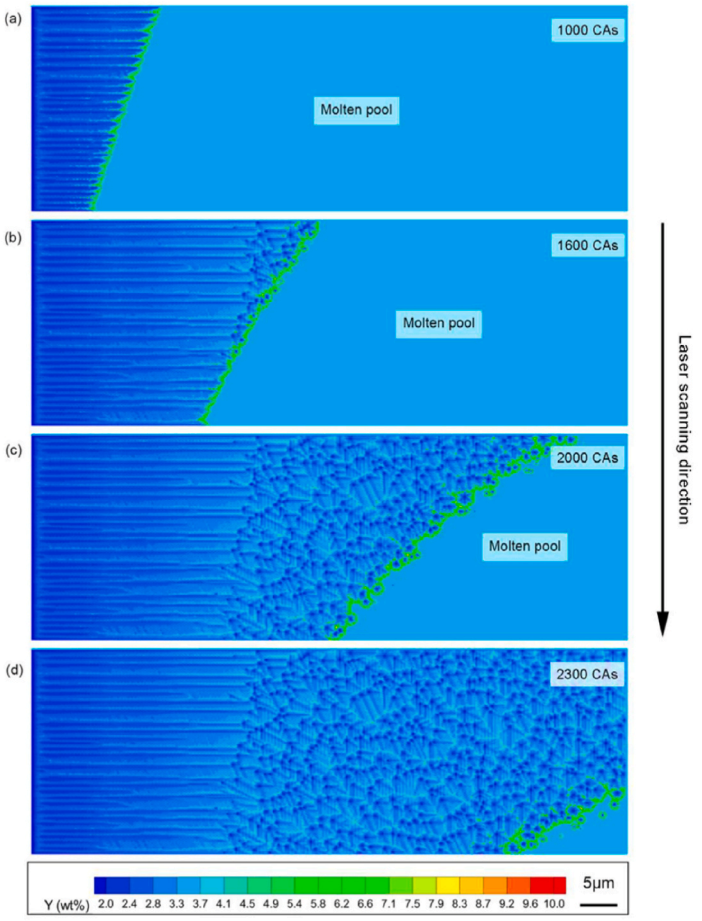


(a)

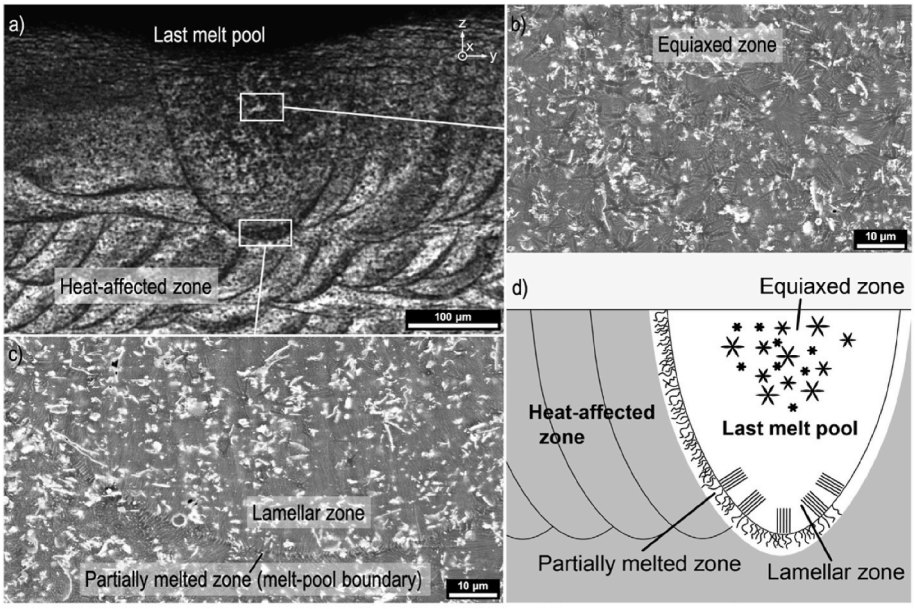


(b)

**Fig. 13.** (a) Grain growth direction [95], (b) microstructural evolution [138], (c) texture distribution, and (d) grain size comparison of Mg alloys produced by different fabrication techniques [140].

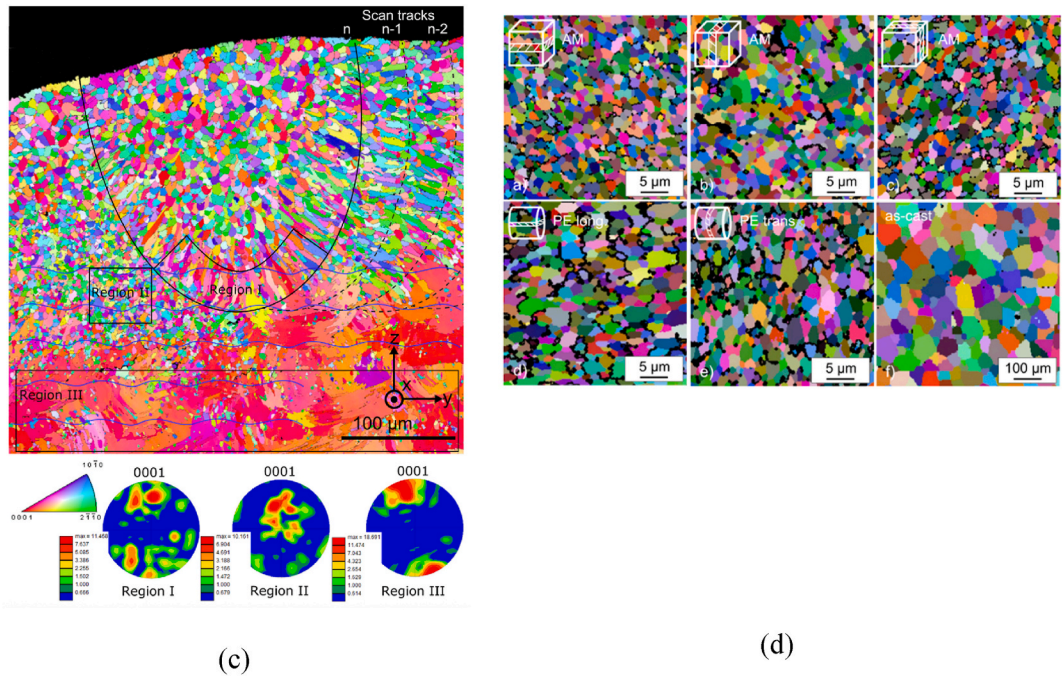


**Fig. 13.** (*continued*).

enhanced mechanical properties.

In general, the evolution of grain size during SLM is mainly affected by the temperature gradient (G), solidification rate (R), and cooling rate (T = G × R) [142]. A higher solidification rate typically leads to a reduced grain size. The ultrahigh cooling rates characteristic of SLM, ranging from $10^3$ to $10^4$ K/s, generate substantial temperature differences inside the melt pool [44]. These conditions significantly limit the growth period for both primary grains and regenerated secondary sub-grains. A notable temperature divergence generates a surface tension gradient, thereby initiating thermal convection within the melt pool [83]. This process facilitates the remelting of columnar dendrites, resulting in their transformation into smaller secondary grains and a decrease in average grain size [143]. Empirical evidence indicates that elevated solidification rates promote a transition from columnar to equiaxed grains, whereas greater cooling rates improve microstructural refinement. Furthermore, the G/R ratio is essential in determining the final grain morphology [6]. Lower G/R values facilitate the formation of equiaxed structures, whereas higher G/R values lead to the emergence of columnar grains (Fig. 14).

## 5. Corrosion and biodegradable

The unique thermal cycle in SLM, featuring localised melting and fast solidification, generates a fine-grained, equiaxed, and cellular-dendritic microstructure within the melt pool core. According to the Hall–Petch relationship, fine grains typically improve mechanical characteristics; however, they tend to facilitate uniform corrosion rather than localised degradation [144]. Grain boundaries may act as active corrosion pathways, particularly in the presence of impurity segregation. Some magnesium alloys made using SLM, like ZK60 (Mg–Zn–Zr), can have mixed metal phases such as MgZn, $MgZn_2$, and compounds rich in Zn–Zr, while alloys like WE43 (Mg–Y-RE-Zr) can develop stages rich in Y or rare earth metals; these phases can act as a positive electrode compared to the main magnesium structure, leading to small-scale corrosion in body-like environments [145].

The Mg matrix adjacent to the intermetallic undergoes preferential corrosion, resulting in localised degradation. Also, body fluids, particularly blood plasma, are rich in chloride ions ($Cl^-$) and simulate strong

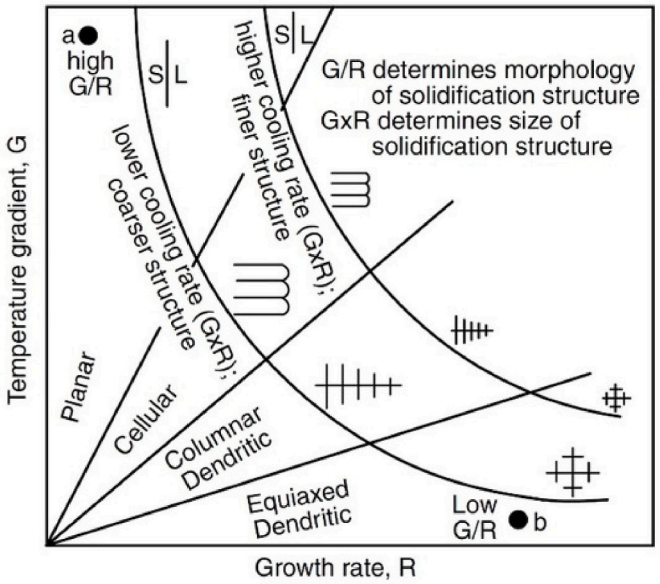


**Fig. 14.** A solidification map showing that the temperature gradient and growth rate influence microstructural shape and grain size [142].

corrosive environments. Mg deteriorates swiftly in physiological conditions, resulting in the release of hydrogen gases, the creation of alkaline contaminants, and severe material loss. The interaction of the metal within the physiological pH range of 7.35–7.45, typical of human extracellular fluids, is particularly significant due to its elevated chemical reactivity in aqueous conditions. The primary corrosive mechanism is expressed by Gonzales et al. (2018) [146],

$$\text{(Anodic) } Mg \rightarrow Mg^{2+} + 2e^- \quad (1)$$

$$\text{(Cathodic) } 2H_2O + 2e^- \rightarrow H_2\uparrow + 2OH^- \quad (2)$$

$$Mg + 2H_2O \rightarrow Mg(OH)_2 + H_2\uparrow \quad (3)$$

Chloride ions ($Cl^-$) from body fluids can break down $Mg(OH)_2$, accelerating corrosion:

$$Mg(OH)_2 + 2Cl^- \rightarrow MgCl_2 + 2OH^- \quad (4)$$

Uncontrolled corrosion of Mg implants in physiological environments can result in premature structural failure, weakening the structural support necessary for the recovery process. Additionally, the rapid degradation may lead to localised pH increases and the accumulation of corrosion byproducts, which can irritate surrounding tissues and trigger inflammatory responses [147]. These adverse biological reactions can hinder tissue regeneration, delay healing, and ultimately affect the biocompatibility and clinical success of the implant. Non-uniform corrosion can lead to the creation of pits, which act as stress concentrators, significantly increasing the risk of implant fracture under physiological loads and potentially resulting in premature failure before proper bone healing occurs [148]. Uneven wear can cause a large and quick release of metal ions, like $Zn^{2+}$, $Y^{3+}$, and $RE^{3+}$, which might lead to harmful or inflammatory responses in the body [149]. Fig. 15 illustrates the laboratory assessment methods and corresponding levels of difficulty involved in evaluating the corrosion behaviour and biodegradability of magnesium alloys. Uncontrolled corrosion of magnesium implants in physiological environments can result in premature structural failure, compromising the mechanical support required during the healing process. Also, the quick disintegration might raise pH levels in certain areas, leading to corrosion from accumulation, which could irritate adjacent tissues and induce discomfort [150].

### 5.1. In-vitro evaluation

Corrosion testing for Mg and its alloys is crucial because magnesium is highly reactive, especially in moist or saline environments. Corrosion testing of magnesium often involves immersion testing (ASTM G31), where samples are exposed to solutions such as sodium chloride (NaCl), Hanks' solution, Simulated Body Fluid (SBF), Phosphate Buffered Saline (PBS), or Dulbecco's Modified Eagle Medium (DMEM) for defined periods, and deterioration is measured using weight loss, hydrogen evolution, and variations in pH [152]. The corrosion rate is calculated as mass loss per unit area over time. For example, salt spray testing (ASTM B117) accelerates atmospheric oxidation by exposing samples to a 5 % NaCl mist. In addition, a renowned technique, such as electrochemical testing (ASTM G5, G59, and G106), is used to measure the decomposition behaviour of Mg in electrolytes like 3.5 wt% NaCl or SBF through potentiodynamic polarisation to identify $E_{corr}$, $I_{corr}$, and EIS for assessing corrosion resistance and protective film properties. Here, the hydrogen evolution test is straightforward for assessing the degradation rate of Mg. In vitro biodegradation testing involves gravimetric testing, which includes weighing the sample before and after corrosion exposure [153]. Corrosion products are removed following ASTM G1, then evaluated by surface appearance and mass loss.

Early investigations into the corrosion behaviour of SLM Mg alloys, such as the study by Ning et al. [154] revealed that the Zn–3Mg alloy exhibited enhanced corrosion resistance compared to pure Mg, demonstrating a reduced degradation rate of 0.0886 mm/year. Also, Lovašiová et al. [145] established that the potential for corrosion of SLM WE43 is substantially more positive than that of the as-cast sample, which is related to the existence of oxides demonstrating more noble galvanic behaviour. The formation of phosphate compounds during corrosion enhances biocompatibility by promoting bone ingrowth and osseointegration, owing to their similarity with bone minerals [155, 156]. A deterioration rate of 2.6 mm/year is reasonable for devices like 5 mm-thick skeletal fasteners, allowing degradation within approximately one year. Similarly, Suchý et al. [130] examined the ability to withstand corrosion of the SLM WE43 alloy in Hanks' salt solution, focusing on the effect of surface condition. SLM samples displayed a corrosion value of 2.11 mm/year, yet as-built specimens revealed a markedly elevated rate of 7.04 mm/year. This substantial difference, when compared to extruded material, is attributed to the faster corrosion caused by the irregular distribution of secondary phases and silicon inclusions in the specimens [157]. Raducanu et al. [158] fabricated Mg–10Zn-0.8Ca-0.5Zr alloy using SLM to develop 3D-printed samples for biodegradable implant applications. The oxidation activity was investigated in PBS solution at three distinct pH values, exhibiting stable and excellent performance. At physiological pH, the alloy exhibited a rate of 1.426 mm/year, indicating its potential suitability for biomedical use. In contrast, a lower degradation rate of 0.2 mm/year was reported for SLM ZK60, compared to 0.42 mm/year for cast ZK60, indicating that the corrosion resistance of the SLM alloy was higher. A similar finding was also mentioned by Wu et al. [45].

#### 5.1.1. Alloying element

In Mg alloys for medical purposes, alloying elements enhance durability, corrosion resistance, and processability. However, biocompatibility and degradation control remain major challenges. Many alloying elements traditionally used in Mg alloys may not be safe for long-term implantation due to potential toxicity or adverse biological effects (Table 4).

Mg is well-known for being strong and safe for the body, which makes it a good choice for temporary medical implants, especially because its elastic modulus (~45 GPa) is similar to that of cortical bone (~10–30 GPa) [26]. This similarity helps minimise the problem of stress shielding, a phenomenon in which implants that are significantly stiffer than bone carry most of the load, causing surrounding bone tissue to

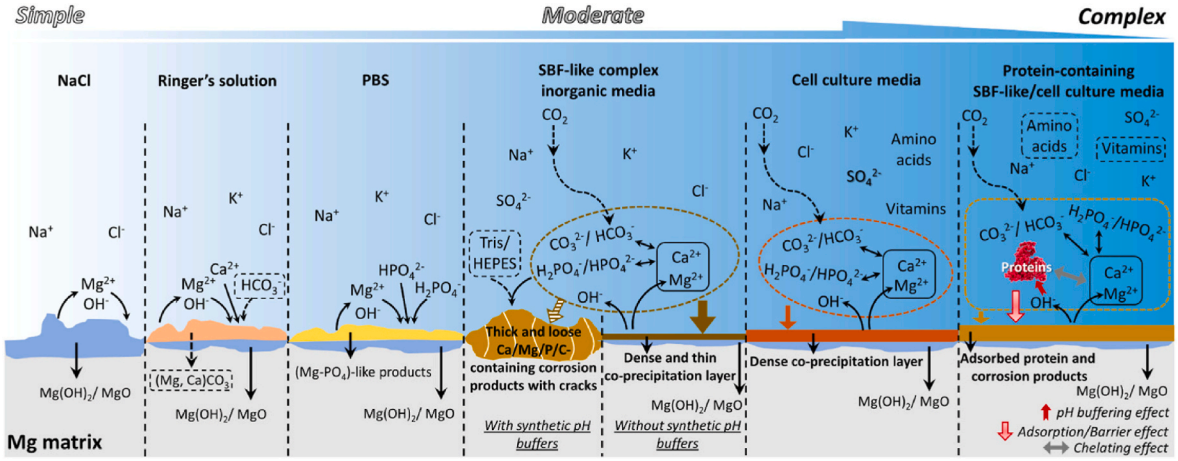


**Fig. 15.** The laboratory evaluation methods and associated levels of difficulty in assessing Mg alloys for biomedical applications [151].

**Table 4**
The biomedical implications of alloying elements within the biomedical domain

| Element | Reason for Use | Biomedical Concern |
|---|---|---|
| Aluminum (Al) | Strengthening (common in AZ series) | Neurotoxicity associated with Alzheimer's disease [159]. |
| Zinc (Zn) | Improves strength, corrosion | Acceptable in minimal quantities; nevertheless, excessive zinc is cytotoxic [160]. |
| Rare Earth Elements (REEs) | Grain refinement, corrosion resistance | Ambiguous long-term biocompatibility and possible buildup in the liver and kidneys [161] |
| Manganese (Mn) | Improves corrosion resistance | Typically biocompatible; however, it requires regulation [162]. |
| Copper (Cu) | Antibacterial strength | Toxic at high concentrations; may cause liver and kidney damage [163]. |

weaken over time due to reduced mechanical stimulus. Despite its beneficial modulus, Mg magnesium exhibits some significant mechanical constraints that hinder its adoption in clinical settings, especially in load-bearing orthopaedic implants like screws, plates, and pins [164]. Alloying Mg with elements like zinc, calcium, or rare earth metals enhances its structural strength, improves resistance to corrosion, and promotes stable degradation behaviour, thereby extending its suitability for safe biomedical applications. Table 5 demonstrates the effects of manufacturing parameters on the mechanical properties of SLM Mg alloys.

To eradicate this problem, researchers are attempting to restrict the amount of alloying elements that are prone to generating significantly cathodic intermetallic phases. Utilising materials with more suitable electrochemical potentials, such as calcium or minimal levels of zinc, can mitigate microgalvanic corrosion [171] and encourage more uniform deterioration. Xie et al. [172] conducted a systematic assessment of the influence of manganese content on the biocompatibility of SLM ZK30-0.2Cu-xMn alloys. At lower amounts of manganese (0.4–1.2 %), more cells survived; however, at 1.6 % manganese, there was a small amount of cell damage, showing a good range for medical use. Also, Shuai et al. [173] examined the influence of copper content, ranging from 0.2 to 0.8 wt%, on the cytotoxicity of the SLM-ZK60-xCu alloy. This study indicated that the ZK60-xCu alloy groups showed significant antibacterial characteristics. On day 5, MG63 cells exposed to the ZK60-0.8Cu alloy demonstrated comparatively lower relative growth rate (RGR) values than those with the virgin ZK60 alloy; yet, the values remained under an acceptable cytotoxicity threshold. On the other hand, Xu et al. [174] confirmed that alloys with higher copper content (e.g., ZK30-0.2Cu, ZK30-0.3Cu) likely show lower bacterial counts (reduced CFU/mL) over time compared to ZK30. The base ZK30 probably exhibits the weakest antibacterial effect, with higher CFU/mL values. Again, Shuai et al. [173] examined the insertion of varying quantities of calcium oxide (CaO) to enhance the morphology and dispersion of secondary phases in SLM-AZ61 alloys. They want to boost the biocompatibility of the alloy. The study revealed that AZ61-9CaO demonstrated favourable cytocompatibility and offers prospects as a suitable material for knee implants [175,176].

Also, Xie et al. [131] evaluated the influence of the zinc level on the corrosion attributes of SLM Mg alloys, aiming to improve their use in biomedical fields. The experiment was conducted through immersion tests in Hanks' solution. It was revealing that higher Zn content led to more distinct grain boundaries and a decrease in oxidation resistance [177], resulting in more evident localised deterioration following immersion. Xie et al. [178] reported that alloying Mg with manganese promoted the formation of a relatively protective manganese oxide layer on the sample surface, thereby enhancing its biodegradation resistance. However, when the Mn content exceeded 0.8 wt%, the presence of undissolved Mn phases negatively impacted biodegradation resistance, offsetting the beneficial effects of the oxide layer. Yao et al. [179] integrated an additional minor amount of calcium (Ca), in conjunction with a Ca–Zn combination, into magnesium alloys during the SLM to enhance corrosion resistance. The corrosion rate diminished to 1.0 mm/year for laser-processed Mg–0.6Ca and to 0.7 mm/year for SLM Mg–0.5Zn–0.3Ca. The decrease in corrosion rate was attributed to the confinement of impurity elements [180], the presence of MgO, and the consequent increase in self-corrosion potential. Early work by Long et al. [181] identified Mg–3Zn-1Dy (where Dy = dysprosium) as a viable choice for implant possibilities, owing to its significantly lower degradation rate compared to other Mg alloy compositions. The research demonstrated that the second-phase composition and particle size were essential for enabling Mg–3Zn-1Dy to exhibit the lowest average hydrogen evolution rate. Dysprosium content varied from 1 to 5 wt% in their experiments. Shuai et al. [173] incorporated graphene oxide (GO) as a secondary phase into SLM AZ61 alloys, leading to grain encapsulation within a honeycomb-like nanostructure. The distinctive architecture did not conclusively offer a significant improvement in durability against corrosion [182]. The incorporation of 0.1 % GO resulted in a decrease in corrosion current density (Icorr) relative to the untreated AZ61 alloy. In addition, Yang et al. [62] used the rare earth metal scandium (Sc) as a component of alloying to produce Mg(Sc) powder, which was further manufactured into an implant via SLM. The SLM Mg(Sc) alloy demonstrated a comparatively low rate of decay of 0.61 mm/year, indicating its potential suitability for biomedical applications. SLM-processed Mg(Sc) promotes matrix dispersion and the formation of extensive solid solution particles due to rapid heating and cooling rates, which maintain the original supersaturated structure. Immersion studies demonstrated that elevated scandium levels markedly enhanced the corrosion resistance of the Mg matrix due to the development of a protective corrosion film coating. Fig. 16 shows (a) surface morphology after SBF immersion, (b) elemental analysis of the selected area, and (c) XRD of corrosion products.

### 5.1.2. Heat treatment

Heat treatment is frequently used for Mg components fabricated by SLM to improve their corrosion resistance by reducing internal stresses, improving microstructural uniformity, and reducing residual defects that may act as initiation sites for corrosion [183]. Table 6 presents the standard hardening and temper designations applicable to Mg alloys, as defined by the ISO 2107:1983 specification.

Like, Esmaily et al. [42] utilised hot isostatic pressing (HIP) and heat treatment (HT) to improve morphology and corrosion resistance. of WE43 alloy fabricated via the SLM method. The combination of HIP and HT exhibited enhanced corrosion resistance relative to both the untreated and singular HIP versions. Microstructural changes in the solid-solution matrix caused by high cooling rates, combined with oxide particles originating from powder solidification [184], significantly improve the corrosion resistance. Ling et al. [100] enhanced the anisotropy and multilayer microstructure of SLM WE43 alloy by employing heat treatment to facilitate the heterogeneous precipitation of Nd-rich intermetallic. T4-treated samples (solutionized at around 525 °C, air-cooled, and naturally aged) exhibited reduced $I_{corr}$ values and an enhanced corrosion barrier. The homogenised microstructure obtained via post-treatment significantly mitigated micro-galvanic corrosion and promoted the development of a protective passivation film [185]. Also, stress relief annealing can be applied to SLM-Mg alloys to mitigate stress corrosion cracking (SCC), thereby enhancing both mechanical performance and resistance to deterioration. Like, Wang et al. [186] employed a combination of hot rolling and annealing at 400 °C for 1 h to enhance the morphology and resist corrosion of SLM-AZ91 alloys. The corrosion rate significantly dropped from 31.6 to 7.2 mm/year, largely attributable to the reduced presence of flaws and the generation of small particles. These microstructural features significantly diminished pitting and micro-galvanic degradation by functioning as barriers that impeded corrosion production.

**Table 5**
The effect of processing parameters on the mechanical performance of SLM Mg-alloys

| SLM | Material | Laser power (W) | Scanning Speed (mm/s) | Hatch Spacing (mm) | Layer Thickness (mm) | Energy Density (J/mm$^3$) | Relative density (%) | Ultimate Tensile Strength (MPa) | Yield Strength (MPa) | Young's Modulus (GPa) | Elongation (%) | References |
|---|---|---|---|---|---|---|---|---|---|---|---|---|
| ProX DMP320 | WE43 | 150–250 | 800–1200 | 0.1 | 0.03 | 74–104 | 98.5–99.5 | 261–287 | 210–218 | 44–45 | 4.1–10.1 | Shi et al. [68] |
| EOS M290 | ZK60 | 30–120 | 60–600 | 0.06–0.12 | 0.03 | 73–583 | 83.0–98.0 | 180–250 | 100–250 | | 8.1–15.5 | Liang et al. [102] |
| LSFN-I | Mg-5.5Zn | 180 | 700 | 0.07 | 0.02 | | | 70–159 | | | 1.6–10.9 | Wei et al. [165] |
| E-Plus 3D M250 | AZ91D | 50 | 200–500 | 0.03 | 0.03 | 111–278 | 85.0–98.1 | 210–335 | 170–280 | | 1.1–5.8 | Niu et al. [112] |
| ZRapid 150 | AZ91D | 50–150 | 200–700 | 0.1 | 0.03 | 15–250 | 88.1–99.1 | 275–390 | 160–235 | | 1.1–8.9 | Li et al. [113] |
| HK M300 | AS41 | 110–270 | 300–1000 | | | 48–126 | | 100–300 | | | 4.0–12.0 | Yang et al. [62] |
| HK M300 | WE43 | 200 | 100–1600 | 0.06, 0.09, 0.12 | 0.02 | | | 202–350 | 160–317 | | 0.1–4.9 | Xu et al. [128] |
| BLT S210 | WE43 | 40–160 | 400–1400 | 0.07 | 0.01–0.04 | | 99.5–99.7 | 125–250 | 540–460 | 2–3 | 1.4–2.8 | Yin et al. [56] |
| GDINM-D150 | WE43 | 80–200 | 250–650 | 0.05–0.08 | 0.04 | 45–400 | 78.8–97.4 | | 157–351 | 39–47 | 6.5–14.5 | Chang et al. [94] |
| ReaLizer 50 | AZ31 | 60–90 | 90–160 | 0.1 | 0.05 | | | | 150–185 | | 7.5–8.1 | Pawlak et al. [166] |
| Forwedo LM-120 | AZ61 | 150 | 250–1800 | 0.06, 0.08, 0.1 | 0.04 | 139–208 | 86.1–97.4 | 149–287 | 99–233 | | 2.1–5.2 | Liu et al. [58] |
| Forwedo LM-120 | AZ61 | 150 | 400 | 0.06 | 0.04 | | | 233–287 | 126–274 | | 3.3–8.1 | Liu & Guo [167] |
| ZRapid 150 | GZ151K | 200 | 700 | 0.07 | 0.03 | | | 277–428 | 184–410 | | 2.9–4.8 | Fu et al. [168] |
| LSFN-I | Mg–Gd | 200 | 500–700 | 0.06–0.08 | 0.02 | | | 230–410 | 210–380 | | 4.1–13.1 | Yuan et al. [135] |
| ZRapid 150 | GZ112K | 80 | 200 | 0.1 | 0.02 | | | 287–351 | 183–332 | | 9.3–14.3 | Deng et al. [125] |
| GDINM-D150 | Mg–Al | 60–150 | 400–600 | 0.04–0.05 | 0.04 | | 71.8–99.7 | 320–350 | 275–315 | | 8.9–10.4 | Chang et al. [169] |
| SLM 280HL | Mg–3Y | 60–240 | 200–1500 | | 0.05 | | 99.8 | 180 | 113 | | 1.1 | Minárik et al. [170] |

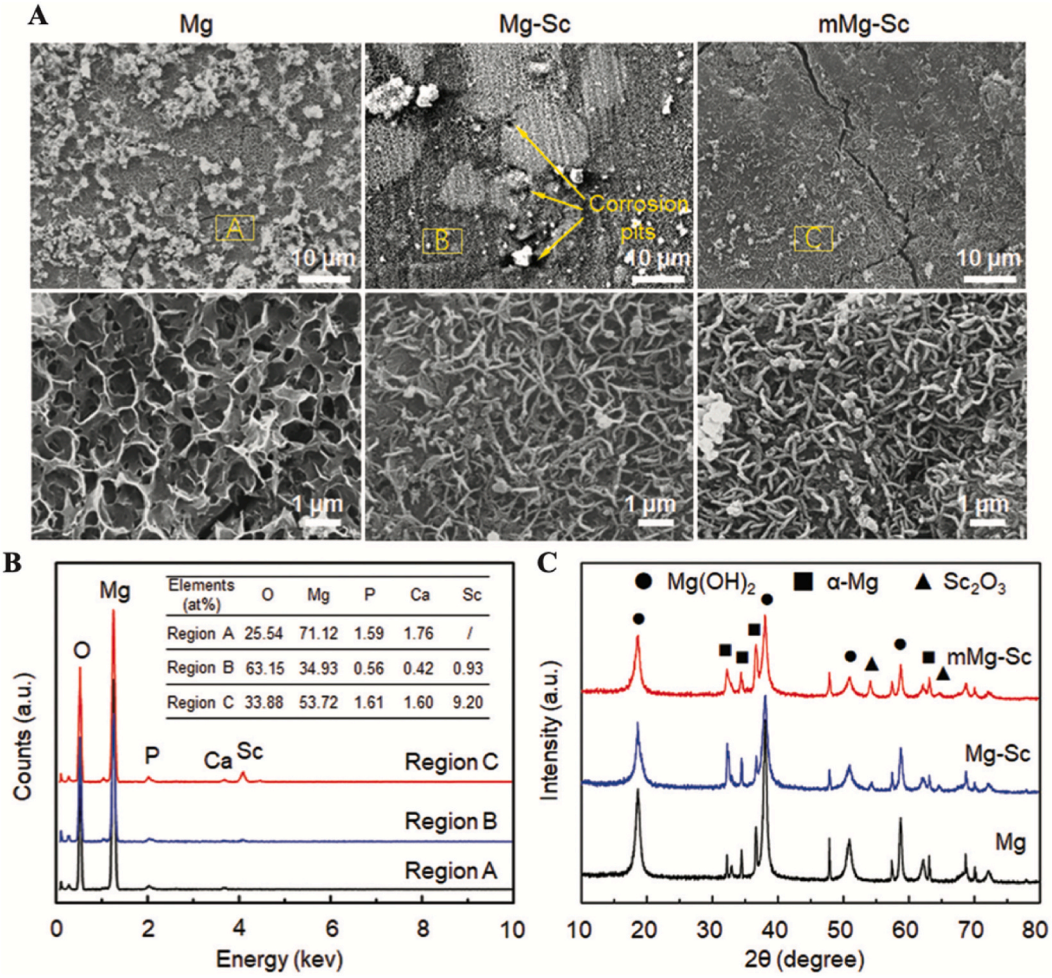


**Fig. 16.** (a) the surface morphologies after immersion in SBF, (b) the elemental analysis of the selected area, and (c) the XRD patterns of the sample's corrosion products [62].

**Table 6**
Standard hardening and temper designations for magnesium alloys n [153].

| Tempering designation | Heat treatment process |
|---|---|
| **F** | As fabricated |
| **O** | Annealed |
| **H** | Strain hardened |
| **H1** | Strain hardened only |
| **H2** | Strain hardened and partially annealed |
| **H3** | Strain hardened and then stabilized |
| **W** | Solution heat treated, unstable temper, alloy spontaneously aged at room temperature |
| **T** | Thermally treated to produce stable temper |
| **T1** | Cooled and naturally aged |
| **T3** | Solution heat treated and cold worked |
| **T4** | Solution heat treated |
| **T5** | Cooled and artificially aged only |
| **T6** | Solution heat treated and artificially aged |
| **T7** | Solution heat treated and stabilized |
| **T8** | Solution heat treated, cold worked, and artificially aged |
| **T9** | Solution heat treated, artificially aged, and cold worked |
| **T10** | Cooled, artificially aged, and cold worked |

### *5.1.3. Surface modification and coating*

Surface finishing techniques or modifications, such as polishing like laser surface remelting, are commonly employed to enhance surface quality, reduce roughness, and enhance the oxidation resistance of AM parts. For example, laser remelting, also referred to as surface remelting, is a post-processing technique commonly applied to refine parts [55] produced by additive manufacturing methods such as SLM. The process involves re-scanning the surface of a previously solidified material using a high-energy laser [176]. This laser energy is sufficient to remelt a thin top layer of the material without adding new powder. In 2024, Luo et al. [187] examined the effect of fibre laser surface remelting on the corrosion resistance of SLM-AZ31 alloy. The corrosion behaviour was evaluated by electrochemical polarisation scan, revealing that the treatment markedly reduced the crystallite size in the remelted layer to between 11.23 and 15.80 μm, thus improving its resistance to corrosion.

Wang et al. [188] also enhanced the surface of SLM-fabricated ZK60 alloy by applying a micro-arc oxidation (MAO) coating. The compound $Ca_3Mg_3(PO_4)_4$, resulting from the corrosion process, is essential for improving the material's resistance to corrosion. It creates a robust and adhesive layer on the surface that effectively obstructs the penetration of corrosive substances. This preventive measure inhibits additional degradation of the underlying coating and assists in preserving the material's structural integrity in biomedical environments. Yao et al. [179] employed a gas-atomized $Fe_{55}Cr_{25}Mo_{16}B_2C_2$ metallic glass (MG) powder to create a conformal surface coating on SLM magnesium alloys, with the explicit aim of enhancing their resistance to corrosion. Utilising microstructural characterisation and electrochemical testing, including dynamic polarisation testing and impedance-based electrochemical analysis, they demonstrated that the integration of this hybrid MG–Mg architecture resulted in a significant decrease in corrosion current density and a corresponding increase in polarisation resistance. As a result, the coated specimens demonstrated significantly enhanced

barrier qualities [189] and maintained structural integrity under simulated physiological conditions, highlighting the potential of this hybrid coating method to prolong the service life of Mg-based biomedical implants. On the other hand, Yang et al. [98] deposited a mesoporous bioglass (MBG) coating onto the surface of a ZK60 magnesium alloy using the sol-gel method. Fig. 17 deposited a mesoporous bioglass (MBG) coating onto the surface of an SLM ZK60 using the process of sol-gel. The resulting ZK60/MBG composite exhibited a significantly reduced degradation rate of 0.31 mm/year, which was notably lower than that of counterparts (Fig. 17). Following immersion, the concentrations of Ca and P ions exhibited an increase, indicative of the typical ion release behaviour of bioactive materials. This indicates the localised degradation of the hybrid ZK60 surface, in accordance with its bioactive characteristics. Table 7 summarises recent studies focused on mitigating corrosion in SLM-processed magnesium alloys for biomedical applications.

The use of a substance mimicking hydroxycarbonate apatite (HCA) on the surface of magnesium, in addition to conventional alloying with metallic elements to enhance its biological efficiency, has attracted interest. This mineral layer, resembling bone, enhances osteoconductivity and possesses intrinsic antibacterial properties, presenting a viable approach for augmenting implant integration and mitigating infection risk. In their early investigation, Yin et al. [175] assessed the degradation performance of potential implant materials by incorporating different bioactive glass composites onto the surface of an SLM ZK30 alloy. The corrosion performance of the studied specimens, determined through hydrogen evolution and electrochemical polarisation tests, diminished in the following sequence: ZK30/10BG, ZK30/5BG, ZK30/15BG, and ZK30. The in vitro cell viability results showed that ZK30/10BG and ZK30/15BG were more cytocompatible than ZK30 and ZK30/5BG. Incorporating 10 % weight of bioactive glass has demonstrated excellent corrosion resistance and beneficial formability. Similarly, Yao et al. [179] employed a metallic glass on the surface of pure magnesium to assess cytotoxicity in MG-63 cells. The samples showed low cytotoxicity and good compatibility with human cells. Also, Gao et al. [191] applied a continuous magnesium fluoride ($MgF_2$) element into the surface of the SLM-AZ61 alloy. Prior to coating, the AZ61 specimens underwent initial cleaning using absolute ethanol, followed by immersion in a stirred hydrofluoric acid (HF) solution for durations of 6, 12, 24, and 48 h, respectively. The AZ61-24$MgF_2$ exhibited a better cellular response relative to the AZ61 extract, possibly due to increased cell density, attributable to its reduced disintegration rate and more regulated ion release.

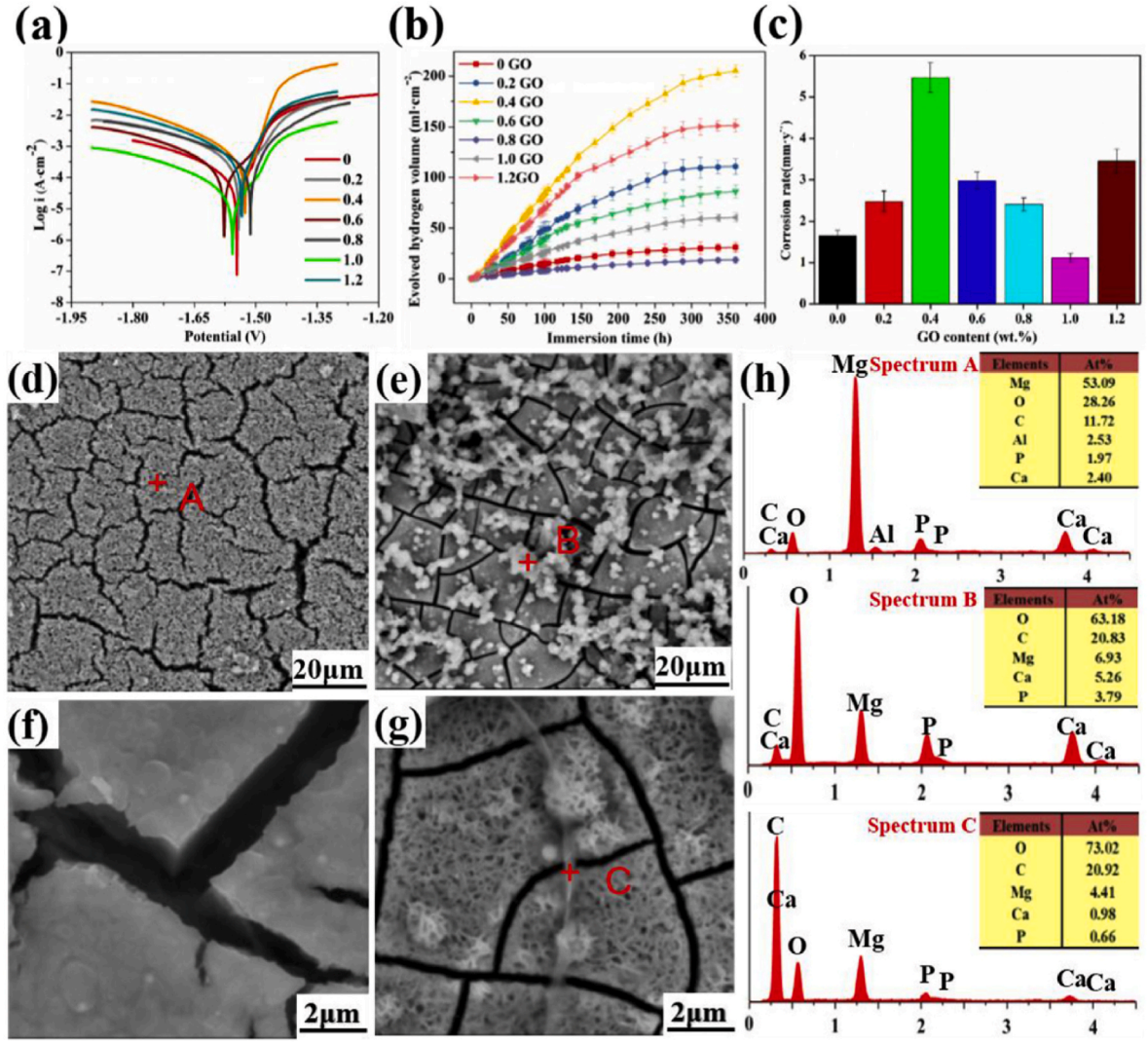


**Fig. 17.** Typical polarisation curves, hydrogen evolution, weight loss in SBF, surface morphology, and EDS analysis for corrosion analysis of SLM AZ61-xGO samples [190].

**Table 7**
Current status for mitigating corrosion in SLM-processed Mg alloys for biomedical applications.

| Material | Corrosion Mitigation | Method | Corrosion Measurement Rate | | | | Remark | Ref |
|---|---|---|---|---|---|---|---|---|
| | | | Weight loss | Potentio-dynamic | EIS | $H_2$ evolution (10 h) | | |
| | | | mm/year | x$10^{-5}$ (μA/cm$^2$) | Rct (Ω cm$^2$) | mL/cm$^2$ | | |
| WE43 | As-built | | 2.6 | | | | Treatment is needed to improve corrosion resistance. | Lovašiová et al. [145] |
| Mg–10Zn-0.8Ca-0.5Zr | As-built | | 1.4 | | | | Corrosion parameters evolve satisfactorily | Raducanu et al. [158] |
| WE43 | As-built | | 2.1 | | | | As-built samples were worse than the extruded material | Suchý et al. [130] |
| WE43 | Heat treatment | Hot isostatic pressing (HIP) and heat treatment (HT) | | 2.1–5.5 | 32–3790 | 0.8–1.8 | HIP + HT improved the corrosion rate. | Esmaily et al. [42] |
| WE43 | Heat treatment | T4 and T6 | 0.4–5.8 | | | 0.3–4.0 | T4 treatment offered excellent corrosion resistance. | Ling et al. [100] |
| AZ91 | Rolling and heat treatment | Rolling and T6 | 7.2 | | 981–1523 | 0.5–14.0 | Fine $Mg_{17}Al_{12}$ particles act as a corrosion barrier | Wang et al. [161] |
| WE43 | Heat treatment and surface modification | T6 and Plasma Electrolytic Oxidation (PEO) | | | | | PEO modification effectively reduces degradation rate. | Kopp et al. [192] |
| AZ31 | Surface modification | Laser surface remelting with power density (2100, 2250, and 2400 W) | 0.3–0.6 | 2.8–7.9 | 57–185 | | Laser surface remelting at 2250 W gave good corrosion resistance | Luo et al. [187] |
| Pure Mg | Surface modification | Layering with metallic glass | | 0.5–2.0 | | | Hybrid material greatly improved corrosion resistance. | Yao et al. [176] |
| ZK60 | Surface modification | Micro-arc oxidation (MaO) | | | 579–6732 | | $Ca_3Mg_3(PO_4)_4$ forms a protective layer that slows coating degradation. | Wang ZX et al. [188] |
| AZ61 | Alloying design | Alloying with Manganese (Mn) and Tin (Sn) | 1.1–3.5 | | | 4.0–13.0 | AZ61–0.4Mn– 0.8Sn showed highest corrosion resistance. | Gao et al. [191] |
| AZ61 | Alloying design | Alloying with Graphene Oxide (GO) | 1.2–5.6 | | | 1.0–15.0 | AZ61-1.0GO exhibited the best corrosion resistance | Shuai et al. [190] |
| Mg-xZn-0.2 Mn | Alloying design | Variations in Zn content | | 5.9–35.1 | | | Corrosion resistance decreased with increasing Zn content | Xie et al. [131] |
| Pure Mg | Alloying design | Alloying with rare earth scandium (Sc) | 0.6–2.8 | 1.3–4.6 | 238–360 | 0.5–2.0 | Scandium improved corrosion resistance. | Yang et al. [193] |

### 5.2. *In vivo*

The in vivo evaluation of SLM-Mg alloys is essential for determining their appropriateness for biomedical applications, especially as biodegradable implants. In general, these studies involve the implantation of Mg structures into living species, such as mice or rabbits, to monitor real-time degradation, biocompatibility, and mechanical performance [194]. It is crucial for understanding the relationship of the material with bone and soft tissues, the rate and consistency of Mg biodegradation, hydrogen gas production, and the systemic impacts of released Mg ions. These research investigations are essential in preclinical validation and are vital to ensuring the safe and effective translation of Mg-based devices into clinical use.

Osteoporotic fractures represent one of the most critical consequences of osteoporosis, frequently accompanied by bone voids that hinder the reestablishment of equilibrium between osteogenesis and bone resorption. Addressing this challenge, Ran et al. [195] explored the therapeutic potential of a surface-modified Mg–Nd–Zn–Zr alloy scaffold incorporating a zoledronic acid (ZA) and strontium-containing ceramic (Sc) composite coating for enhancing osteoporotic bone regeneration. Their study utilised a defect model in 60 female Sprague-Dawley rats, each three months old. Results indicated that the Mg/Sc/ZA group achieved a markedly enhanced healing response compared to both the uncoated Mg and Mg/Sc groups. Furthermore, scaffolds functionalised with the drug composite exhibited a notably slower degradation profile, contributing to superior repair quality and accelerated recovery of osteoporotic bone lesions [196]. However, an excess release of Mg ions from the alloy scaffold can create a highly alkaline local environment, potentially downregulating the expression of proteins critical for osteogenic differentiation.

Bian et al. [197] fabricated SLM-AZ91D alloy samples and implanted them into Sprague Dawley rats to evaluate unexpected bone destruction and prolonged foreign body reactions. They concluded that the rapid corrosion of SLM-AZ91D alloys led to adverse biological responses after prolonged exposure in the body. The severe corrosion of the SLM components, combined with a rise in pH and the rapid release of byproducts such as metallic ions, hydroxide structure, molecular hydrogen [198], and transient reactive elements, further complicated the biological environment. Additionally, the local microenvironment close to the metallic surface remains relatively unstable and harsh, creating conditions that are harmful to surrounding cells and tissues. The accumulation of corrosion byproducts exceeds the body's ability to eliminate them. Fig. 18 shows the corrosion routes and the corresponding biological reactions of SLM-processed magnesium alloys. Careful consideration must be given to these challenges prior to the clinical application, as adverse effects seem to be more prevalent in SLM-fabricated alloys than in their extruded equivalents.

#### 5.2.1. *Porous structures*

Furthermore, SLM facilitates the production of porous Mg alloys with precisely regulated structures, rendering them feasible alternatives for bone implant usage. The use of a porous structure replicates the natural form of cancellous bone, improving osteointegration and facilitating circulation and nutrient exchange. In in vivo investigations, these porous Mg scaffolds have demonstrated the capacity to facilitate new bone formation and gradual biodegradation. However, the increased

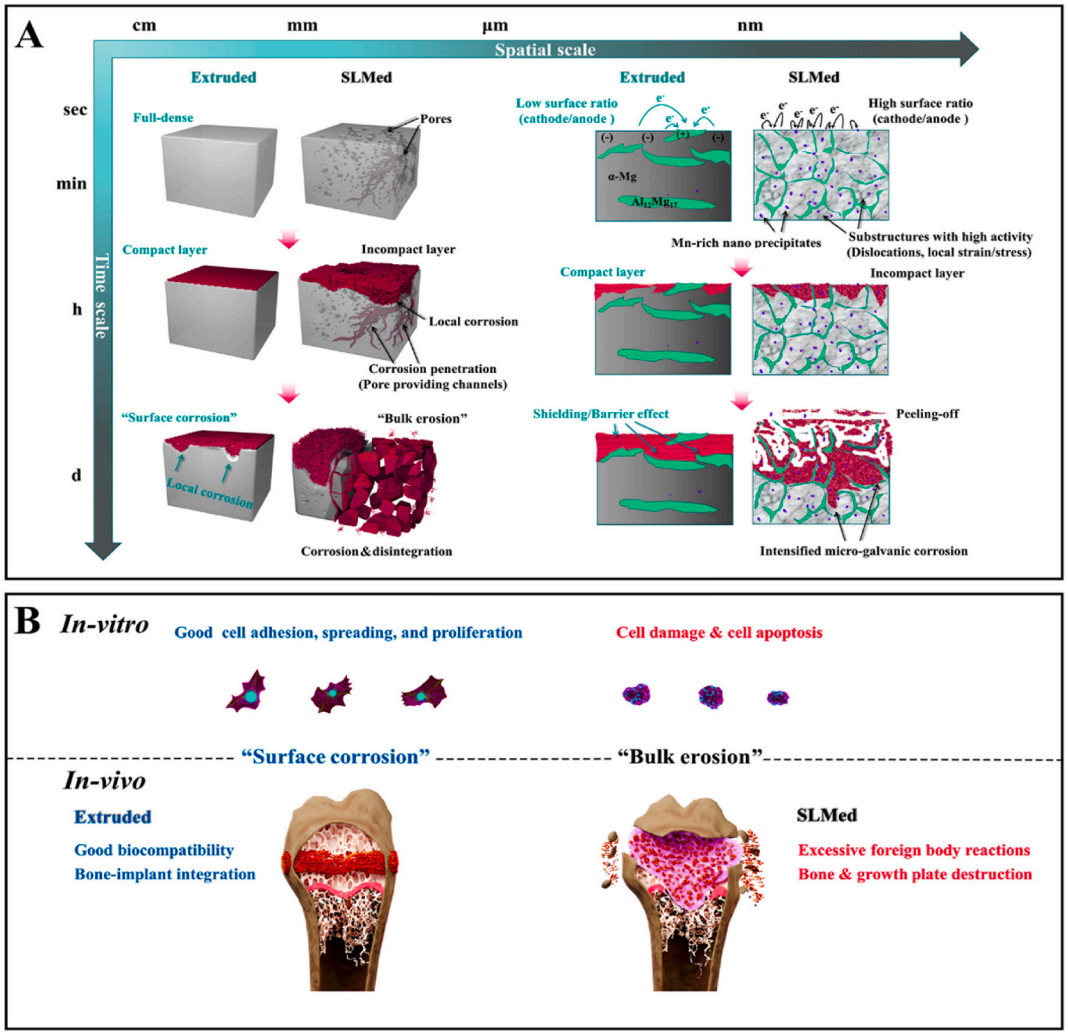


**Fig. 18.** Comparative biological responses of SLM and extruded magnesium alloys based on in-vitro and in-vivo evaluation [197].

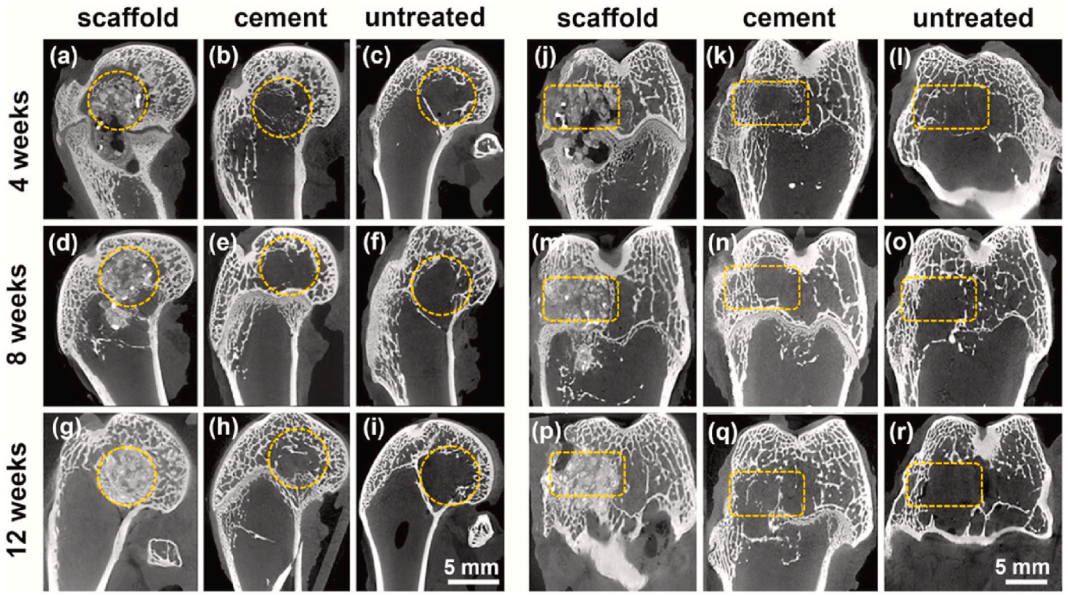


**Fig. 19.** Sagittal and coronal micro-CT images illustrate the femoral condyle defects (highlighted) at different postoperative intervals, assessed using porous SLM-Mg implants [203].

surface area associated with porosity can also accelerate corrosion rates, potentially leading to local alkalinity, gas release, and foreign body reactions. Therefore, it is necessary to balance the structural strength, deterioration rate, and biological compatibility of porous SLM-Mg implants [199].

Carefully designed pore size, interconnectivity, and alloy composition are essential to achieve optimal in vivo performance [200]. For example, in a study by Xie et al. [201] a porous Mg–Nd–Zn–Zr (JDBM) diamond lattice architecture scaffold was produced via SLM that mimics trabecular bone to facilitate complete regeneration of extensive bony defects. The 3D-printed JDBM implant was evaluated for implant-related infection in a rabbit model. The results demonstrated that the high $Mg^{2+}$ concentration generated during degradation promoted the polarisation of macrophages toward the pro-inflammatory M1 phenotype. Liu et al. (2022) determined the optimised processing parameter to obtain WE43 porous scaffolds with a relative density of 99.5 %. The results indicate that both the cavity and the WE43 scaffold were replaced by a visibly white substance after 12 weeks, signifying that new bone progressively developed within the defect area as the scaffold continued to disintegrate. The defect area was predominantly empty, with minimal bone development noted in the untreated group (Fig. 19). Wang C et al. [202] used a model of a rabbit femoral condyle lesion to see whether pore diameters affect the healing of bone. The study showed that porosity greatly helps bone tissue grow. Porous Mg is an excellent contender for usage in medicine to fix bone issues. Wang et al. [202] did very similar work that also shows that the structure of the pores is critical for both osteointegration and the formation of new bone tissue.

Fig. 20 illustrates the comparative degradation rates of various Mg alloys processed via SLM from 2020 onwards, highlighting differences relative to traditionally fabricated as-built magnesium materials. In general, numerous alloys and post-processed materials in the graph exhibit enhanced corrosion resistance. WE43/T4, AZ31 with surface re-melting, PureMg/Sc, and AZ61/GO demonstrate corrosion rates under 1 mm/year, significantly lower than untreated or as-fabricated materials. The decreases are likely due to microstructural improvement, stress relief, grain boundary engineering, or passive film stabilisation, accomplished by alloying or heat treatments [204,205]. For instance, the T4 treatment of WE43 likely dissolves secondary phases and homogenises the matrix, enhancing corrosion resistance, while scandium additions may facilitate grain refinement and passivation. As-fabricated magnesium alloys are recognised for their elevated corrosion rates, typically between 2 and 8 mm/year, attributed to residual stresses, significant surface roughness, porosity, and heterogeneous microstructures. Notably, AZ91/rolled + annealed exhibits the poorest performance, suggesting that specific thermomechanical treatments may inadequately enhance corrosion resistance and could potentially worsen it [206]. This comparative investigation emphasises the significance of alloy design and post-processing in reducing the naturally elevated corrosion rates of as-fabricated Mg alloys [183]. The materials within the lower corrosion regime are promising prospects for sustainable implant technologies.

Fig. 21 illustrates the in vivo corrosion rates of Mg alloys and modifications fabricated via SLM as a function of implantation time in various animal models reported since 2020. As can be seen, the LX41 alloy, evaluated in a rat tibial model, exhibits the slowest degradation rate, presumably because of its rare-earth makeup [108] and the comparatively stable mechanical environment of the tibia. Conversely, Mg-8.5Li exhibits the acceptable value, indicative of the synergistic effects of lithium's high reactivity and the dynamic, chloride-laden vascular environment [207]. The graph does not clearly depict the WE43/PEO-coated sample; nonetheless, its reference implies that surface changes, such as plasma electrolytic oxidation (PEO), may further influence degradation rates in subsequent animal experiments. The as-fabricated WE43 alloy, implanted in a rabbit femur, demonstrates the worst corrosion rate. This in vivo study underlines the significant effect of alloy substance, fabrication technique, and implantation locations on the degradation of Mg alloys. The results indicate that WE43 alloys manufactured via SLM may necessitate post-processing treatments or protective coatings to achieve corrosion resistance comparable [208] to that of conventionally processed counterparts. A surprising discovery from this in vivo investigation is that the corrosion rates of SLM Mg alloys in biological conditions are lower than those recorded in in vitro tests. The difference is due to proteins, phosphates, and carbonates in physiological fluids accumulating on the Mg surface, creating a semi-protective coating that inhibits its further decomposition [197].

## 6. Future direction

Conventional Mg alloys, originally designed for casting or extrusion, exhibit poor processability and unpredictable degradation when exposed to the extreme solidification conditions of SLM. Incorporating high-entropy alloy (HEA) principles into magnesium systems, such as Mg–Zn–Y-Nd-Ca [212], to mitigate solidification cracking and improve corrosion control through microstructural complexity is very worthwhile for investigation. This method involves an alloy composed of five

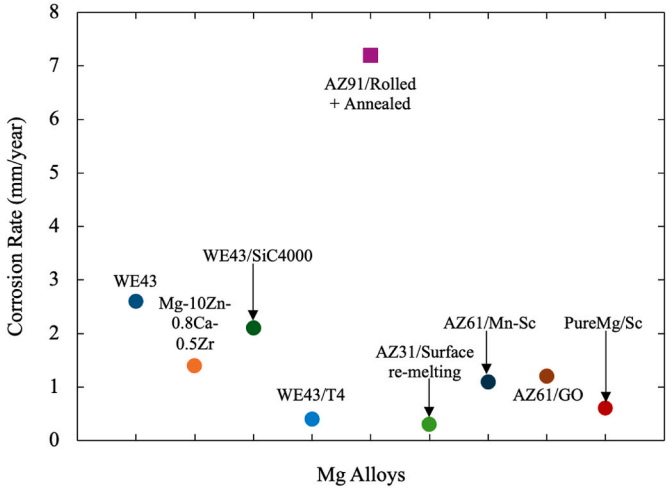


**Fig. 20.** Corrosion rates of Mg alloys fabricated via SLM (SLM) and tested in SBF and Hank's solution since 2020 [100,130,145,158,161,187,190,191,193].

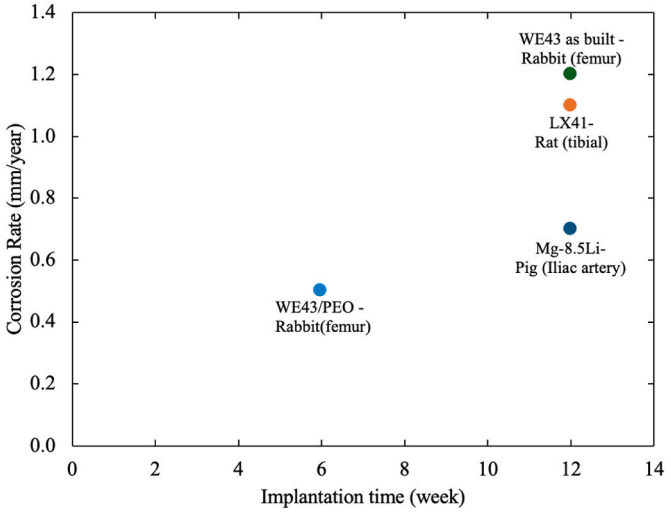


**Fig. 21.** In vivo corrosion rates of Mg alloys and modifications fabricated via SLM as a function of implantation time in various animal models reported since 2020 [203,209–211].

or more main elements mixed in almost equal atomic amounts, which leads to a high configurational entropy. This high entropy promotes the formation of straightforward solid solution structures rather than complex intermetallic compounds [213]. Developing advanced alloys such as magnesium-based high-entropy alloys for SLM is a complex, costly, and multi-faceted challenge. Applying Bayesian optimisation and reinforcement learning to improve the printability, biodegradability, and mechanical characteristics of SLM-Mg alloys for biomedical applications offers an important and emerging skill set [214,215].

The SLM of Mg alloy is limited by a restricted processing window due to its low boiling point, elevated vapour pressure, and propensity for oxidation [216]. Mahmood et al. [217] proposed the development of integrated thermal-fluid-mechanical-microstructure models that compensate for Marangoni convection, recoil pressure, keyhole dynamics, and oxide film evolution through the application of Gaussian processes and deep neural networks in simulations, thus minimising the need for extensive experimental and parameter data trials. Besides, the integration of multi-objective optimisation using Pareto front analysis to concurrently minimise porosity, maximise density, and regulate grain shape of Mg alloy is appealing to look into [218].

Biodegradable performance of SLM Mg alloys is governed by the coupled interaction of microstructure, local electrochemistry, and mechanical loading [2,77,85]. To enhance prediction capacities, phase-field models of localised corrosion and pitting can be developed by deriving input parameters from microstructural characteristics based on Electron Backscatter Diffraction (EBSD) and Atom Probe Tomography (APT) [219]. Conversely, the establishment of digital twins for magnesium implants, integrating patient-specific loading conditions and fluid flow dynamics, offers an exciting chance to replicate long-term deterioration kinetics and assess mechanical stability [209].

In addition, untreated SLM-Mg surfaces demonstrate irregular corrosion and insufficient cellular adhesion owing to surface oxide variability and micro-porosity. The technique to combat this issue is by applying atomically engineered coatings like functionalised self-assembled monolayers [220] and multi-layered nanocomposites [221] in SLM-Mg alloy that serve as tuneable corrosion barriers and drug delivery systems. The combination of advanced surface patterning techniques, including laser-induced periodic surface structures (LIPSS) and two-photon lithography, is a promising strategy to improve osteointegration and endothelialization [222]. Also, a further interesting option is the development of intelligent surface coatings that include stimuli-responsive polymers or bioresorbable inorganic layers, designed to degrade in a controlled manner that corresponds with the degradation profile of the Mg implant [223,224].

The release of Mg ions and the decomposition byproducts considerably affects immune cell polarisation and inflammatory responses, although these effects are little established. To further investigate the host response, single-cell RNA sequencing (scRNA-seq) combined with proteome profiling can be utilised to elucidate immunological processes, such as macrophage M1/M2 polarisation and cytokine signalling networks, related to SLM-fabricated magnesium implants [225,226]. Further, engineering alloy compositions or surface treatments to regulate the immune response may be proposed as an approach to enhance healing and reduce fibrotic encapsulation [227]. The organ-on-chip platforms used by Mansoorifar et al. [228], which replicate vascular and osseous microenvironments under physiomimetic conditions, offer a valuable tool for preclinical assessment and could be effectively applied to investigate the biological performance of SLM-Mg alloys.

In orthopaedic and load-bearing biomedical implants, porous structures are intentionally introduced to achieve both mechanical compatibility and biological integration with host tissue. Porous features are purposefully included in orthopaedic and load-bearing biomedical implants to promote mechanical and biological interactions with the host tissue. For lowering the stress shielding effect [229–231]. it is essential to create the structure with controlled porosity. It can only easily be done with tools like SLM. Functionally graded porous structures with customised stiffness levels are a promising way to reduce stress shielding because they closely resemble the mechanical properties of natural bone. It is necessary to achieve an optimal equilibrium between mechanical strength and sufficient porosity to facilitate tissue integration [232,233]. In addition, using a generative design and shape optimisation might be employed to create load-bearing SLM-Mg implants that employ less material and enhance biocompatibility [234]. Also, integration of porous structures with voxel-based modelling and patient-specific CT/MRI data facilitates the creation of biomimetic designs, such as trabecular meshes, that emulate the appearance and movement of authentic bones [235,236].

## 7. Conclusions

SLM of Mg alloys presents a promising pathway for fabricating biodegradable implants with complex geometries and tailored properties. The success of SLM depends heavily on processing parameters such as laser power, scan speed, and layer thickness, which significantly influence microstructure, grain size, and texture. Optimising these parameters is essential, as grain refinement typically improves mechanical strength and corrosion resistance. Common Mg alloys studied in SLM research include WE43, AZ31, and ZK60, selected for their favourable mechanical properties and biocompatibility. Despite these advantages, rapid corrosion remains a challenge, potentially compromising structural integrity before complete tissue regeneration. As such, both in vitro and in vivo studies are vital to evaluate degradation behaviour, cytocompatibility, and host response. Porous structures enabled by SLM not only reduce stress shielding but also promote osteointegration and vascularization by mimicking trabecular bone. Future research should aim to refine grain control strategies, apply surface modifications or bioactive coatings, and leverage voxel-based modelling combined with CT/MRI data for patient-specific design. Integrating these approaches will enhance the predictability and performance of Mg-based implants, supporting their translation into clinical practice.

## Declaration of competing interest

The authors declare that they have no known competing financial interests or personal relationships that could have appeared to influence the work reported in this paper.

## Acknowledgements

The authors express their gratitude for the funding received from **the** Horizon Europe Programme **(HORIZON-MSCA-2022-SE-01–01)** under Grant Agreement number **101129996.** We extend our sincere appreciation to the Silesian University of Technology**, Gliwice, Poland,** for facilitating valuable secondment opportunities, scientific collaboration, and knowledge exchange. They also express their gratitude to Universiti Teknologi Malaysia **(UTM)** for the research grant **PY/2024/02153**, with cost centre No. **R.K130000.7309.1U081**, and for sabbatical leave, which made it possible to finish this study.

## References

[1] Aufa AN, et al. Current trends in additive manufacturing of selective laser melting for biomedical implant applications. J Mater Res Technol 2024;31:213–43. https://doi.org/10.1016/j.jmrt.2024.06.041. 2024/07/01/.
[2] Kurzynowski T, Pawlak A, Smolina I. The potential of SLM technology for processing magnesium alloys in aerospace industry. Arch Civ Mech Eng 2020;20(1):23.
[3] Aufa A, et al. Current trends in additive manufacturing of selective laser melting for biomedical implant applications. J Mater Res Technol 2024.
[4] Joshua RJN, et al. Powder bed fusion 3D printing in precision manufacturing for biomedical applications: a comprehensive review. Materials 2024;17(3):769.
[5] Vayssette B, Saintier N, Brugger C, El May M. Surface roughness effect of SLM and EBM Ti-6Al-4V on multiaxial high cycle fatigue. Theor Appl Fract Mech 2020;108:102581. https://doi.org/10.1016/j.tafmec.2020.102581.

[6] Sui S, et al. Additive manufacturing of magnesium and its alloys: Process-Formability-Microstructure-performance relationship and underlying mechanism. Int J Extrem Manuf 2023;5(4):042009.
[7] Gatto ML, et al. Improved biomechanical behavior of 316L graded scaffolds for bone tissue regeneration produced by laser powder bed fusion. journal of the mechanical behavior of biomedical materials 2023;144:105989.
[8] Mazumder S, Boban J, Ahmed A. A comprehensive review of recent advancements in 3D-Printed co-cr-based alloys and their applications. Journal of Manufacturing and Materials Processing 2025;9(5):169.
[9] Meng M, Wang J, Huang H, Liu X, Zhang J, Li Z. 3D printing metal implants in orthopedic surgery: methods, applications and future prospects. Journal of Orthopaedic Translation 2023;42:94–112.
[10] Aufa AN, Hassan MZ, Ismail Z, Harun N, Ren J, Sadali MF. Surface enhancement of Ti-6Al-4V fabricated by selective laser melting on bone-like apatite Formation. J Mater Res Technol 2022/06/30/2022. https://doi.org/10.1016/j.jmrt.2022.06.135.
[11] Cabrini M, et al. Influence of surface finishing and heat treatments on the corrosion resistance of LPBF-produced Ti-6Al-4V alloy for biomedical applications. J Mater Process Technol 2022;308:117730.
[12] Aufa AN, Hassan MZ, Ismail Z, Ren J. Sol–gel surface modification of selective laser melting Ti6Al4V for biomedical applications. Progress in Additive Manufacturing 2024. https://doi.org/10.1007/s40964-024-00748-0.
[13] Yusufu Y, et al. Magnesium alloy implant GZ31K with enhanced corrosion resistance promotes fracture healing in vitro and in vivo systems. J Magnesium Alloys 2025.
[14] Aufa AN, Hassan MZ, Ismail Z. Recent progress of sol-gel coating of pure magnesium in biomedical applications. A review. Malaysian Journal of Medicine and Health Sciences 2021;17.
[15] Fatima G, et al. Magnesium matters: a comprehensive review of its vital role in health and diseases. Cureus 2024;16(10).
[16] Fiorentini D, Cappadone C, Farruggia G, Prata C. Magnesium: biochemistry, nutrition, detection, and social impact of diseases linked to its deficiency. Nutrients 2021;13(4):1136.
[17] Zhang Q-H, Cossey A, Tong J. Stress shielding in periprosthetic bone following a total knee replacement: effects of implant material, design and alignment. Med Eng Phys 2016;38(12):1481–8.
[18] Li C, et al. Design of biodegradable, implantable devices towards clinical translation. Nat Rev Mater 2020;5(1):61–81.
[19] Atrens A, Chen X, Shi Z. Mg corrosion—recent progress. Corros Mater Degrad 2022;3(4):566–97.
[20] Xu T, Yang Y, Peng X, Song J, Pan F. Overview of advancement and development trend on magnesium alloy. J Magnesium Alloys 2019;7(3):536–44.
[21] Zeng Z, Salehi M, Kopp A, Xu S, Esmaily M, Birbilis N. Recent progress and perspectives in additive manufacturing of magnesium alloys. J Magnesium Alloys 2022;10(6):1511–41.
[22] Aufa AN, Hassan MZ, Ismail Z. Recent advances in Ti-6Al-4V additively manufactured by selective laser melting for biomedical implants: prospect development. J Alloys Compd 2021;896. https://doi.org/10.1016/j.jallcom.2021.163072.
[23] Sharma SK, et al. Significance of alloying elements on the mechanical characteristics of Mg-based materials for biomedical applications. Crystals 2022;12(8):1138.
[24] Reza Kashyzadeh K, Amiri N, Maleki E, Unal O. A critical review on improving the fatigue life and corrosion properties of magnesium alloys via the technique of adding different elements. J Mar Sci Eng 2023;11(3):527.
[25] Rahmatabadi D, Ahmadi M, Pahlavani M, Hashemi R. DIC-based experimental study of fracture toughness through R-curve tests in a multi-layered Al-Mg (LZ91) composite fabricated by ARB. J Alloys Compd 2021;883:160843.
[26] Zhou K, et al. A view of magnesium alloy modification and its application in orthopedic implants. J Mater Res Technol 2025;36:1536–61. https://doi.org/10.1016/j.jmrt.2025.03.188. 2025/05/01/.
[27] Shi H, Xu C, Hu X, Gan W, Wu K, Wang X. Improving the Young's modulus of Mg via alloying and compositing–a short review. J Magnesium Alloys 2022;10(8):2009–24.
[28] Tian G, Wang J, Wang S, Xue C, Yang X, Su H. An ultra-light Mg-Li alloy with exceptional elastic modulus, high strength, and corrosion-resistance. Mater Today Commun 2023;35:105623.
[29] Helmer AT, Mugale MV, Borkar T, Gupta RK. A magnesium alloy with high corrosion resistance, hardness and elastic modulus enabled by elemental synergy. Mater Lett 2025/11/15/2025;399:139102. https://doi.org/10.1016/j.matlet.2025.139102.
[30] Qian L, et al. Biodegradable PTMC-MAO composite coatings on AZ31 Mg-alloys for enhanced corrosion-resistance. J Alloys Compd 2024;998:175017.
[31] Bakhori SNM, Bakhori NM, Hassan MZ, Suyambulingam I, Sundaram RS, Mahardika M. Compression after impact (CAI) behavior after low-velocity impact (LVI) of agro-waste-based pineapple leaf fiber (PALF) and kevlar fabrics-reinforced polyester composites for automotive applications. Polym Compos 2025.
[32] Seetharaman S, Sankaranarayanan D, Gupta M. Magnesium-based temporary implants: potential, current status, applications, and challenges. J Funct Biomater Jun 17 2023;14(6). https://doi.org/10.3390/jfb14060324 (in eng).
[33] Saha S, Roy S. Metallic dental implants wear mechanisms, materials, and manufacturing processes: a literature review. Materials 2022;16(1):161.
[34] Ramya M. Advances in biodegradable orthopaedic implants: optimizing magnesium alloy corrosion resistance for enhanced bone repair. Biomedical Materials & Devices 2025;3(1):396–414.
[35] Bakhori NM, Daud MYM, Hassan MZ, Suyambulingam I. Characterisation of pineapple leaf fibre/poly (methacrylic acid) semi-interpenetrating network hydrogel. Results Eng 2025:105184.
[36] Limbasiya N, Jain A, Soni H, Wankhede V, Krolczyk G, Sahlot P. A comprehensive review on the effect of process parameters and post-process treatments on microstructure and mechanical properties of selective laser melting of AlSi10Mg. J Mater Res Technol 2022;21:1141–76.
[37] Aufa AN, Hassan MZ, Ismail Z. Recent advances in Ti-6Al-4V additively manufactured by selective laser melting for biomedical implants: prospect development. J Alloys Compd 2022/03/10/2022;896:163072. https://doi.org/10.1016/j.jallcom.2021.163072.
[38] Tan Z, et al. Fabrication of Zr-based bulk metallic glass lattice structure with high specific strength by laser powder bed fusion. Addit Manuf 2024;95:104556.
[39] Singla AK, et al. Selective laser melting of Ti6Al4V alloy: process parameters, defects and post-treatments. J Manuf Process 2021;64:161–87.
[40] Praneeth J, Venkatesh S, Krishna LS. Process parameters influence on mechanical properties of AlSi10Mg by SLM. Mater Today Proc 2023.
[41] Ibrahim MI, et al. Central composite design for optimization of kenaf-reinforced epoxy composite bonding performance. Bioresources 2024;19(1):605.
[42] Esmaily M, et al. A detailed microstructural and corrosion analysis of magnesium alloy WE43 manufactured by selective laser melting. Addit Manuf 2020;35:101321.
[43] Zhang C, Li Z, Zhang J, Tang H, Wang H. Additive manufacturing of magnesium matrix composites: comprehensive review of recent progress and research perspectives. J Magnesium Alloys 2023;11(2):425–61.
[44] Chen J, Chen B. Progress in additive manufacturing of magnesium alloys: a review. Materials 2024;17(15):3851.
[45] Wu C, Zai W, Man HC. Additive manufacturing of ZK60 magnesium alloy by selective laser melting: parameter optimization, microstructure and biodegradability. Mater Today Commun 2021;26:101922.
[46] Shi G, Zhang R, Cao Y, Yang G. A review of the vaporization behavior of some metal elements in the LPBF process. Micromachines 2024;15(7):846.
[47] Wang J, Zhu R, Liu Y, Zhang L. Understanding melt pool characteristics in laser powder bed fusion: an overview of single-and multi-track melt pools for process optimization. Advanced Powder Materials 2023;2(4):100137.
[48] Tong M, et al. Influence of laser power and scanning speed on microstructure evolutions and mechanical properties of the SLM fabricated al–mg–mn–sc–zr alloy. J Mater Res Technol 2024;33:5018–29.
[49] Ahmadi M, Tabary SB, Rahmatabadi D, Ebrahimi MS, Abrinia K, Hashemi R. Review of selective laser melting of magnesium alloys: advantages, microstructure and mechanical characterizations, defects, challenges, and applications. J Mater Res Technol 2022;19:1537–62.
[50] Liu H, et al. The effects of 3D printing parameters, structural design and post-processing on the mechanical properties and corrosion resistance of SLMed ZK60 porous scaffolds. Mater Today Commun 2024;39:109123.
[51] Li K, Ji C, Bai S, Jiang B, Pan F. Selective laser melting of magnesium alloys: necessity, formability, performance, optimization and applications. J Mater Sci Technol 2023;154:65–93.
[52] Wang YM, et al. Additively manufactured hierarchical stainless steels with high strength and ductility. Nat Mater 2018;17(1):63–71.
[53] Wang X, Chen C, Zhang M. Effect of laser power on formability, microstructure and mechanical properties of selective laser melted mg-al-zn alloy. Rapid Prototyp J 2020;26(5):841–54.
[54] Xie W, Man H-C, Chan C-W. Interplay of laser power and pore characteristics in selective laser melting of ZK60 magnesium alloys: a study based on in-situ monitoring and image analysis. J Magnesium Alloys 2024;12(4):1346–66.
[55] Sharma SK, et al. Advancements in the additive manufacturing of magnesium and aluminum alloys through laser-based approach. Materials 2022;15(22):8122.
[56] Yin B, et al. Influence of layer thickness on formation quality, microstructure, mechanical properties, and corrosion resistance of WE43 magnesium alloy fabricated by laser powder bed fusion. J Magnesium Alloys 2024;12(4):1367–85.
[57] Manakari V, Parande G, Gupta M. Selective laser melting of magnesium and magnesium alloy powders: a review. Metals 2016;7(1):2.
[58] Liu S, et al. Influence of laser process parameters on the densification, microstructure, and mechanical properties of a selective laser melted AZ61 magnesium alloy. J Alloys Compd 2019;808:151160.
[59] AlMangour B, Cheng J, Grzesiak D, Hwang Y-J, Lee K-A. Fundamental study on the development of pure magnesium parts by additive manufacturing: an experimental and computational analysis. Met Mater Int 2023;29(2):429–43.
[60] Soderlind J, et al. Melt-pool dynamics and microstructure of mg alloy we43 under laser powder bed fusion additive manufacturing conditions. Crystals 2022;12(10):1437.
[61] Jia H, Sun H, Wang H, Wu Y, Wang H. Scanning strategy in selective laser melting (SLM): a review. Int J Adv Des Manuf Technol 2021;113(9):2413–35.
[62] Yang R, et al. Enhanced strength and hardness of AS41 magnesium alloy fabricated by selective laser melting. Materials 2022;15(17):5863.
[63] Deng Q, et al. Fabrication of high-strength mg-gd-zn-zr alloy via selective laser melting. Mater Char 2020;165:110377.
[64] Wang T-S, et al. Macro-/micro-structures and mechanical properties of magnesium alloys based on additive manufacturing: a review. J Mater Sci 2024;59(22):9908–40.
[65] Kaushik V, Kumar N, Vignesh M. Magnesium role in additive manufacturing of biomedical implants–challenges and opportunities. Addit Manuf 2022;55:102802.

[66] Wei K, Gao M, Wang Z, Zeng X. Effect of energy input on formability, microstructure and mechanical properties of selective laser melted AZ91D magnesium alloy. Materials Science and Engineering: A 2014;611:212–22.
[67] Wang W, Yang X, Wang KK. Research on formability, microstructure and mechanical properties of selective laser melted Mg-Y-Sm-Zn-Zr magnesium alloy. Mater Char 2022;189:111980.
[68] Shi Y, Guo K, Shi H, Huang X, Yang B, Sun J. Effects of process parameters on microstructure properties of WE43 magnesium alloy by selective laser melting. Mater Today Commun 2024;39:109151.
[69] Jiang P, Dong H, Cai Y, Gao M. Effects of laser power modulation on keyhole behavior and energy absorptivity for laser welding of magnesium alloy AZ31. Int J Adv Des Manuf Technol 2023;125(1):563–76.
[70] Wu X, et al. Laser powder bed fusion of biodegradable magnesium alloys: process, microstructure and properties. Int J Extrem Manuf 2024;7(2):022007.
[71] Liu J, Yin B, Sun Z, Wen P, Zheng Y, Tian Y. Hot cracking in ZK60 magnesium alloy produced by laser powder bed fusion process. Mater Lett 2021;301:130283.
[72] Manjhi SK, Sekar P, Bontha S, Balan A. Additive manufacturing of magnesium alloys: characterization and post-processing. Int J Lightweight Mater Manuf 2024;7(1):184–213.
[73] Ahmadi N, Naffakh-Moosavy H, Hadavi SMM, Bagheri F. The effect of Nd: YAG laser parameters on the microstructure, hot cracking susceptibility and elemental evaporation of surface melted AZ80 magnesium-based alloy. J Mater Res Technol 2023;27:2459–74.
[74] Reijonen J, Revuelta A, Metsä-Kortelainen S, Salminen A. Effect of hard and soft re-coater blade on porosity and processability of thin walls and overhangs in laser powder bed fusion additive manufacturing. Int J Adv Des Manuf Technol 2024;130(5):2283–96.
[75] Pesode P, Barve S, Wankhede SV, Mugale M. Manufacturing methods of Mg alloys for biomedical applications. In: Magnesium alloys for biomedical applications. CRC Press; 2024. p. 20–61.
[76] Soni N, Renna G, Leo P. Advancements in metal processing additive technologies: selective laser melting (SLM). Metals 2024;14(9):1081.
[77] Liu S, Guo H. A review of SLMed magnesium alloys: processing, properties, alloying elements and postprocessing. Metals 2020;10(8):1073.
[78] Zöller C, Adams N, Adami S. Numerical investigation of balling defects in laser-based powder bed fusion of metals with Inconel 718. Addit Manuf 2023;73:103658.
[79] Song X, Wang W, Han F, Liu Y. Numerical simulation of single-pass selective laser melting of Mg-Y-Sm-Zn-Zr alloy. Mater Today Commun 2024;40:109930.
[80] Wang Y, et al. Cross-Scale simulation of macro/microstructure evolution during selective laser melting of mg–gd–y alloy. Metall Mater Trans B 2024;55(4):2407–25.
[81] Chen X, et al. Research progress of heterogeneous structure magnesium alloys: a review. J Magnesium Alloys 2024.
[82] Pimenov DY, et al. Influence of selective laser melting process parameters on the surface integrity of difficult-to-cut alloys: comprehensive review and future prospects. Int J Adv Des Manuf Technol 2023;127(3):1071–102.
[83] Mo B, Li T, Deng L, Shi F, Liu W, Zhang H. Mechanisms and influencing factors of defect formations during laser-based directed energy deposition with coaxial powder feeding: a review. Virtual Phys Prototyp 2024;19(1):e2404155.
[84] Oliveira JP, LaLonde A, Ma J. Processing parameters in laser powder bed fusion metal additive manufacturing. Mater Des 2020;193:108762.
[85] Liu S, Guo H. Balling behavior of selective laser melting (SLM) magnesium alloy. Materials 2020;13(16):3632.
[86] Zhao D, Wang W, Wang K, Xu R, Li H, Dong G. Effect of process parameters on the densification of SLM-Produced mg–y–sm–zn–zr alloy. Mater Sci Technol 2024;40(11):809–20.
[87] Vela B, Mehalic S, Sheikh S, Elwany A, Karaman I, Arróyave R. Evaluating the intrinsic resistance to balling of alloys: a high-throughput physics-informed and data-enabled approach. Additive Manufacturing Letters 2022;3:100085.
[88] Li X, Liu Y, Tan C, Zou Y. Porosity formation mechanisms, microstructure evolution and mechanical performance of AlMgScZr alloy fabricated by laser powder bed fusion: effect of hatch distance. J Manuf Process 2023;94:107–19.
[89] Wang Q, Mao Y, Zhu K. Melt pool size prediction of laser powder bed fusion by process and image feature fusion. IEEE Trans Instrum Meas 2023;73:1–12.
[90] Motallebi R, Savaedi Z, Mirzadeh H. Post-processing heat treatment of lightweight magnesium alloys fabricated by additive manufacturing: a review. J Mater Res Technol 2022;20:1873–92.
[91] Shen H, Yan J, Niu X. Thermo-fluid-dynamic modeling of the melt pool during selective laser melting for AZ91D magnesium alloy. Materials 2020;13(18):4157.
[92] Hu D, et al. Experimental investigation on selective laser melting of bulk net-shape pure magnesium. Mater Manuf Process 2015;30(11):1298–304.
[93] Ali MH, Sabyrov N, Shehab E. Powder bed fusion–laser melting (PBF–LM) process: latest review of materials, process parameter optimization, application, and up-to-date innovative technologies. Progress in Additive Manufacturing 2022;7(6):1395–422.
[94] Chang C, et al. From macro-, through meso-to micro-scale: densification behavior, deformation response and microstructural evolution of selective laser melted Mg-RE alloy. J Magnesium Alloys 2025.
[95] Wang W, Liu W, Yang X, Xu R, Dai Q. Multi-scale simulation of columnar-to-equiaxed transition during laser selective melting of rare earth magnesium alloy. J Mater Sci Technol 2022;119:11–24.
[96] Wang W, Liu W, Yang X, Xu R, Dai Q. Multi-scale simulation of the dendrite growth during selective laser melting of rare earth magnesium alloy. Model Simulat Mater Sci Eng 2021;30(1):015005.
[97] Sun X, et al. Wire-based friction stir additive manufacturing of AZ31B magnesium alloy: precipitate behavior and mechanical properties. J Magnesium Alloys 2025.
[98] Yang Y, Lu C, Shen L, Zhao Z, Peng S, Shuai C. In-situ deposition of apatite layer to protect Mg-based composite fabricated via laser additive manufacturing. J Magnesium Alloys 2023;11(2):629–40.
[99] Salehi M, Seet HL, Gupta M, Farnoush H, Maleksaeedi S, Nai MLS. Rapid densification of additive manufactured magnesium alloys via microwave sintering. Addit Manuf 2021;37:101655.
[100] Ling C, et al. Influence of heat treatment on microstructure, mechanical and corrosion behavior of WE43 alloy fabricated by laser-beam powder bed fusion. Int J Extrem Manuf 2023;6(1):015001.
[101] Zhou Y, Zhang K, Liang Y, Cheng J, Dai Y. Selective laser melted magnesium alloys: fabrication, microstructure and property. Materials 2022;15(20):7049.
[102] Liang J, et al. Formability, microstructure, and thermal crack characteristics of selective laser melting of ZK60 magnesium alloy. Materials Science and Engineering: A 2022;839:142858.
[103] Ning J, Ma Z-X, Zhang L-J, Wang D-P, Na S-J. Effects of magnesium on microstructure, properties and degradation behaviors of zinc-based alloys prepared by selective laser melting. Mater Res Express 2022;9(8):086511.
[104] ZainElabdeen IH, Ismail L, Mohamed OF, Khan KA, Schiffer A. Recent advancements in hybrid additive manufacturing of similar and dissimilar metals via laser powder bed fusion. Materials Science and Engineering: A 2024;909:146833.
[105] Wei L, Li J, Zhang Y, Lai H. Effects of Zn content on microstructure, mechanical and degradation behaviors of Mg-xZn-0.2 Ca-0.1 Mn alloys. Mater Chem Phys 2020;241:122441.
[106] Qian X, et al. Influence of alloying element segregation at grain boundary on the microstructure and mechanical properties of Mg-Zn alloy. Mater Des 2022;224:111322.
[107] Sorkhi L, Madden NJ, Crawford GA. Effect of post-processing on the microstructure of WE43 magnesium alloy fabricated by laser powder directed energy deposition. Journal of Manufacturing and Materials Processing 2024;9(1):3.
[108] Liu S, Huang P, Zhou Y, Zhang S, Wang Y. A review of the different fabrication techniques of porous Mg structures considering the effect of manufacturing parameters on corrosion rate and mechanical properties in the bio application. J Mater Sci 2023;58(15):6556–79.
[109] Tan CY, Wen C, Mayes E, Zhang D, Ang HQ. Revealing the limits of laser energy density: a study of the combined effects of process parameters on melt pool and microstructure in WE43 magnesium alloys. J Magnesium Alloys 2025;13(3):1034–49.
[110] Yin Q, Yang Z, Li H, Du H. Mechanism of keyhole evolution and welding quality of electron beam welded magnesium alloy with scanning path variation via modeling and numerical study. J Magnesium Alloys 2024.
[111] Çam G, Günen A. Challenges and opportunities in the production of magnesium parts by directed energy deposition processes. J Magnesium Alloys 2024;12(5):1663–86.
[112] Niu X, Shen H, Fu J, Feng J. Effective control of microstructure evolution in AZ91D magnesium alloy by SiC nanoparticles in laser powder-bed fusion. Mater Des 2021;206:109787.
[113] Li X, Fang X, Wang S, Wang S, Zha M, Huang K. Selective laser melted AZ91D magnesium alloy with superior balance of strength and ductility. J Magnesium Alloys 2023;11(12):4644–58.
[114] Seidgazov R, Mirzade FK. Keyhole-induced porosity in laser manufacturing processes: formation mechanism and dependence on scan speed. Chin J Mech Eng: Additive Manufacturing Frontiers 2022;1(3):100044.
[115] Wang W, Wang D, He L, Liu W, Yang X. Thermal behavior and densification during selective laser melting of Mg-Y-Sm-Zn-Zr alloy: simulation and experiments. Mater Res Express 2020;7(11):116519.
[116] A. Aufa, M. Z. Hassan, and R. Ilyas, Handbook of 3D printing in biomedical applications.
[117] Wang Y, et al. Mechanisms of processing map difference between laser powder bed fusion of Mg solid cubes and lattice structures. Addit Manuf 2023;76:103773.
[118] Qiu C, Panwisawas C, Ward M, Basoalto HC, Brooks JW, Attallah MM. On the role of melt flow into the surface structure and porosity development during selective laser melting. Acta Mater 2015;96:72–9.
[119] Xu R, Wang W, Wang K, Dai Q. Finite element simulation of residual stress distribution during selective laser melting of Mg-Y-Sm-Zn-Zr alloy. Mater Today Commun 2023;35:105571.
[120] Sun Y, Akçay FA, Wu D, Bai Y. Analytical and numerical modeling on strengths of aluminum and magnesium micro-lattice structures fabricated via additive manufacturing. Progress in Additive Manufacturing 2025;10(2):1421–34.
[121] Fan X, et al. Thermoelectric magnetohydrodynamic control of melt pool flow during laser directed energy deposition additive manufacturing. Addit Manuf 2023;71:103587.
[122] Khairallah SA, Anderson AT, Rubenchik A, King WE. Laser powder-bed fusion additive manufacturing: physics of complex melt flow and formation mechanisms of pores, spatter, and denudation zones. Acta Mater 2016;108:36–45.
[123] King WE, et al. Observation of keyhole-mode laser melting in laser powder-bed fusion additive manufacturing. J Mater Process Technol 2014;214(12):2915–25.
[124] Wang W, Yang X, Wang KK, He L. Research on solidification behavior of selective laser melted Mg-Y-Sm-Zn-Zr alloy: from molten pool to cubic sample. Mater Today Commun 2021;28:102517.
[125] Deng Q, et al. Effect of heat treatment on microstructure evolution and mechanical properties of selective laser melted Mg-11Gd-2Zn-0.4 Zr alloy. Materials Science and Engineering: A 2022;829:142139.

[126] Zhu Z, Zhang M, Chen C. Effect of selective laser melting on microstructure and properties of AZ91D alloy. Mater Werkst 2019;50(12):1484–94.
[127] Huang K, Chang T, Jing Y, Fang X, Lu B. Additive manufacturing of magnesium alloys. In: Davim JP, editor. Additive and subtractive manufacturing. first ed. 2020. p. 149–99.
[128] Xu W, et al. Effects of processing parameters on fabrication defects, microstructure and mechanical properties of additive manufactured mg–nd–zn–zr alloy by selective laser melting process. J Magnesium Alloys 2024;12(6):2249–66.
[129] Men Z, et al. Accurate detection and analysis of pore defects in laser powder bed fusion WE43 magnesium alloys. Micromachines 2024;15(7):909.
[130] Suchý J, et al. Corrosion behaviour of WE43 magnesium alloy printed using selective laser melting in simulation body fluid solution. J Manuf Process 2021;69:556–66.
[131] Xie W, Wu C-L, Man H-C, Chan C-W. Effect of zinc content on powder characteristics, porosity, microstructure, and corrosion behavior of SLM-Printed Mg-xZn-0.2 Mn alloys for biomedical applications. Coatings 2023;13(11):1876.
[132] Ezhilmaran V, Suya Prem Anand P, Kannan S, Sivashanmugam N, Jayakrishna K, Kalusuraman G. Review of bioresorbable AZ91, AZ31 and mg–zn–ca implants and their manufacturing methods. Mater Sci Technol 2023;39(8):901–25.
[133] Julmi S, et al. Development of a laser powder bed fusion process tailored for the additive manufacturing of high-quality components made of the commercial magnesium alloy WE43. Materials 2021;14(4):887.
[134] Jaroš J, et al. Influence of laser strategies on performance of lattice structures from magnesium alloy WE43 produced by laser beam powder bed fusion. Adv Eng Mater 2025;27(7):2402625.
[135] Yuan X, Liu M, Wei K, Li F, Li X, Zeng X. Defect, microstructure and mechanical properties of Mg–Gd binary alloy additively manufactured by selective laser melting. Materials Science and Engineering: A 2022;850:143572.
[136] Wang J, et al. Macro-micro numerical simulation and experimental study of Mg-Gd-Y-Zn-Zr alloy fabricated by cold metal transfer wire arc additive manufacturing. J Mater Res Technol 2023;23:403–18.
[137] Cheng S, et al. Effects of arc oscillation on microstructure and mechanical properties of AZ31 magnesium alloy prepared by CMT wire-arc directed energy deposition. Materials Science and Engineering: A 2023;864:144539.
[138] Bär F, et al. Laser additive manufacturing of biodegradable magnesium alloy WE43: a detailed microstructure analysis. Acta Biomater 2019;98:36–49.
[139] Deng Q, et al. Laser powder bed fusion of Mg-6Gd-3Y-0.2 Zr alloy: excellent printability, heterogeneous microstructure and dedicated direct aging heat treatment. J Magnesium Alloys 2024.
[140] Zumdick NA, Jauer L, Kersting LC, Kutz TN, Schleifenbaum JH, Zander D. Additive manufactured WE43 magnesium: a comparative study of the microstructure and mechanical properties with those of powder extruded and as-cast WE43. Mater Char 2019;147:384–97.
[141] Hemachandra M, Thapliyal S, Adepu K. A review on microstructural and tribological performance of additively manufactured parts. J Mater Sci 2022;57(36):17139–61.
[142] DebRoy T, et al. Additive manufacturing of metallic components–process, structure and properties. Prog Mater Sci 2018;92:112–224.
[143] Shi Y, et al. Influence of processing parameters on additively manufactured architected cellular metals: emphasis on biomedical applications. J Funct Biomater 2025;16(2):53.
[144] Fakhar N, Sabbaghian M. A good combination of ductility, strength, and corrosion resistance of fine-grained ZK60 magnesium alloy produced by repeated upsetting process for biodegradable applications. J Alloys Compd 2021;862:158334.
[145] Lovašiová P, et al. Biodegradable WE43 magnesium alloy produced by selective laser melting: mechanical properties, corrosion behavior, and in-vitro cytotoxicity. Metals 2022;12(3):469.
[146] Gonzalez J, Hou RQ, Nidadavolu EP, Willumeit-Römer R, Feyerabend F. Magnesium degradation under physiological conditions–best practice. Bioact Mater 2018;3(2):174–85.
[147] Zhou K, et al. A view of magnesium alloy modification and its application in orthopedic implants. J Mater Res Technol 2025.
[148] Bednarikova V, et al. In vitro corrosion study of selected laser melted WE43 magnesium alloy in Hank's balanced salt solution. Key Eng Mater 2022;923:113–8.
[149] Fard MG, Sharifianjazi F, Kazemi SS, Rostamani H, Bathaei MS. Laser-based additive manufacturing of magnesium alloys for bone tissue engineering applications: from chemistry to clinic. Journal of Manufacturing and Materials Processing 2022;6(6):158.
[150] Motaharinia A, et al. Overview of porous magnesium-based scaffolds: development, properties and biomedical applications. Materials Futures 2025;4(1):012401.
[151] Mei D, Lamaka SV, Lu X, Zheludkevich ML. Selecting medium for corrosion testing of bioabsorbable magnesium and other metals–a critical review. Corros Sci 2020;171:108722.
[152] Estrada RG, Multigner M, Lieblich M, Fajardo S, Rams J. Effect of magnesium addition and high energy processing on the degradation behavior of iron powder in modified hanks' solution for bioabsorbable implant applications. Metals 2022;12(1):78.
[153] Jana A, Das M, Balla VK. In vitro and in vivo degradation assessment and preventive measures of biodegradable Mg alloys for biomedical applications. J Biomed Mater Res 2022;110(2):462–87.
[154] Ning H, Liu X, Li P, Zhang Y, Du Y. Multi-scale precipitates for improved strength and ductility of AZ91D magnesium alloy fabricated using laser penetrating strip directed energy deposition. Materials Science and Engineering: A 2025;934:148352.
[155] Sekar P, Panigrahi S. Understanding the corrosion and bio-corrosion behaviour of magnesium composites–a critical review. J Magnesium Alloys 2024;12(3):890–939.
[156] R. Ilyas, A. Aufa, A. Najihah, M. Noremylia, M. Z. Hassan, and Z. Ismail, "In vivo studies of 3D bioprinting," in Handbook of 3D printing in biomedical applications: CRC Press, pp. 88-98.
[157] Wang L, et al. Degradable magnesium corrosion control for implant applications. Materials 2022;15(18):6197.
[158] Raducanu D, et al. Characterization of a biodegradable Mg-Alloy after SLM processing. 2024.
[159] Dey M, Singh RK. Neurotoxic effects of aluminium exposure as a potential risk factor for Alzheimer's disease. Pharmacol Rep 2022;74(3):439–50.
[160] Liu Q, et al. Cytotoxicity of biodegradable zinc and its alloys: a systematic review. J Funct Biomater 2023;14(4):206.
[161] Wang X, et al. Adverse effects and underlying mechanism of rare earth elements. Environmental Health 2025;24(1):1–23.
[162] Haque S, Tripathy S, Patra CR. Manganese-based advanced nanoparticles for biomedical applications: future opportunity and challenges. Nanoscale 2021;13(39):16405–26.
[163] Szczęsny G, Kopec M, Kowalewski ZL. Toxicity, irritation, and allergy of metal implants: historical perspective and modern solutions. Coatings 2025;15(3):361.
[164] Wang D, Yang Y, Han C. Additive manufacturing of metal implants and surgical plates. In: Additive manufacturing: materials, functionalities and applications. Springer; 2022. p. 151–203.
[165] Wei K, et al. Selective laser melting of Mg-Zn binary alloys: effects of Zn content on densification behavior, microstructure, and mechanical property. Materials Science and Engineering: A 2019;756:226–36.
[166] Pawlak A, Szymczyk PE, Kurzynowski T, Chlebus E. Selective laser melting of magnesium AZ31B alloy powder. Rapid Prototyp J 2020;26(2):249–58.
[167] Liu S, Guo H. Influence of hot isostatic pressing (HIP) on mechanical properties of magnesium alloy produced by selective laser melting (SLM). Mater Lett 2020;265:127463.
[168] Fu P-h, et al. Microstructure and mechanical properties of high strength Mg–15Gd– 1Zn– 0.4 Zr alloy additive-manufactured by selective laser melting process. Trans Nonferrous Metals Soc China 2021;31(7):1969–78.
[169] Chang C, et al. Achieving ultra-high strength and ductility in Mg–9Al–1Zn–0.5 Mn alloy via selective laser melting. Advanced Powder Materials 2023;2(2):100097.
[170] Minárik P, et al. Comparative analysis of microstructure, mechanical, and corrosion properties of biodegradable Mg-3Y alloy prepared by selective laser melting and spark plasma sintering. J Magnesium Alloys 2024;12(4):1496–510.
[171] Verma C, Alameri A, Barsoum I, Alfantazi A. Review on corrosion-related aspects of metallic alloys additive manufactured with laser powder bed-fusion (LPBF) technology. Progress in Additive Manufacturing 2025;10(5):3195–223.
[172] Xie B, et al. Biodegradation, antibacterial performance, and cytocompatibility of a novel ZK30-Cu-Mn biomedical alloy produced by selective laser melting. International Journal of Bioprinting 2020;7(1):300.
[173] Shuai C, et al. Microstructure, biodegradation, antibacterial and mechanical properties of ZK60-Cu alloys prepared by selective laser melting technique. Journal of materials science & technology 2018;34(10):1944–52.
[174] Xu R, et al. Improved biodegradation resistance by grain refinement of novel antibacterial ZK30-Cu alloys produced via selective laser melting. Mater Lett 2019;237:253–7.
[175] Yin Y, et al. In vitro degradation behavior and cytocompatibility of ZK30/bioactive glass composites fabricated by selective laser melting for biomedical applications. J Alloys Compd 2019;785:38–45.
[176] Yao X, et al. Selective laser melting of an Mg/Metallic Glass hybrid for significantly improving chemical and mechanical performances. Appl Surf Sci 2022;580:152229.
[177] Kuah KX, et al. Insights into the influence of oxide inclusions on corrosion performance of additive manufactured magnesium alloys. npj Mater Degrad 2022;6(1):36.
[178] Xie B, et al. Effect of alloying Mn by selective laser melting on the microstructure and biodegradation properties of pure Mg. Metals 2020;10(11):1527.
[179] Yao X, et al. Surface modification of biomedical Mg-Ca and mg-zn-ca alloys using selective laser melting: corrosion behaviour, microhardness and biocompatibility. J Magnesium Alloys 2021;9(6):2155–68.
[180] Liang J, et al. Study on corrosion characteristics and mechanism of laser powder bed fusion of mg–zn–zr alloy. J Mater Res Technol 2024;30:6366–75.
[181] Long T, et al. Novel Mg-based alloys by selective laser melting for biomedical applications: microstructure evolution, microhardness and in vitro degradation behaviour. Virtual Phys Prototyp 2018;13(2):71–81.
[182] Tao J-X, et al. Influence of graphene oxide (GO) on microstructure and biodegradation of ZK30-xGO composites prepared by selective laser melting. J Magnesium Alloys 2020;8(3):952–62.
[183] Hu Q, Chen C, Liu M, Chang C, Yan X, Dai Y. Improved corrosion resistance of magnesium alloy prepared by selective laser melting through T4 heat treatment for biomedical applications. J Mater Res Technol 2023;27:813–25.
[184] Ansari N, Alabtah FG, Albakri MI, Khraisheh M. Post processing of additive manufactured Mg alloys: current status, challenges, and opportunities. J Magnesium Alloys 2024;12(4):1283–310.
[185] Chi J, et al. The impact of pre-and post-treatment processes on corrosion resistance of micro-arc oxidation coatings on mg alloys: a systematic review. Materials 2025;18(3):723.
[186] Wang L, Xia S, Wang Q, Qin X, Jiang B. Simultaneously enhancing the mechanical properties and corrosion resistance in a selective laser melting AZ91 magnesium alloy by hot rolling and subsequent annealing. J Mater Res Technol 2025.

[187] Luo Y, et al. Surface microstructure and corrosion characterization of AZ31 magnesium alloys fabricated by laser surface-modification. J Alloys Compd 2024; 994:174708.
[188] Wang Z-X, Chen G-Q, Chen L-Y, Xu L, Lu S. Degradation behavior of micro-arc oxidized ZK60 magnesium alloy in a simulated body fluid. Metals 2018;8(9):724.
[189] Santos V, Uddin M, Hall C. Mechanical surface treatments for controlling surface integrity and corrosion resistance of Mg alloy implants: a review. J Funct Biomater 2023;14(5):242.
[190] Shuai C, Wang B, Yang Y, Peng S, Gao C. 3D honeycomb nanostructure-encapsulated magnesium alloys with superior corrosion resistance and mechanical properties. Compos B Eng 2019;162:611–20.
[191] Gao C, Zeng Z, Peng S, Tan W, Shuai C. A continuous MgF2 network structure encapsulated Mg alloy prepared by selective laser melting for enhanced biodegradation resistance. Adv Eng Mater 2021;23(10):2100389.
[192] Kopp A, et al. Influence of design and postprocessing parameters on the degradation behavior and mechanical properties of additively manufactured magnesium scaffolds. Acta Biomater 2019;98:23–35.
[193] Yang Y, et al. Selective laser melted rare earth magnesium alloy with high corrosion resistance. International Journal of Bioprinting 2022;8(3):574.
[194] Zeller-Plumhoff B, Tolnai D, Wolff M, Greving I, Hort N, Willumeit-Römer R. Utilizing synchrotron radiation for the characterization of biodegradable magnesium alloys—from alloy development to the application as implant material. Adv Eng Mater 2021;23(11):2100197.
[195] Ran Z, et al. 3D-printed biodegradable magnesium alloy scaffolds with zoledronic acid-loaded ceramic composite coating promote osteoporotic bone defect repair. International Journal of Bioprinting 2023;9(5):769.
[196] Wang Z, Liu B, Yin B, Zheng Y, Tian Y, Wen P. Comprehensive review of additively manufactured biodegradable magnesium implants for repairing bone defects from biomechanical and biodegradable perspectives. Front Chem 2022; 10:1066103.
[197] Bian D, et al. A spatiotemporal "bulk erosion" mode in selective laser melted magnesium alloys and the resulting adverse cell & tissue responses. J Mater Sci Technol 2024;198:243–58.
[198] Wei Z, Attarilar S, Ebrahimi M, Li J. Corrosion and wear behavior of additively manufactured metallic parts in biomedical applications. Metals 2024;14(1):96.
[199] Agbedor S-O, et al. Recent progress in porous Mg-based foam preparation approaches: effect of processing parameters on structure and mechanical property. J Iron Steel Res Int 2022;29(3):371–402.
[200] Li Y, et al. Biodegradation-affected fatigue behavior of additively manufactured porous magnesium. Addit Manuf 2019;28:299–311.
[201] Xie K, et al. Additively manufactured biodegradable porous magnesium implants for elimination of implant-related infections: an in vitro and in vivo study. Bioact Mater 2022;8:140–52.
[202] Wang C, et al. Effect of pore geometry on properties of high-temperature oxidized additively manufactured magnesium scaffolds. J Magnesium Alloys 2023.
[203] Liu J, et al. Biodegradable magnesium alloy WE43 porous scaffolds fabricated by laser powder bed fusion for orthopedic applications: process optimization, in vitro and in vivo investigation. Bioact Mater 2022;16:301–19.
[204] Aufa A, Hassan MZ, Ismail Z, Ren J. Sol–gel surface modification of selective laser melting Ti6Al4V for biomedical applications. Progress in Additive Manufacturing 2025;10(4):2247–64.
[205] Najihah A, Hassan MZ, Ismail Z. Current trend on preparation, characterization and biomedical applications of natural polysaccharide-based nanomaterial reinforcement hydrogels: a review. Int J Biol Macromol 2024;271:132411.
[206] Hu C, Chen C, Zhang M. Effects of Ag content and heat treatment on the microstructure and properties of SLMed AZ61 mg–al–zn alloy. Appl Phys A 2021; 127(3):186.
[207] Thomas KK, Zafar MN, Pitt WG, Husseini GA. Biodegradable magnesium alloys for biomedical implants: properties, challenges, and surface modifications with a focus on orthopedic fixation repair. Applied Sciences 2023;14(1):10.
[208] Mahajan A, Devgan S. Recent advances in surface engineering of additive manufactured materials for enhancing corrosion resistance. Progress in Additive Manufacturing 2025;10(2):1103–18.
[209] Bian D, et al. Degradation behaviors and in-vivo biocompatibility of a rare earth- and aluminum-free magnesium-based stent. Acta Biomater 2021;124:382–97.
[210] Sommer NG, Gieringer S, Schwarze UY, Weinberg A-M, Al-Samman T, Estrin Y. In vivo performance of magnesium alloy LX41 in a rat model. Processes 2022;10 (11):2222.
[211] Ali W, et al. Bioabsorbable WE43 Mg alloy wires modified by continuous plasma-electrolytic oxidation for implant applications. Part I: processing, microstructure and mechanical properties. Biomaterials advances 2023;146:213314.
[212] Dai Y, Li Y. Composition design and Properties of Mg-Zn-Y-Nd-Ca magnesium alloys. J Phys Conf 2021;2021(1):012064. IOP Publishing.
[213] Babenko A, et al. Comprehensive insights into recent innovations: Magnesium-inclusive high-entropy alloys. J Magnesium Alloys 2024.
[214] Ghorbani M, Boley M, Nakashima P, Birbilis N. An active machine learning approach for optimal design of magnesium alloys using Bayesian optimisation. Sci Rep 2024;14(1):8299.
[215] Peng P, et al. Bayesian optimization and explainable machine learning for high-dimensional multi-objective optimization of biodegradable magnesium alloys. J Mater Sci Technol 2025.
[216] Zhang W-n, Wang L-z, Feng Z-x, Chen Y-m. Research progress on selective laser melting (SLM) of magnesium alloys: a review. Optik 2020;207:163842.
[217] Mahmood MA, et al. Printability for additive manufacturing with machine learning: hybrid intelligent gaussian process surrogate-based neural network model for Co-Cr alloy. J Mech Behav Biomed Mater 2022;135:105428.
[218] Chen Y, et al. Machine learning assisted multi-objective optimization for materials processing parameters: a case study in Mg alloy. J Alloys Compd 2020; 844:156159.
[219] Brewick PT. Simulating pitting corrosion in AM 316L microstructures through phase field methods and computational modeling. J Electrochem Soc 2022;169 (1):011503.
[220] Patel T, Huang J, Krukiewicz K. Multifunctional organic monolayer-based coatings for implantable biosensors and bioelectronic devices: review and perspectives. Biosens Bioelectron X 2023;14:100349.
[221] Raeisidehkordi S, et al. Bioactive, antibacterial, and biocompatible multifunctional Mg–GO/ZnO nanocomposite with improved mechanical and corrosion characteristics. Adv Eng Mater 2024;26(21):2400414.
[222] Calin BS, Paun IA. A review on stimuli-actuated 3D micro/nanostructures for tissue engineering and the potential of laser-direct writing via two-photon polymerization for structure fabrication. Int J Mol Sci 2022;23(22):14270.
[223] Zhao Y, et al. Smart self-healing coatings on biomedical magnesium alloys: a review. Smart Materials in Manufacturing 2023;1:100022.
[224] Saberi A, et al. A comprehensive review on surface modifications of biodegradable magnesium-based implant alloy: polymer coatings opportunities and challenges. Coatings 2021;11(7):747.
[225] Gong Q, et al. Single-cell RNA sequencing combined with proteomics of infected macrophages reveals prothymosin-α as a target for treatment of apical periodontitis. J Adv Res 2024;66:349–61.
[226] Li Y, et al. Combined proteomics and single cell RNA-sequencing analysis to identify biomarkers of disease diagnosis and disease exacerbation for systemic lupus erythematosus. Front Immunol 2022;13:969509.
[227] Uddin M, Hall C, Santos V, Visalakshan R, Qian G, Vasilev K. Synergistic effect of deep ball burnishing and HA coating on surface integrity, corrosion and immune response of biodegradable AZ31B Mg alloys. Mater Sci Eng C 2021;118:111459.
[228] Mansoorifar A, Gordon R, Bergan RC, Bertassoni LE. Bone-on-a-chip: microfluidic technologies and microphysiologic models of bone tissue. Adv Funct Mater 2021; 31(6):2006796.
[229] Bandyopadhyay A, Mitra I, Avila JD, Upadhyayula M, Bose S. Porous metal implants: processing, properties, and challenges. Int J Extrem Manuf 2023;5(3): 032014.
[230] Bandyopadhyay A, Ciliveri S, Bose S. Metal additive manufacturing for load-bearing implants. J Indian Inst Sci 2022;102(1):561–84.
[231] Nouri A, Shirvan AR, Li Y, Wen C. Additive manufacturing of metallic and polymeric load-bearing biomaterials using laser powder bed fusion: a review. J Mater Sci Technol 2021;94:196–215.
[232] Lutzweiler G, Ndreu Halili A, Engin Vrana N. The overview of porous, bioactive scaffolds as instructive biomaterials for tissue regeneration and their clinical translation. Pharmaceutics 2020;12(7):602.
[233] Shahzamanian M, Banerjee R, Dahotre NB, Srinivasa AR, Reddy J. Analysis of stress shielding reduction in bone fracture fixation implant using functionally graded materials. Compos Struct 2023;321:117262.
[234] Mehboob A, Barsoum I, Mehboob H, Abu Al-Rub RK, Ouldyerou A. Topology optimization and biomechanical evaluation of bone plates for tibial bone fractures considering bone healing. Virtual Phys Prototyp 2024;19(1):e2391475.
[235] Vega G, Paz R, Gleadall A, Monzón M, Alemán-Domínguez ME. Comparison of cad and voxel-based modelling methodologies for the mechanical simulation of extrusion-based 3d printed scaffolds. Materials 2021;14(19):5670.
[236] Li Y, et al. A review on functionally graded materials and structures via additive manufacturing: from multi-scale design to versatile functional properties. Advanced Materials Technologies 2020;5(6):1900981.

Dr. Mohamad Zaki Hassan is an Associate Professor at the Faculty of Artificial Intelligence, Universiti Teknologi Malaysia (UTM), Kuala Lumpur. He earned his Diploma, Bachelor of Engineering (B.Eng.), and Master of Engineering (M.Eng.) in Mechanical Engineering from UTM in 1997, 1999, and 2003, respectively. In 2012, he completed his Ph.D. in Mechanical Engineering at the University of Liverpool, United Kingdom, where he focused on advanced material processing techniques and mechanical behavior. Dr. Zaki's current research is deeply rooted in the field of additive manufacturing (AM), with a particular emphasis on metallic systems such as Ti–6Al–4V (Ti6), magnesium alloys, and maraging steel, as well as bio-based and sustainable materials for 3D printing applications. His work bridges the gap between engineering materials and real-world applications, addressing both mechanical performance and environmental sustainability. He is especially interested in how these advanced and natural materials can be used to develop next-generation components for biomedical, aerospace, and industrial applications through additive manufacturing technologies like Selective Laser Melting (SLM) and Fused Deposition Modeling (FDM).mzaki.kl@utm.my

Dr. Aufa Adlia Nazari, professionally known as A.N. Aufa, is a Malaysian researcher specializing in additive manufacturing, biomaterials, and orthopaedic implant technologies. She is currently affiliated with the Faculty of Artificial Intelligence, Universiti Teknologi Malaysia (UTM), Kuala Lumpur. She holds a Ph.D. and Master of Philosophy in Mechanical Engineering from UTM, where her award-winning research focused on the design and optimisation of Selective Laser Melted (SLM) Ti–6Al–4V implants for biomedical applications. Her academic foundation includes a Bachelor's degree in Biomedical Electronic Engineering from Universiti Malaysia Perlis, which supports her interdisciplinary expertise across biomedical and material engineering. Dr. Aufa's research explores laser-based manufacturing techniques, surface modification, and metallic biomaterials like titanium and magnesium alloys to enhance implant performance and biocompatibility. She also works on developing bioactive surfaces and corrosion-resistant structures for clinical use. Dr. Aufa continues to advance research in next-generation

biomedical devices by integrating cutting-edge additive manufacturing with practical medical innovation.aufanazari@gmail.com

Dr. hab. inż. Zbigniew Brytan earned his Habilitated Doctorate (D.Sc.) in Materials Engineering from the Silesian University of Technology in 2019. He holds a Ph.D. in Technical Sciences (2006), an M.Sc. in Mechanical Engineering with a specialization in computer-aided engineering of metallic materials (2002), and a B.Sc. in Mechanical Engineering (2000) from the same university. He also completed postgraduate studies in computer networks and microprocessor systems in 2002 and is a certified quality inspector for anticorrosive coatings (TÜV Rheinland Polska, 2017).Dr. Brytan works in additive manufacturing and leads the SynAm Horizon Europe grant project. Since 2010, he has been a member of the Polish Stainless Steel Association and represents them in several Polish Committee for Standardization technical committees since 2017. He is also a member of the Association of Polish Mechanical Engineers and Technicians (SIMP), the Polish Corrosion Society (PSK), and the Society for Computer Materials Science and Surface Engineering.zbigniew.brytan@polsl.pl

Professor X.J. Ren is the Director of the Mechanical Engineering and Materials Research Centre at the Faculty of Engineering, Liverpool John Moores University, UK. His research focuses on materials development and processing, the mechanics of smart materials and structures, computational mechanics, materials simulation, and additive manufacturing. He has held previous academic and consultancy roles at the University of Exeter, Loughborough University, Yanshan University in China, and AMEC Engineering Consultant in the UK. Professor Ren serves on the editorial boards of Materials & Design (Elsevier, SCI) and Surface Technology (EI), and has secured funding from prestigious bodies including EPSRC, the EU, NHS, the Royal Society, and the Royal Academy of Engineering. He currently leads several EU Horizon 2020 Marie Skłodowska-Curie projects aimed at advancing materials joining, freeze casting, porous structures, and additive manufacturing. He has supervised numerous Ph.D. candidates and serves as an examiner for international universities. Additionally, Professor Ren regularly reviews for leading journals such as Materials Research, Materials Letters, Materials Science and Engineering A, and others in the field.X.J.Ren@ljmu.ac.uk